

**QUANTITATIVE IMAGING OF SUBSURFACE STRUCTURES AND
MECHANICAL PROPERTIES AT NANOSCALE USING ATOMIC
FORCE MICROSCOPE**

A Dissertation
Presented to
The Academic Faculty

by

Zehra Parlak

In Partial Fulfillment
of the Requirements for the Degree
Doctor of Philosophy in the
School of Electrical and Computer Engineering

Georgia Institute of Technology

December 2010

Copyright © Zehra Parlak 2010

QUANTITATIVE IMAGING OF SUBSURFACE STRUCTURES AND MECHANICAL PROPERTIES AT NANOSCALE USING ATOMIC FORCE MICROSCOPE

Approved by:

Dr. F. Levent Degertekin, Advisor
School of Electrical and Computer
Engineering
Georgia Institute of Technology

Dr. Jennifer Michaels
School of Electrical and Computer
Engineering
Georgia Institute of Technology

Dr. Hongwei Wu
School of Electrical and Computer
Engineering
Georgia Institute of Technology

Dr. Oliver Brand
School of Electrical and Computer
Engineering
Georgia Institute of Technology

Dr. Elisa Riedo
School of Physics
Georgia Institute of Technology

Date Approved: November 08, 2010

To my parents, Gülten and Şükrü Parlak,
my brother, Zafer Parlak,
and husband, Hüseyin Dinç

ACKNOWLEDGEMENTS

It is a pleasure to thank those who made this thesis possible. I owe my deepest gratitude to my thesis advisor, Dr. Levent Degertekin for his support, insight, and guidance. But more importantly, I want to thank for his patience, motivation, and understanding. In times, he believed in me and my work more than me and made all of this possible. I would also like to thank Drs. Jennifer Michaels, Hongwei Wu, Oliver Brand and Elisa Riedo for serving in my thesis committee and providing helpful comments.

I am grateful to all members of MiST for their kind help and many valuable technical discussions. I especially would like to thank Guclu Onaran who patiently taught me how to use AFM, Dr. Hamdi Torun for many brainstorming sessions, and Rameen Hadizadeh and Dr. Kianoush Naeli for fabricating devices in cleanroom. I also want to thank David Torello for proofreading this thesis. I feel particularly indebted to Guclu Onaran, Hamdi Torun, Baris Bicen, Ayse Ozbil, and Seyma Celik for being there and not hesitating a second when I need help. I never felt alone in Atlanta with their support.

I would like to thank my parents and my brother for supporting my decision of having PhD. I also would like to thank my husband, Huseyin Dinc, for his constant love and understanding. I remember working on one set of experiments, not getting anything working for months, and deciding to quit PhD every Friday. It was his patience and support that made me wanting to try again every Monday. This thesis is dedicated to them; my family.

TABLE OF CONTENTS

ACKNOWLEDGEMENTS.....	IV
LIST OF TABLES.....	VIII
LIST OF FIGURES.....	IX
SUMMARY.....	XIII
CHAPTER	
1 INTRODUCTION	1
1.1 ATOMIC FORCE MICROSCOPE	1
1.2 NANOSCALE ELASTICITY MEASUREMENT	4
1.3 METHODS FOR SUBSURFACE IMAGING AT NANOSCALE.....	8
1.4 INTERACTION FORCES IMAGING IN INTERMITTENT CONTACT MODE AFM	10
1.5 RESEARCH GOALS.....	12
2 MODELING OF THE AFM TIP-SURFACE CONTACT FOR MATERIAL CHARACTERIZATION	15
2.1 AFM TIP CONTACT WITH HALFSpace	16
2.2 AFM TIP CONTACT WITH LAYERED MATERIAL	17
2.3 2-D FINITE ELEMENT ANALYSIS OF AFM TIP CONTACT	21
2.4 3-D SUBSURFACE IMAGING MODEL	23
2.4.1 Implementation of the 3-D Finite Element Model.....	23
2.4.2 Imaging Simulations of Finite Sized Cavities.....	28
2.4.3 Practical Example: Formation of an Electromigration Void.....	30
2.5 CHAPTER SUMMARY	32
3 EXPERIMENTAL VERIFICATION OF THE 3-D FINITE ELEMENT ANALYSIS MODEL	34
3.1 ULTRASONIC METHODS OF AFM	34
3.2 ULTRASONIC AFM EXPERIMENTS FOR THE VERIFICATION OF THE 3-D FEA MODEL.....	40
3.3 APPLICATION OF THE 3-D FEA MODEL AND DISCUSSION	44
3.3.1 Effects of Elastic Properties of Subsurface Structures	45
3.4 CHAPTER SUMMARY.....	47

4 MECHANICAL PROPERTIES IMAGING BY MEASURING TIME-RESOLVED INTERACTION FORCES.....	48
4.1 METHODS OF MATERIAL CHARACTERIZATION BY TAPPING MODE AFM	48
4.1.1 <i>Imaging the Phase</i>	48
4.1.2 <i>Harmonic Imaging</i>	49
4.1.3 <i>Time-resolved Interaction Forces Imaging</i>	51
4.2 FIRAT PROBES	52
4.3 MODELING OF THE FIRAT PROBES	55
4.3.1 <i>Dynamics of FIRAT Probes</i>	55
4.3.2 <i>Simulink Model of the FIRAT Probe</i>	60
4.3.3 <i>Theoretical Modeling of the Interaction Forces</i>	64
4.3.3.1 <i>Surface Forces during the Non-contact Region</i>	64
4.3.3.2 <i>Contact Mechanics Models for AFM Tip-Sample Contact</i>	67
4.3.4 <i>Inverting the Taps for Material Characterization</i>	72
4.4 SENSITIVITY OF THE ELASTICITY MEASUREMENT BY FIRAT PROBE.....	73
4.4.1 <i>Dependence of the Sensitivity on the Probe Dynamics</i>	73
4.4.2 <i>Effects of Experimental Uncertainties on the Elasticity Measurement Sensitivity</i>	74
4.4.3 <i>Effects of the Noise and Probe Stiffness on the Elasticity Measurement Sensitivity</i>	76
4.5 INVERSION OF THE TAPS FOR LAYERED MEDIA CHARACTERIZATION	78
4.5.1 <i>Mechanical Properties Imaging on the Layered media</i>	79
4.6 CHAPTER SUMMARY	81
5 ACTIVE TIP CONTROL OPERATION OF FIRAT PROBES	82
5.1 THE WORKING MECHANISM OF FIRAT PROBES WITH ACTIVE CONTROL	82
5.2 EXPERIMENTAL SET-UP FOR THE ACTIVE TIP CONTROL	85
5.3 RESULTS.....	86
5.4 THE APPLIED FORCES TO THE SURFACE DURING ATC	89
5.5 CHAPTER SUMMARY	92

6 SIMULTANEOUS TIME-RESOLVED INTERACTION FORCE AND ULTRASONIC AFM MEASUREMENT FOR BROAD RANGE OF MATERIALS: ULTRASONIC TRIF MODE	94
6.1 EXPERIMENTAL SET-UP AND THE RESULTS.....	95
6.2 MODELING OF THE FIRAT PROBE FOR ULTRASONIC TRIF MODE	101
6.2.1 <i>Analytical model</i>	101
6.2.2 <i>Modal Analysis by the FEA Model</i>	104
6.2.3 <i>Frequency Response Analysis with the Squeezed Film Effects</i>	108
6.3 FUTURE IMPROVEMENTS FOR ULTRASONIC TRIF MODE	111
6.4 CHAPTER SUMMARY	113
7 CONCLUSION	114
7.1 CONTRIBUTIONS.....	115
7.2 FUTURE WORK	117
REFERENCES	119

LIST OF TABLES

Table 1: Different AFM modes for elasticity measurement.....	14
Table 2: Elastic constants of the materials used in the calculations.....	24

LIST OF FIGURES

Figure 1 (a) Schematic of AFM. (b) A regular AFM cantilever by Veeco Instruments [12].	2
Figure 2 (a) Non-contact mode (b) Contact mode (c) Tapping mode.	3
Figure 3 Force curves on silicon, chromium, and aluminum.	5
Figure 4 Resonance frequency variation of the different contact modes versus stiffness [25].	8
Figure 5 (a) Schematic of deformation in polymer layers (b) Elastic modulus distribution into a polymer-stiff substrate sample [20].	19
Figure 6 (a) Contact stiffness on aluminum and photoresist layers deposited on silicon versus film thickness. (b) Contact stiffness on tungsten layer deposited on silicon substrate [55].	20
Figure 7 Contact stiffness on oxide layer with and without a bonding defect [31].	21
Figure 8(a) Meshed geometry of AFM tip and substrate. The substrate has a spherical cavity. (b) Displacement distribution for AFM tip-sample contact when there is subsurface void.	22
Figure 9 The computational grid on the Y surface [65].	27
Figure 10 The contact stiffness simulations for an embedded spherical cavity [65].	28
Figure 11 (a) Contact stiffness on a silicon substrate with two cylindrical cavities. (b) Schematics of the sample.	29
Figure 12 The normalized contact stiffness of the substrate with two cylindrical cavities with different forces [65].	30
Figure 13 (a) The calculated contact stiffness on a Cu interconnect line with a electromigration defect.(b) The geometry of the simulated electromigration defect.	32
Figure 14 Calculated local vibration amplitudes along a cantilever with rectangular cross section for mode $n=1, 2$, and 3 (from left to right) for different values of k^*/k_c (from top to bottom).	36
Figure 15 The simplified model for cantilever in contact.	37
Figure 16 Schematic of the AFAM setup.	38
Figure 17 Frequency response of an AFM cantilever while it is in contact with photoresist and silicon [59].	40

Figure 18 (a) SEM side view of the substrate used in the experiments. (b) Schematic of the subsurface cavity structure.	42
Figure 19 (a) AFM topography image of the substrate. Scan size is $2\ \mu\text{m} \times 2\ \mu\text{m}$. Arrows A, B, and C in (a) represent the lines where the measurements are performed. (b) Cross section of sample surface on line C, showing maximum 6 nm height difference.....	42
Figure 20 Comparison of experimental and simulation scan data for (a) 315 nm, (b) 350 nm, (c) 465 nm radius of cylindrical cavities [65].	43
Figure 21 The detection limit contours for the cylindrical defects in silicon substrate [65].	47
Figure 22 (A) The reconstructed interaction force and photodiode outputs. Free oscillation is shown in (i), whereas (ii) is the attractive force region. (iv) Repulsive forces become dominant and exceed 200 nN. (B) Taps on different materials [78].	50
Figure 23 SEM image of a harmonic cantilever [86].	50
Figure 24 (a) SEM image of a torsional harmonic cantilever. (b) An illustration of the THC while it is tapping [47].	51
Figure 25 Schematic of the FIRAT probe and the diffraction based optical detection [50].	53
Figure 26 Schematic of the TRIF mode set-up.	54
Figure 27 Experimental TRIF signals on different materials [52].	54
Figure 28 Spring-mass-dashpot model using a squeezed-film damping element [92].	55
Figure 29 The measured and simulated frequency response of a FIRAT probe.....	57
Figure 30 The frequency response of a FIRAT probe with two different gap heights.	58
Figure 31 The experimental set-up of TRIF mode of FIRAT with a sharp tip.....	59
Figure 32 (a) Taps versus time. (b) Taps versus z-piezo movement.....	60
Figure 33 The block diagram of the taps on the probe. Sample properties, probe dynamics, and detection system is included in this model.	61
Figure 34 Experimental $Z(t)$ and $x(t)$ measured on the sample.	62
Figure 35 Taps simulated for a high Q (a) and low Q (b) probe. Taps measured by using a cantilever (c) and FIRAT probe (d).....	63
Figure 36 The schematic of the force curve; two bodies, one is connected to the non-stationary base by a spring. Second body (sample) on the z-piezo.....	65

Figure 37 Interaction force versus tip-sample distance measured by FIRAT probe on pentacene.....	66
Figure 38 Tap simulated by using DMT and BCP mechanics.....	71
Figure 39 FIRAT probe interacting with the sample surface. Material properties can be extracted from the taps [52].	72
Figure 40 (a) Frequency response of the probe for different gaps. 3 μm gap provides 200 kHz cut-off frequency while 2.5 μm gap provides 70 kHz cut-off frequency. (b) Error in the Young's modulus calculation for different cut-off frequencies.	74
Figure 41 The error in measured Young's modulus due to the ambiguity in probe stiffness.	75
Figure 42 The elasticity values that can be measured accurately for different probe stiffnesses.	77
Figure 43 Force noise RMS versus number of averages.	78
Figure 44 (a) The effective elasticity on the surface changes with the indentation. (b) The taps show differences for bulk material and the layered material.	79
Figure 45 The taps simulated for layered material is then analyzed and the calculated values and the real values are plotted.	80
Figure 46 The shape of the FIRAT probe and the indentation on the sample during different phases of intermittent contact mode. Phase III is depicted with and without active tip control. When ATC is employed in phase III, less indentation of the sample occurs.	84
Figure 47 Experimental set-up integrating FIRAT probe with AFM system and ATC circuitry. Peak detection of PD signal is used for controlling Z-piezo. ATC signal is generated from PD signal and is used to retract the FIRAT probe when the contact force exceeds a threshold value.....	86
Figure 48 (a) Individual tap signal without the active tip control. (b) Active tip control signal to the FIRAT probe. (c) Force on the FIRAT probe and real interaction force signal.	87
Figure 49(a) Topography of the polymer sample. Point A and B indicates lower and higher regions of the sample. (b) Force curves on point A and B. (c) Topography of the grating sample. (d) Force curves of different materials on the grating sample.....	88
Figure 50 Topography and the topography difference observed by employing ATC on a (a) PS/PI polymer mixture and (b) patterned chromium on silicon [99].	89
Figure 51 ATC block is added to the Simulink model shown in Fig. 33.	90

Figure 52 The interaction forces after applying ATC.	91
Figure 53 (a) The deflection of the beam when contact force is applied. The area around the tip deflects more than the rest of the beam and the laser beam averages out the displacement. (b) The deflection of the beam when ATC is used. Beam deflects with a smoother profile.	92
Figure 54 The experimental set-up for ultrasonic TRIF mode.	96
Figure 55 Frequency response of free FIRAT probe and probe in contact. Higher resonance modes are amplified with the contact [104].	97
Figure 56 Interaction forces during the tap and the vibration amplitude for 1.25 MHz. By the initial contact amplitude decreases but then increase in the stiffness boosts the amplitude.....	98
Figure 57 Interaction forces during the tap and the vibration amplitude for 1.4 MHz.	98
Figure 58 The vibration amplitude change created by contact stiffness at 1.45 MHz.	99
Figure 59 (a) Topography and (b) adhesion force image of a sample composed of aluminum, silicon, chromium. Elasticity is measured by (c) TRIF. (d) UAFM modes concurrently. (e) Elasticity data by two methods on the same line exhibit higher standard deviation by TRIF due to non-matching probe surface stiffness. Contamination on the silicon surface is clearly observed by UAFM [104].....	100
Figure 60 (a) The simple model of FIRAT probe in-contact. (b) The model is symmetrical and can be cut into half.	102
Figure 61 Normalized resonance frequencies for a thin FIRAT beam in-contact.	103
Figure 62 The FEA calculations for the contact resonances and the analytical solution.	105
Figure 63 Mode shapes of a FIRAT probe when it is free and it is in contact.	107
Figure 64 The simulated frequency response of the free FIRAT probe and probe in contact. Third mode is amplified by the contact.	110
Figure 65 The measured frequency response of the free FIRAT probe and probe in contact.....	110
Figure 66 The proposed set-up for real-time resonance frequency tracking during the tap.	112

SUMMARY

The atomic force microscope (AFM) is a powerful instrument to image topography, mechanical, electrical, and magnetic properties of surfaces at nanoscale. This dissertation focuses on quantitative subsurface and mechanical properties imaging potential of AFM probes. In this work, extensive modeling of AFM probes is presented for thorough understanding of capabilities and limitations of current techniques, these models are verified by various experiments, and different methods are developed by utilizing a force-sensing integrated read-out active tip (FIRAT), which is an active AFM probe with broad bandwidth. These recently introduced methods aim to provide more accurate topography imaging and more sensitive elasticity mapping by AFM on composite materials.

For quantitative subsurface imaging, a 3-D FEA model of AFM tip-sample contact is developed and this model can simulate AFM tip scan on nanoscale-sized buried structures. The 3-D FEA contact model is verified experimentally by employing ultrasonic AFM methods. The simulation results show that one can detect the presence of nanometer-sized subsurface structures by utilizing sensitive elasticity imaging at the nanoscale.

FIRAT, which is active and broadband, is utilized for interaction force imaging during intermittent contact mode and the mechanical characterization capability of this probe is investigated in this dissertation. Analytical and Simulink models are used to study several parameters such as dynamics and material properties. According to the simulation results; probe dynamics, stiffness, stiffness ambiguity, the assumed contact mechanics model, and noise are important parameters that determine the error rates on the measured mechanical properties.

In intermittent contact mode AFM, lowering contact force may result in instability in the imaging and users don't have direct control over the contact forces. To solve this issue, the active nature and high bandwidth of FIRAT probe are utilized and an active tip control (ATC) method is introduced. An experimental set-up for ATC is designed and experimental studies that verify the increased accuracy in topography imaging are performed.

Accuracy of elasticity measurement by AFM highly depends on the probe stiffness and it decreases when the surface stiffness does not match probe stiffness. This constitutes a challenge on the samples with different stiffness regions, such as nanobeads on polymers. A combined ultrasonic AFM and interaction force imaging method is introduced to solve the reduced elasticity measurement sensitivity on stiff materials. An experimental set-up is built to test this idea, the calibration steps for quantitative analysis are determined, and the increased elasticity sensitivity of the combined operation is verified.

CHAPTER 1

INTRODUCTION

Atomic force microscopy is a scanning probe technique that can image topography [1] and characterize the mechanical, electrical, and magnetic properties of the surfaces at nanoscale. The quantitative and non-destructive nature of the atomic force microscope (AFM) makes it a prominent tool that can guide researchers through nanotechnology, microelectronics, and life sciences.

This thesis focuses on mechanical property imaging during the topography mapping at nanoscale by analyzing the AFM tip-sample interaction. The sample of interest for characterization can be a biological specimen like DNA [2, 3] or a cell [4-6], ultra-thin polymers [7], nano-structures like nanowires [8], or zinc oxide belts [9], which are hard to analyze without damaging the sample. Different AFM techniques can be utilized or modified to achieve the sensitive characterization of these samples while extensive modeling and experimental studies are required to understand the limitation and capabilities of these techniques. In this thesis, analysis techniques for subsurface structures and mechanical property imaging are introduced, as well as improved AFM probes and different techniques for AFM imaging.

1.1 Atomic Force Microscope

In 1986, Binnig et al. proposed the AFM [1], which employs a mechanical probe with a sharp tip to scan and detect the surface. The most common AFM probe is a micromachined cantilever beam with a sharp tip – a radius of curvature of 4-20 nm – on the free end. The integration of the AFM probes with accurate x-y-z piezos provides

topography imaging with high resolution [10] while optical microscopes cannot measure structures smaller than a few hundred nanometers due to the diffraction. Although there are other microscopes that can image larger areas than AFM, the high resolution of height mapping makes the AFM useful for many applications. During the two decades following its introduction, the AFM has been for imaging, characterizing, and manipulating [11] surfaces at nanoscale.

A basic schematic of the AFM is depicted in Fig. 1 (a) and an SEM image of a regular AFM cantilever is shown in Fig. 1 (b). The AFM cantilever in Fig. 1 (a) is placed on a holder at an angle and the deflection of the cantilever is detected by the photodiode. The scanner consists of three independently controlled piezoelectric transducers (piezos) that are combined as a tube. The x and y-piezoes provide lateral scanning while the z-piezo extends and retracts to follow the topography. The controller uses the photodiode output and aims to keep the tip-sample distance constant by actuating the z-piezo. The signal used to actuate the z-piezo also provides height information of the sample on the x-y mapping.

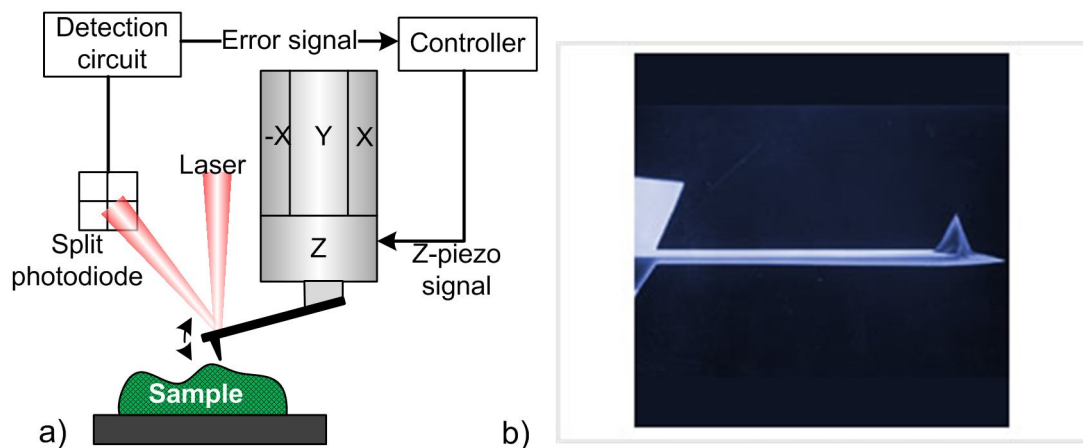


Figure 1 (a) Schematic of AFM. (b) A regular AFM cantilever by Veeco Instruments [12].

Although there are several AFM modes, basic topography imaging can be summarized by three modes that utilize different phases of the tip-sample interaction force. Non-contact, contact, and intermittent contact mode are the most common topography imaging modes of the AFM. As the AFM tip comes close to the surface, it is attracted by the surface due to the capillary and van-der-Waals forces. The non-contact mode AFM utilizes this attractive force regime and measures the topography by detecting the vibration amplitude or the resonance frequency affected by the attractive forces without contacting the surface (Figure 2(a)). When the tip approaches the surface further, tip-sample contact occurs and the interaction force becomes repulsive. The contact mode AFM performs in the repulsive force regime by keeping the contact force between the soft cantilever and the sample constant during the scan (Figure 2 (b)). While these two modes are used in either attractive or repulsive force regimes, intermittent contact mode performs in both force regimes. In this mode, the cantilever tip (during tapping mode) or the sample is vibrated close to the contact where the probe tip is attracted by the surface, contacts the surface lightly and then lifts off (Fig. 2 (c)). Depending on the requirements of the sample, one of these basic modes can be selected.

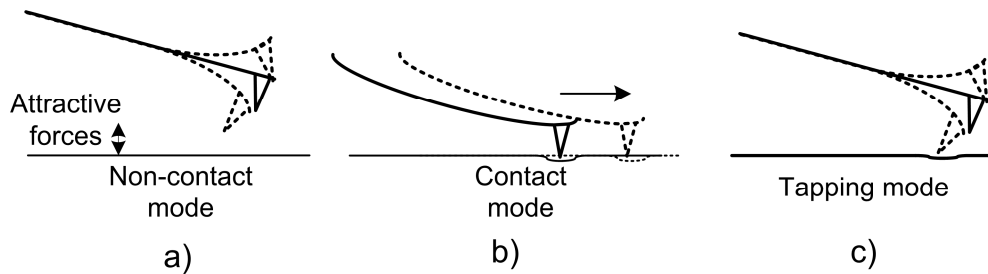


Figure 2 (a) Non-contact mode (b) Contact mode (c) Tapping mode.

1.2 Nanoscale Elasticity Measurement

Nanoscale and non-destructive elasticity measurement is desirable for understanding and improving microfabrication, measurements on biological specimens, and nanotechnology. For example, the elastic modulus of a microfabricated material may define its quality and changes with the fabrication process as seen in the oxidation of the silicon. If a wet oxidation process is applied to the silicon, the elastic modulus of SiO_2 becomes 57 GPa while dry oxidation process results in more reliable SiO_2 with 67 GPa elastic modulus [13]. Mechanical properties imaging studies on cells and DNA will provide insights on the mechanism behind these structures but it is hard to achieve nanoscale elasticity measurements on these specimens in a non-destructive manner. Recent studies by employing AFM show that live metastatic cancer cells have different stiffness than the benign cells [4, 5] and it is thought that the stiffness of the cancer cells affects the way they spread. In addition to these, the ever shrinking sizes achieved in nanofabrication require the mechanics of the materials at nanoscale to be investigated. One example is carbon nanotubes (CNT), in which elasticity depends on the dimensions and affects the reliability of the applications with CNTs [14].

Nanoindentation is one of the methods that can be used to achieve elasticity measurements [15] by moving an indenter to the surface of the material and measuring the force and the displacement [16]. This method is attractive to many users since the user interface calculates the elasticity modulus and the hardness (resistance to plastic deformation) automatically by analyzing the force-displacement curves [16]. Nanoindentation can apply up to a few hundred mNs of force with 75 nN resolution. The displacement can be measured with 0.1 nm resolution [16]. For accurate mechanical

properties measurement, the penetration depth should be at least 20 nm, which may result in plastic deformation. Analyzing the force-displacement curves of the indenter is slow due to the highly controlled load rate [16]. Although dynamic improvements are introduced and scanning capability is added [16, 17], this sensitive tool applies high loads to the samples, can be destructive, and has low force and lateral resolution.

On the other hand, AFM has high lateral and force resolution, can image profiles, and the tip-sample interaction can be quantified for material characterization. Force-distance curve measurement by AFM is a broadly used method to measure elasticity [10, 15, 18]. In this measurement, cantilever deflection is monitored while the z-piezo is modulated and cycles of contact and non-contact regimes appear. In Fig. 3, cantilever deflections versus the z-piezo movements –force-distance curves– on different materials are plotted. In this figure, the region A represents the non-contact area since there is no deflection on the cantilever even when the z-piezo moves. The region B is the contact region, where the z-piezo moves the cantilever tip into the sample and the cantilever deflects.

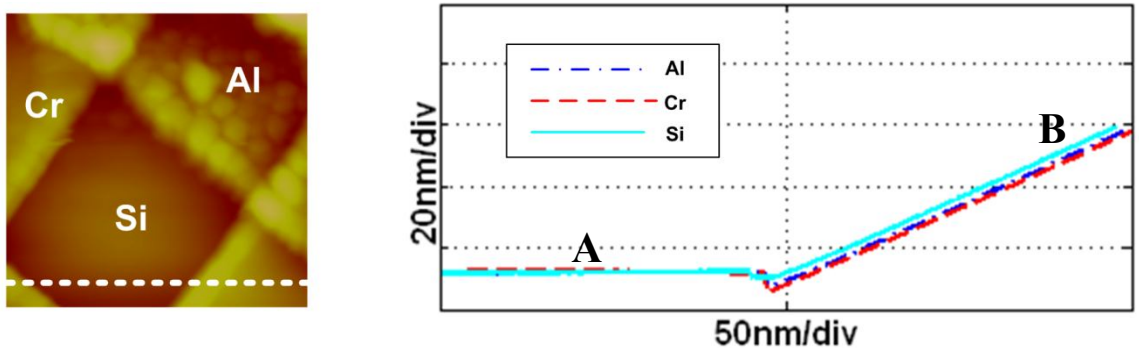


Figure 3 Force curves on silicon, chromium, and aluminum.

Accurate z-piezo movement and cantilever deflection measurements provide sensitive force-displacement data that can be used to determine the mechanical properties of the sample. Basically, a lower slope in the force-distance curve means a softer sample since the tip indents the sample and this indentation decreases the measured cantilever deflection. This measurement technique is easy to implement and is used for many applications, such as characterizing micro and nano-fabricated structures, measuring bonding forces of biomolecules [19] and the elasticity of the cells, and analyzing multiple layered polymers [20]. Force modulation microscopy (FMM) [21] and pulsed-force mode [22] are similar to force curve measurement in principal with an additional scan capability. The cantilever tip is kept in contact in FMM [21] whereas the tip leaves the contact in pulsed-force mode [22], while the z-piezo is modulated.

One of the requirements for sensitive measurements with this technique is comparable tip-sample contact and cantilever stiffness. Spring constant of contact stiffness, k^* , is a function of the AFM tip radius, R , the applied contact force, F_0 , and the reduced equivalent Young's modulus of the substrate and the tip, E^* ;

$$k^* = \sqrt[3]{6F_0RE^{*2}} \quad (\text{Eq. 1.1})$$

One can model the mechanism of the AFM force-displacement curves by two serial springs; the cantilever and the contact. Since the user measures the deflection of the cantilever in the force-displacement curves, this deflection should differ in a detectable amount on different materials for sensitive material characterization. However, for high E^* materials, k^* increases rapidly with the contact and becomes much higher than the cantilever stiffness.

The force-distance curves shown in Fig. 3 were obtained using a 20 N/m cantilever on three different materials; aluminum ($E=70$ GPa), chromium ($E=279$ GPa), and silicon ($E=150$ GPa). When the cantilever deflects 5 nm for this case, the tip-sample contact is deformed by 4.9 Å, 3.1 Å, and 3.9 Å for aluminum, chromium, and silicon. Since the differences in the indentations are low, the sensitivity depends on the noise levels. As plotted in Fig. 3, the slope of the force-distance curves are nearly same for these different materials, which means that the sensitivity of the measurement may not be capable of elasticity imaging of these three distinctly different materials.

To increase the sensitivity of the k^* measurement on stiff materials, one can increase the cantilever stiffness, k_c , but this approach decreases the force resolution. A more useful approach is to vibrate the cantilever in its higher resonances while it is in contact and to detect these resonance frequencies [23, 24]. The cantilever has a higher effective spring constant when it is operated in high contact resonances and, as a result, the sensitivity is increased for stiff materials. In the following figure, the normalized resonance frequency versus normalized contact stiffness is plotted for different flexural modes of a cantilever. According to these calculations, the resonance frequency of the first contact mode shifts for k^*/k_c values less than 20. However, the resonance frequency of the second mode becomes sensitive when the first resonance mode is not responding to higher k^* . Higher contact resonance modes provide stiffer probes and become more sensitive as the k^* increases. One can select the suitable contact resonance mode for the range of the contact stiffnesses to be measured.

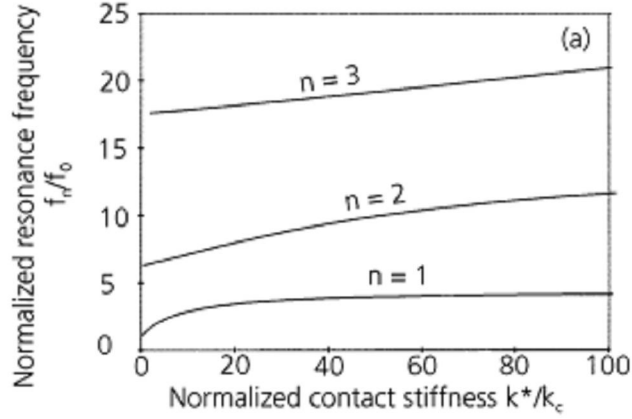


Figure 4 Resonance frequency variation of the different contact modes versus stiffness [25].

Vibrating the cantilever probes at high contact resonance modes for sensitive mechanical properties imaging is called ultrasonic methods of AFM. Ultrasonic methods of AFM are valuable techniques for material characterization [26, 27] and subsurface imaging [28]. In ultrasonic methods of AFM, contact mode AFM is used and the cantilever [26] –or the sample [29]– is vibrated at ultrasonic frequencies, while tip and sample are in contact with a DC force. By calibrating the cantilever and employing analytical expressions, one can calculate the contact stiffness on a surface from the contact resonance frequencies. The accurately measured k^* makes it possible to obtain E^* by applying Eq. 1.1 with known F_0 and R .

1.3 Methods for Subsurface Imaging at Nanoscale

Noninvasive imaging of the subsurface at nanoscale is a critical task for many applications. With such a capability, one can analyze the embedded structures in micro and nano-fabricated materials [30] and detect the defects that occur during and after the fabrication such as bonding defects between layers [31] or electromigration defects [32].

In addition to this, non-invasive subsurface imaging on biological systems can provide significant insights on sub-cellular phenomena [33, 34].

Subsurface imaging at nanoscale may have a significant contribution to the microelectronics and fabrication since it can increase the reliability and repeatability of the fabrication processes. However, common subsurface imaging techniques suffer lateral resolution limitations due to diffraction and cannot provide subsurface images at nanoscale. Many tools have been developed to achieve subsurface images with nanometer resolution and each of these tools has advantages and disadvantages.

While the materials in semiconductor technology are mostly opaque to the light, these materials are transparent to acoustic waves [35]. As a result, scanning acoustic microscopy (SAM) is an option for imaging interior of the samples; layers and defects in the semiconductor circuits have been imaged by this technique [35]. In SAM, a sapphire lens is used to focus acoustic waves via a coupling fluid into the solid sample [36]. The negligible attenuation of the acoustic waves in semiconductors makes it possible to image structures embedded under hundreds of micrometers of material [35]. However, the lateral resolution is limited by diffraction.

Another method for subsurface imaging is scanning near-field optical microscopy (SNOM) [37, 38]. Optical microscopes suffer from the diffraction limit while imaging and their resolution is around a few hundred nanometers. However, SNOM is not diffraction limited since the light goes through a small aperture of 10-20 nm radius and becomes evanescent [39]. Subsurface imaging at nanoscale is possible with SNOM when the sample is transparent and thin, such as polymers used in microfabrication. Due to the transparency requirement, SNOM cannot be used on microelectronic circuits.

Scanning transmission x-ray microscopy (STXM) is one of the tools that can image the subsurface of different materials and does not require extensive sample preparation. It has been shown that it can measure electromigration defects in microelectronic devices. The wavelength of x-ray is between 0.01 nm and 10 nm, but the lateral resolution is limited by the focused beam size that is around 200 nm [32, 40]. By using x-ray tomography, it is possible to image the organelle structure inside a cell [41].

It is shown that AFM can become a sensitive tool for elasticity measurements by employing ultrasonic methods. If subsurface structures are present in the volume indented by the AFM tip-sample contact, the elasticity measured on the surface is also affected [42, 43]. As a result, subsurface structures close to the surface can be detected by measuring the surface elasticity. However, to analyze the subsurface imaging capability of AFM, valid models of AFM tip-sample contact are required.

1.4 Interaction Forces Imaging in Intermittent Contact Mode AFM

Although ultrasonic methods of AFM can provide sensitive mechanical property mapping, they have some drawbacks, such as scan speed, tip-wear related errors, complex modeling, calibration steps needed for extracting information, and the sample deformation. In addition to these drawbacks, contact mode may not be used in imaging some soft samples, which can be damaged by the lateral forces. If the aim is to perform material characterization on soft samples while performing an image scan, a different mode of AFM, intermittent contact mode, should be used.

Tapping mode (TM) AFM or intermittent contact mode (tapping mode is a commonly used type of intermittent contact mode) is the preferred mode of operation in imaging soft samples. In TM AFM, the cantilever is vibrated by a piezoelectric transducer attached to

the cantilever substrate, and the vibration amplitude is monitored. This mode has less friction on the sample since it taps the surface intermittently. Utilizing TM AFM for mechanical property mapping makes it possible to characterize soft samples. Imaging the phase [44] and measuring the harmonics [45, 46] during TM AFM are some of the methods that have been used by exploiting the dynamics of the commercial AFM cantilevers. Due to the dynamical limitations of the commercial cantilevers, it is necessary to introduce different AFM probes for material characterization by TM AFM. The approaches for designing a new probe include modified cantilevers, such as harmonic cantilevers [45], torsional harmonic cantilevers [47] and cantilevers with integrated sensors [48, 49], and a force sensing integrated read-out and an active tip (FIRAT) [50]. Some of the mentioned probes can measure the time-resolved displacement caused by the tip-sample interaction forces during TM AFM, and this information can be used to extract the surface energy and Young's modulus of the sample.

FIRAT is a recently developed AFM probe that is based on a micromachined membrane pressure sensor with electrostatic actuation and interferometric detection [50, 51]. A sharp tip is added to this pressure sensor to make it capable of interaction force sensing. Its broad bandwidth provides time-resolved interaction force sensing without mathematical reconstruction. It has been showed that analyzing interaction forces obtained by FIRAT probe can be used to determined elasticity, adhesion, and hysteresis on the samples [52].

One of the problems encountered in intermittent contact mode AFM is the instability caused by attractive forces during the taps. To overcome this instability, one has to apply

higher oscillation amplitude, which may cause tip wear or sample deformation due to higher repulsive forces, or use stiffer AFM probes [53] that reduce the force sensitivity. For AFM cantilevers, which are passive sensors, there is always a trade-off for selecting the cantilever stiffness. However, if an active sensor such as a FIRAT probe is used, the operation of the probe can be controlled during each tap to avoid higher repulsive forces while being stiff against the attractive forces that cause instability.

Another problem for material characterization during intermittent contact mode AFM is the reduced sensitivity on the stiff materials. Although interaction force imaging during TM AFM can provide sensitive elasticity measurements on compliant samples, it has reduced sensitivity on stiff materials because of high contact stiffness. This reduces the range of the materials that can be characterized by this mode. On nanocomposites or biological specimens with different stiffness regions, mechanical properties mapping during topography imaging is particularly challenging. A solution to this problem can be dynamical stiffening of the probes in ultrasonic frequencies while obtaining interaction forces.

1.5 Research Goals

In the course of this research, the aim is to analyze the capabilities and limitations of the AFM for quantitative material characterization and to improve mechanical properties imaging by the AFM. This requires understanding the shortcomings of current techniques, constructing finite element and Simulink models for analyzing the current methods, performing experimental verifications, and introducing solutions to existing problems.

Ultrasonic methods of AFM have been used to obtain mechanical properties of samples and it has been shown that the presence of subsurface structures can be detected by using these methods. A 3-D finite element analysis model of AFM tip-sample contact is constructed and this model can determine whether a subsurface structure is detectable or not by means of elasticity measurement. The 3-D FEA model is then verified by using an ultrasonic AFM technique and a special sample with known substructures.

FIRAT is a recently developed AFM probe that can image the tip-sample interaction forces during intermittent contact mode of AFM. These interaction forces can be used to analyze mechanical properties of the samples. A Simulink model is developed to study the effects of probe dynamics and material properties on the taps. The Simulink model and associated experimental studies are used to analyze the error sources on the mechanical properties data obtained by FIRAT probe. The results of this study can guide researchers for AFM probe designs.

Indentation on compliant materials and nanocomposites during TM AFM cannot be controlled if a passive AFM probe is used. The active nature of the FIRAT probe is used in this study to improve intermittent contact imaging on soft samples and provide more realistic topography data. While intermittent contact mode imaging is improved with this application by actively controlling the FIRAT probe, the interaction forces are recorded for mechanical property imaging. As a result, non-abrasive nanomechanical imaging is provided in soft samples.

The sensitivity of the elasticity measurement by intermittent contact mode (force-displacement curves, pulsed-force mode, TRIF, torsional cantilevers) highly depends on the cantilever stiffness (Table 1). This constitutes a problem for characterizing composite

samples with different stiffness regions by the same probe. To solve this issue, we introduced interaction force imaging with dynamic stiffening at ultrasonic frequencies so that one can measure the elasticity of a broad range of samples with high sensitivity.

Table 1. Different AFM methods for elasticity measurement.

	Cantilever Stiffness (N/m)	Sensitive elasticity measurement range	Adhesion measurement Capability	Mode of operation
Force-displacement curve	0.5	<20 MPa ^{**} 5-500 MPa ^{**} 0.2-2 GPa 1-20 GPa	Yes	Intermittent contact (max 30 Hz)
Pulsed-force mode	4 40 200		Yes	Intermittent contact (max 5 kHz)
TRIF by FIRAT	10-40 [*]		Yes	Intermittent contact (max 5 kHz)
Torsional cantilevers	1-5		Yes	Intermittent contact (TM) (max 50 kHz)
Ultrasonic AFM	1-5	>2 GPa	No	Contact

^{*}The spring constant can be decreased by using electrostatic spring softening.

^{**}The measurements should be performed in fluid (water, buffer solution) for pulsed-force mode.

CHAPTER 2

MODELING OF THE AFM TIP-SURFACE CONTACT FOR MATERIAL CHARACTERIZATION

Material characterization in micro and nanoscale is desired for better understanding of substrates, improving microfabrication processes, and advancing nanotechnology. While friction, adhesion, and wear are critical properties to characterize surfaces [16], elasticity and hardness of bulk materials are important parameters for fabricating reliable MEMS/NEMS devices [36]. In addition to measuring the mechanical properties of the samples, it is desired to image the structures situated below the surface. Layer thicknesses, adhesion between boundaries, and embedded impurities can be evaluated by nanoscale subsurface imaging. The high resolution probing capability of AFM makes it a good candidate for nanoscale subsurface imaging, since it can detect the presence of subsurface structures by means of the changes in the surface elasticity.

As the AFM tip contacts the surface, both the tip and the surface deforms and this deformation is a function of the elasticity of the materials, the applied force and the tip radius. The deformation due to the force can be modeled as a spring and the spring constant is the contact stiffness. The measured contact stiffness on a surface will differ from the measurements on the bulk material if there are subsurface layers, structures, grain boundaries and defects. In this chapter, it is assumed that AFM can measure contact stiffness with high sensitivity and the focus is on modeling contact mechanics and the effects of subsurface structures on contact stiffness. Techniques to utilize AFM for nanomechanical properties are discussed in third, fourth and sixth chapters.

2.1 AFM Tip Contact with Halfspace

The theoretical model for the contact of two elastic axisymmetric bodies was introduced by Hertz in 1882 [54]. This model has been a very valuable tool for analyzing the effects of the applied force and the radius on the contact deformation. It can also be used to calculate the reduced Young's modulus from the contact stiffness measured by the AFM on the different half-space materials. The assumptions for this model can be summarized as the following [15, 54]:

- Continuous and non-conforming surfaces;
- Small strains;
- Elastic and homogeneous bodies;
- Frictionless surfaces.

For an elastic sphere with the radius R , like the AFM tip, in contact with a flat and elastic surface, the contact region will be circular. Although both the surface and the tip will have roughness and contact will occur on these asperities, these asperities are assumed to be much smaller than the contact radius in Hertzian contact theory. According to this theory, the contact radius is:

$$a = \sqrt[3]{\frac{3FR}{4E^*}} \quad (2.1)$$

where F is the applied load, R is the tip's radius of curvature, and E^* is the equivalent Young's modulus. The equivalent Young's modulus, E^* , is derived from the Young's modulus, E_1 , E_2 , and Poisson ratio, ν_1 , ν_2 , of two bodies by using following equation:

$$\frac{1}{E^*} = \frac{1 - \nu_1^2}{E_1} + \frac{1 - \nu_2^2}{E_2} \quad (2.2).$$

The mutual approach of two bodies –the maximum deformation–, δ , and the contact stiffness, k^* , are shown as:

$$\delta = \frac{a^2}{R} = \sqrt[3]{\frac{9F^2}{16RE^{*2}}} \quad (2.3)$$

and

$$k^* = \frac{3F}{2\delta} \quad (2.4).$$

Hertzian contact theory is widely used in micro/nano tribology to calculate the elastic modulus from the AFM or nanoindentation measurements. In addition to this, Hertzian theory is used in verifying simulation or analytic based methods on contact mechanics. Sneddon extended the contact theory developed by Hertz to any axisymmetric tip geometry pushed into an elastic half-space. As a result, tip can be defined by a parabolic function instead of a perfect sphere and the generalized formula for the elastic contact of half-space materials is:

$$F = a\delta^b, \quad (2.5)$$

where a and b are specific parameters.

These models are valid for low loads that do not cause plasticity. In addition to this, the adhesive forces are either assumed very low or as an offset. Specific models should be applied for high loads that cause plastic deformation.

2.2 AFM Tip Contact with Layered Material

Hertzian contact theory provides a routine calculation for analyzing AFM tip-substrate contact when the sample is half-space. However, the samples of interest are not only bulk materials; samples with thin layers are also used in many applications and have to be investigated. The layered media can be thin films in microelectronics, compliant

coatings, polymer brushes or biological tissues [20, 55]. To study the data obtained by probing these samples, one should have a model that explains the contact on layered media. One critical point for these models is that the effective Young's modulus –the modulus measured on the surface– is a function of the tip radius and the applied force, while it is a constant for the bulk material case. As a result, the models on the layered media provide the effective Young's modulus for a given applied force and this value is substituted in Eq. 2.2 of the Hertzian theory.

When the layers are compliant, such as polymer coatings, the models should explain the deformation of the multiple layers and the stiff substrate. Several models have been improved for single [7] and multiple [20, 56] polymer layers with different conformation parameters and these models have been validated by using AFM force-distance curve experiments. A simple expression for the composite elastic modulus of a single layered sample is shown as:

$$\frac{1}{E'} = \frac{1}{E_f} (1 - e^{-\alpha h/t}) + \frac{1}{E_s} (e^{-\alpha h/t}), \quad (2.6)$$

where E_f and E_s are the elastic moduli of the film and the substrate, t is the total film thickness, h is the indentation, and α is the conformation parameter [20]. According to this expression, if the indentation is too small, one can only measure E_f . As the indentation gets higher, the substrate will affect the measured elastic modulus. To analyze a force-distance curve for film thickness measurement by using this model, one should know the elastic moduli of the materials and then calculate the unknown parameters. The conformation parameter, α , usually represents the transition region between two materials.

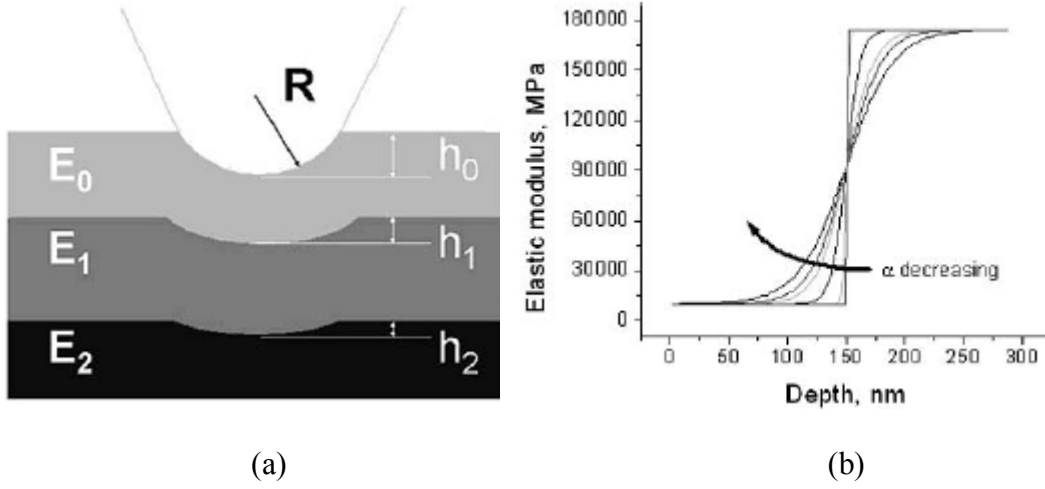


Figure 5 (a) Schematic of deformation in polymer layers (b) Elastic modulus distribution into a polymer-stiff substrate sample [20].

These expressions for layered materials are helpful for high indentation, compliant layers, and transition regions. However, these models cannot be used for stiff layers and small indentation, since it depends on the deformation of the layers. For these cases, one can model the contact by using the radiation impedance method. The radiation impedance of the mechanical radiators on the layered materials has been studied by several researchers [57, 58]. The work on mechanical radiators can be used to explain the AFM tip-sample contact when the contact area is actuated at an ultrasonic frequency for contact stiffness measurements. Since the contact radius, a , is much smaller than the wavelength, λ_s , at that ultrasonic frequency; the generated waves into the solid are inhomogeneous waves and the quasistatic approximation is valid [55]. One can calculate the surface stiffness, k_s , from the effective radiation impedance seen by the tip on the contact area.

$$k_s = \frac{\text{normal force on the contact}}{\text{displacement}} = j\omega Z_s \quad (2.7)$$

where Z_s is the mechanical impedance and ω is the angular frequency. Given that the waves radiated from the contact are inhomogeneous, the radiation impedance is imaginary and the contact is a lossless spring.

The radiation impedance method can be used to calculate the surface stiffness, while Hertzian contact theory is needed for contact stiffness calculation. Yaralioglu et al. improved an iterative algorithm, called contact stiffness algorithm (CSA), by combining these two methods [55]. CSA guesses a contact radius, calculates the surface stiffness for this radius, and compares the radius related to this surface stiffness with the initial guess. It is possible to verify this algorithm for half-space substrate and to extend CSA to layered media. The calculations for layered media can only be validated by finite element modeling [55] and the experiments [59]. CSA has been used to calculate the contact stiffness on the thin films and comparing these contact stiffness values with experimental data will provide the film thicknesses.

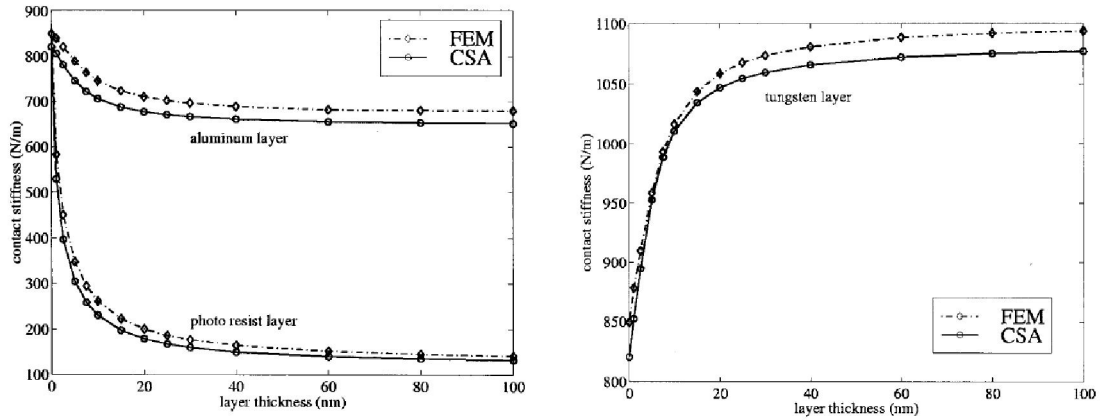


Figure 6 (a) Contact stiffness on aluminum and photoresist layers deposited on silicon versus film thickness. (b) Contact stiffness on tungsten layer deposited on silicon substrate [55].

CSA is used to characterize AFM tip-sample contact for layered samples. In addition to this, it is possible to incorporate interface boundary problems into CSA, such as voids or slippery bonds between layers [31]. Bonding problems are costly issues for

semiconductor technology that decrease the yield immensely. By using CSA, one can evaluate the boundary conditions of an interface by comparing the CSA results with experimental data. The contact stiffness testing with CSA is non-destructive and valid on defects much larger than the contact area.

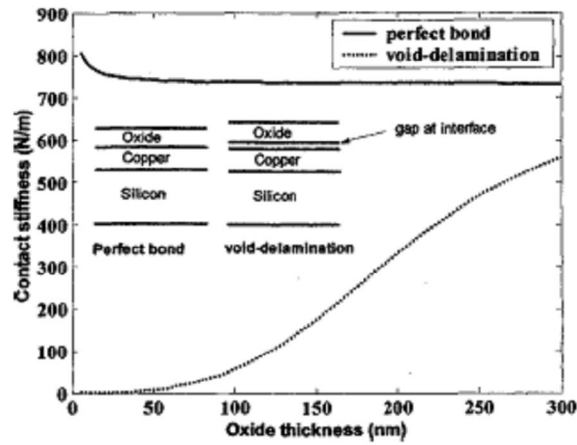


Figure 7 Contact stiffness on oxide layer with and without a bonding defect [31].

2.3 2-D Finite Element Analysis of AFM Tip Contact

In addition to Hertzian contact theory and CSA, numerical methods like finite element analysis (FEA) can evaluate the contact stiffness for the multilayered media and the half-space material [55, 60]. Contact analysis of FEA can be used to calculate contact stiffness as the contact stiffness measurement by ultrasonic AFM is quasistatic.

The previously mentioned methods are for handling the contact mechanics of the half-space materials, the layered materials and the samples with boundary defects. In all of these cases, the sample or the subsurface structure is much larger than the AFM tip-sample contact. However, it is not possible to use these methods for analyzing the effects of finite-size subsurface structures on the contact stiffness. One can build a 2-D FEA model to investigate the AFM tip-sample contact when the sample has a finite size embedded structure.

A 2-D FEA model of the AFM tip-sample contact is easy to construct and the computation time is not excessive. To build an appropriate 2-D FEA model, axisymmetry should be exploited. The spherical tip geometry is suitable for axisymmetry already, so the substrate also has to be modeled with axisymmetry. The 2-D FEA calculations are performed in ANSYS 11.0.25. The tip and the sample are meshed with axisymmetric 2-D element PLANE42. Since the y-axis is the axis of the axisymmetry, a lateral displacement boundary is assigned to this axis. The lines of possible contact are assigned contact elements; TARGE169 and CONTA172. Axisymmetric 2-D FEA models impose limitations on the structures and cannot be used to simulate an imaging scan. 2-D FEA models have been used to verify algorithms like CSA and to determine the feasibility of subsurface imaging on finite size structures by AFM. The geometries and the meshed regions are shown in Fig. 8. The small part on the top part of the model is the AFM tip, while the larger section is the substrate. One can model axisymmetric subsurface structures like spherical voids (Fig. 8) by using a 2-D FEA model.

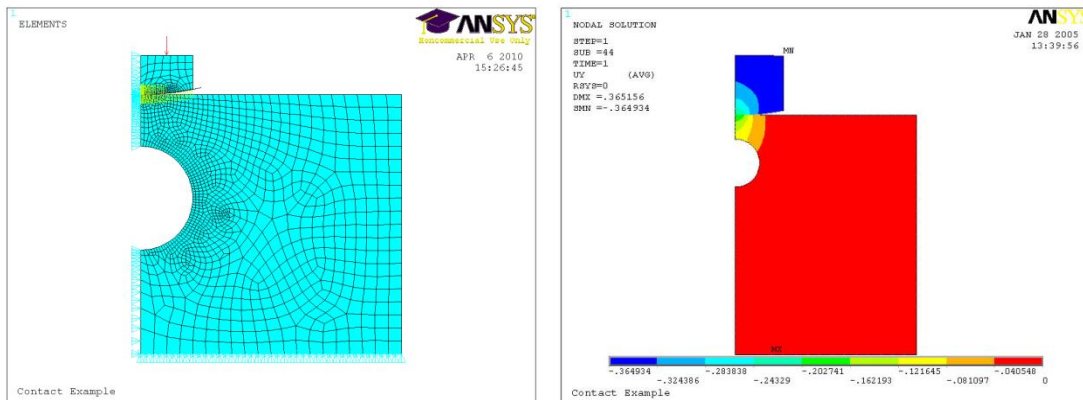


Figure 8(a) Meshed geometry of AFM tip and substrate. The substrate has a spherical cavity. (b) Displacement distribution for AFM tip-sample contact when there is subsurface void.

2.4 3-D Subsurface Imaging Model

AFM is capable of measuring the contact stiffness on different materials with high sensitivity and imaging the effects of the subsurface on the mechanical properties. The quantitative and sensitive contact stiffness results are encouraging for determining the size and the shape of the subsurface structures. However, adequate analytical or numerical models are required for interpreting experimental contact stiffness measurements. In most of the studies, FEA models have used axisymmetry while evaluating the contact stiffness of the AFM tip-substrate contact [55, 61, 62].

There has not been a validated model for the effects of finite size nanoscale subsurface structures on the contact stiffness. A 3-D FEA model of the AFM tip-sample contact can quantitatively characterize the effects of various subsurface structures with arbitrary shape and lateral position relative to the AFM tip. The experimental contact stiffness results can be analyzed for subsurface imaging by using this 3-D FEA model. To provide all these capabilities, a 3-D finite element subsurface imaging model is constructed in this research.

2.4.1 Implementation of the 3-D Finite Element Model

To perform contact stiffness analysis for an AFM tip scanning over a substrate with a finite size subsurface structure, it is necessary to create a fully 3-D FEA model which does not rely on axisymmetry. In analytical or FEA models of the AFM tip-substrate contact, the AFM tip is mostly spherical with a 10-250 nm radius. For a spherical tip and half-space sample, researchers use Hertzian contact theory [54], which explains the contact of spherical surfaces [63, 64]. Effective Young's modulus, E^* , radius

of curvature, R , and applied force, F_0 , are the parameters for contact stiffness and contact radius according to this theory [54]. E^* is calculated by using reduced Young's moduli of the tip, M_T , and the sample, M_S .

$$\frac{1}{E^*} = \frac{1}{M_T} + \frac{1}{M_S}, \text{ where} \quad (2.8)$$

$$M_T = \frac{E_T}{1 - \rho_T^2} \text{ and } M_S = \frac{E_S}{1 - \rho_S^2}. \quad (2.9) \text{ and } (2.10)$$

E_S , E_T , ρ_S , and ρ_T are Young's moduli and Poisson ratios of the tip and the substrate. R is the radius of the AFM tip, since substrate is smooth and has infinite radius of curvature.

Table 2: Elastic constants of the materials used in the calculations.

Material	Mechanical Properties	
	Young's Modulus	Poisson Ratio
Silicon	127 GPa	0.278
Silicondioxide	75 GPa	0.17
Copper	110 GPa	0.33
Tungsten	411 GPa	0.28

Although 3-D FEA models are capable of simulating AFM tip-sample contact for any geometry, it consumes too much computational resources. Both the tip and the sample should be much larger than the contact radius and the contact area should be finely meshed. As a result, the number of the elements is high. On the other hand, the aim of this simulation is to calculate the effective Young's modulus of the sample and using a smaller tip will decrease the computation time immensely.

In the presented 3-D FEA model of the AFM tip-substrate contact, M_S is of interest since M_T can be calculated by using the mechanical properties of the silicon tip in Table 2. Moreover, simulating the AFM tip with its real elastic parameters leads to the excessive computation time. This problem can be avoided when an infinitely rigid tip material is assumed in the simulations instead of the actual M_T , because in this case the elastic parameters of the tip do not affect the results anymore [43, 61]. The effect of the deformation in the AFM tip can be included later analytically to calculate the actual contact stiffness, k^* values as discussed below. In other words, in this model the AFM tip is simulated as a rigid indenter. This configuration gives the opportunity of using a smaller tip structure since the tip does not need to be a half-space any more.

For an infinitely stiff tip ($M_T \rightarrow \infty$), E^* is simply given by M_S according to Eq. 2.8. Consequently, Eq. 2.11 below provides surface stiffness, k_s , assuming Hertzian contact:

$$k_s = \frac{3F_0}{2h}. \quad (2.11)$$

where h is the deformation of the surface and F_0 is the contact force [55]. Note that, this equation is different from Eq. 2.4 since that equation is computed for the contact stiffness.

In order to obtain k^* , three more steps are required. First, M_S is calculated using the following equation;

$$M_s = \sqrt{\frac{k_s^3}{6F_0 R}} \quad (2.12)$$

By substituting M_S of Eq. 2.12 into Eq. 2.8 and using actual M_T , E^* is obtained. Contact stiffness of Hertzian contact can be evaluated using the relation:

$$k^* = \sqrt[3]{6F_0RE^{*2}} \quad (2.13)$$

3-D FEA calculations are implemented by ANSYS 11.0.25. The 3-D structural solid element (SOLID92) is used to mesh the tip and the substrate. In addition, the possible contact area is meshed with 3-D contact elements (TARGE170, CONTA174). The scan direction is on the x-axis and the substrate is symmetric over the y-axis, since the aim is scanning a substrate with a finite size subsurface structure as shown in Fig. 9. Although symmetry on the y-axis is not necessary, one more surface in the middle of the geometry provides better meshing. Note that, it is always possible for this model to use a non-symmetry condition with more complicated subsurface structures. Spheres, cylinders or rectangular prisms can be subsurface structures in this y-symmetric model. Also, more than one structure can be present. The bottom of the tip is spherical and always touches the center of the substrate which is a cylindrical volume with at least 2 μm radius. Convergence studies show that any smaller sized substrate does not agree with Hertzian contact validation for half-space case because of the close boundaries. To simulate a scan over the surface, the subsurface structures are relocated to different positions and the contact stiffness is calculated for those positions.

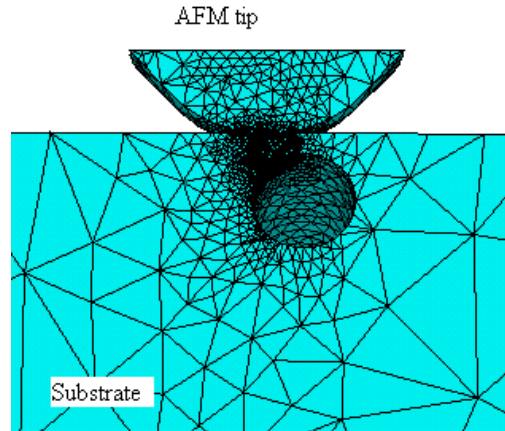


Figure 9 The computational grid on the Y surface [65].

One of the drawbacks of the 3-D FEA contact model is the computation time, which is mainly determined by the nonlinear contact analysis and the number of nodes. The number of nodes should be high for more accurate results, but a high node number leads to excessive computation time. The SMRTSIZE command of ANSYS can be used with medium size to control the distribution of the elements on whole volume. This command provides coarse meshing. However, fine meshing around the contact, especially around the contact elements, is necessary. Thus, it is suggested to refine the meshing around the contact by using NREFINE command. Accordingly, the 3-D model of AFM tip-substrate contact with an acceptable number of nodes can be obtained. Each simulation run takes approximately 15 minutes on average on an Intel P 4 3.0 GHz.

Convergence analysis of the 3-D FEA model of the AFM tip-substrate contact for the half-space material is performed since Hertzian contact theory can be used for comparison in this case. According to the convergence analysis, the simulated contact stiffness for a half-space converges to values obtained from Hertzian contact theory with less than 1% difference for different materials. Although this result verifies the FEA

approach, it does not provide a comparison for the simulation of the finite size subsurface defects. For this purpose, ultrasonic AFM experiments have to be performed. The verification studies are explained in detail in the third chapter.

2.4.2 Imaging Simulations of Finite Sized Cavities

One of the advantages of the 3-D contact model is the capability of the scanning simulation. To demonstrate this capability, the effects of a spherical cavity on the contact stiffness for a surface scan are simulated. The cavity under investigation has 300 nm radius and the center is 500 nm under the silicon surface. The contact force of 1 μN and 100 nm tip radius are used during the scan. The contact stiffness distribution on the surface of this case is shown in Fig. 10. The silicon half-space causes the contact stiffness of 1427 N/m in the simulations for the given parameters. The lowest contact stiffness resulted by this spherical cavity is 1411 N/m, while an infinitely long cylinder with the same radius and depth has 1395 N/m of contact stiffness on the softest spot.

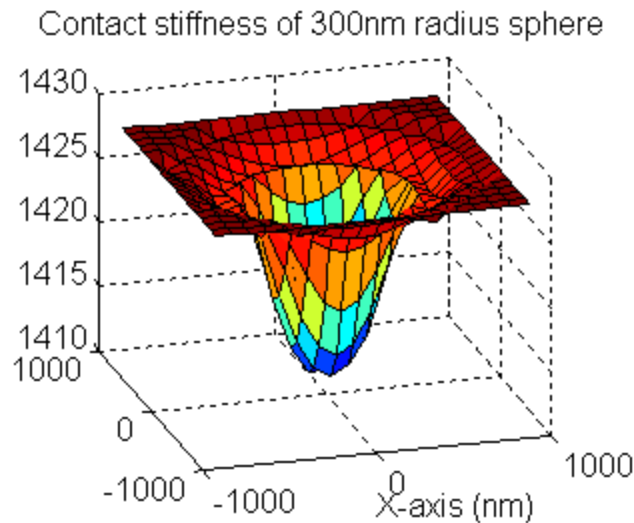


Figure 10 The contact stiffness simulations for an embedded spherical cavity [65].

The 3-D contact model also provides information on the effects of the multiple subsurface structures. As an example, two cylindrical subsurface cavities in a silicon

substrate are simulated using 100 nm radius tip and 1 μN contact force. Both of these cavities are infinitely long and their height axis is parallel to the surface while their radius is 300 nm. The centers are 500 nm under the surface as depicted in Fig. 11 (b) and the distance between the centers of the cylinders is varied between 800 nm and 1.2 μm . According to the simulation results in Fig. 11 (a), the distance between the centers of the cylinders should be more than 1.2 μm so that the subsurface structures can be modeled as independent objects. Note that it is difficult to define a general rule for lateral and depth resolution since the distribution of the contact stiffness is a function of depth, width and material of the subsurface structure as well as the force and tip radius.

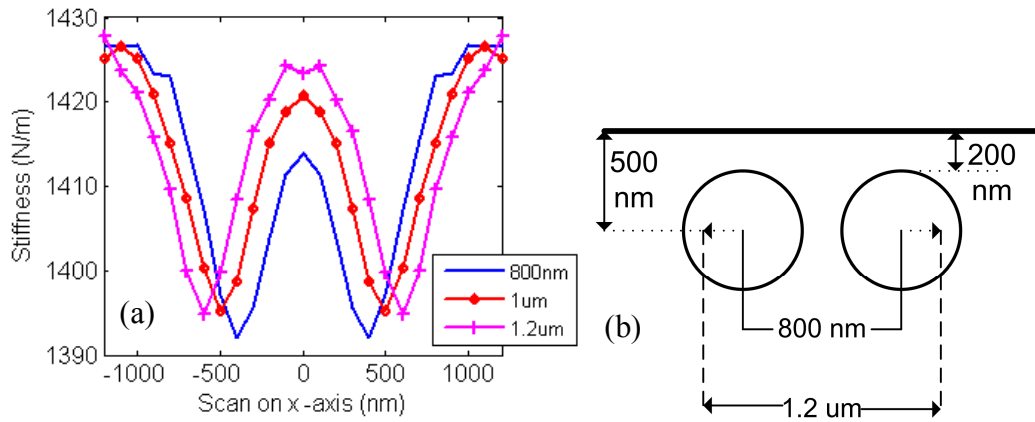


Figure 11 (a) Contact stiffness on a silicon substrate with two cylindrical cavities. (b) Schematics of the sample.

The tip radius and tip material have significant effect on the lateral resolution and depth in ultrasonic AFM applications [62]. However, the observed effects of subsurface structures on the contact stiffness depend on many other variables, such as contact force, material properties of the substrate, and the properties and shape of the subsurface structure. Because of this, it is easier to examine the effects of one variable while keeping the rest of them constant. First, how different force levels change the contrast of the

contact stiffness image is investigated. For this purpose, we apply 200 nN, 1 μ N and 2 μ N forces to the geometry depicted in Fig. 11(b) with a 800 nm distance between centers. Fig. 12 shows the normalized contact stiffness (k^*/k_{si}^*) results for this geometry, where k_{si}^* for each curve is the contact stiffness of silicon halfspace for that particular applied contact force level. When 200 nN of force is applied, normalized contact stiffness changes 1.5% (12.5 N/m for $k_{si}^* = 835$ N/m) as the tip scans over the cylindrical cavities. Thus, for example, these defects would barely be detectable in an ultrasonic AFM set-up with a 200 nN force assuming a minimum detectable Δk of 10 N/m. Higher forces provide better lateral resolution and contrast, because penetration depth is increased to the cylindrical cavities [65]. However, one should optimize the force carefully depending on the substrate and detection system since higher forces can be destructive while providing better subsurface images.

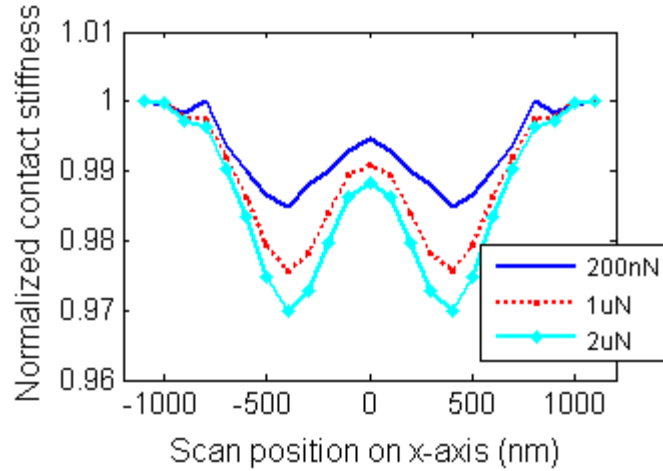


Figure 12 The normalized contact stiffness of the substrate with two cylindrical cavities with different forces [65].

2.4.3 Practical Example: Formation of an Electromigration Void

Electromigration in interconnects is one of the challenges for reliability of integrated circuits. To understand the formation mechanism of electromigration defects researchers

commonly use X-ray [32, 40] or FIB imaging [30, 66]. While the spot size of X-ray creates resolution problems, using FIB is destructive, and thus does not allow in-situ imaging. Therefore, subsurface imaging by AFM as a tool for in-situ observation of electromigration voids is investigated.

For these calculations, copper (Cu) lines with a 300 nm square cross section embedded under 100 nm of SiO₂ are simulated. X-ray techniques would have difficulty in detecting electromigration voids on 300 nm lines because of the larger spot size. However, AFM may provide better lateral resolution by making use of the small contact radius. To model the formation of the electromigration defects, we place a half-spherical void on the upper side of the Cu line as depicted in Fig. 13 (b). Then, contact stiffness on the surface is calculated for different radii of half-spherical cavity, simulating the growth of a void. In addition, the same calculation is done for a Cu line with a rectangular electromigration defect with a base of 300 x 300 nm and which completely breaks the electrical connection resulting in what is called a fatal defect. All calculations are done by assuming 100 nm of tip radius and 1 μ N of force. The results are presented in Fig. 13. As shown in Table 2, Cu is slightly stiffer than SiO₂. Since these two materials do not have much contrast in their elastic properties, scan on flawless Cu line indicates a slight (4 N/m) increase in stiffness. With the electromigration void in the Cu line, a reduction in contact stiffness is observed depending on the size of the defect. If the void has a 50 nm radius, the reduction is about 6 N/m. The slight increase in contact stiffness on either side of the 50 nm radius void is the result of having the stiffer Cu layer under the SiO₂ layer. When the radius of the defect becomes 70 nm, the simulation shows 18 N/m of contact stiffness change. More contrast on contact stiffness results as the defect is enlarged. The

stiffness change is 65 N/m for the fatal defect case, when the diameter of the void reaches the width of the line.

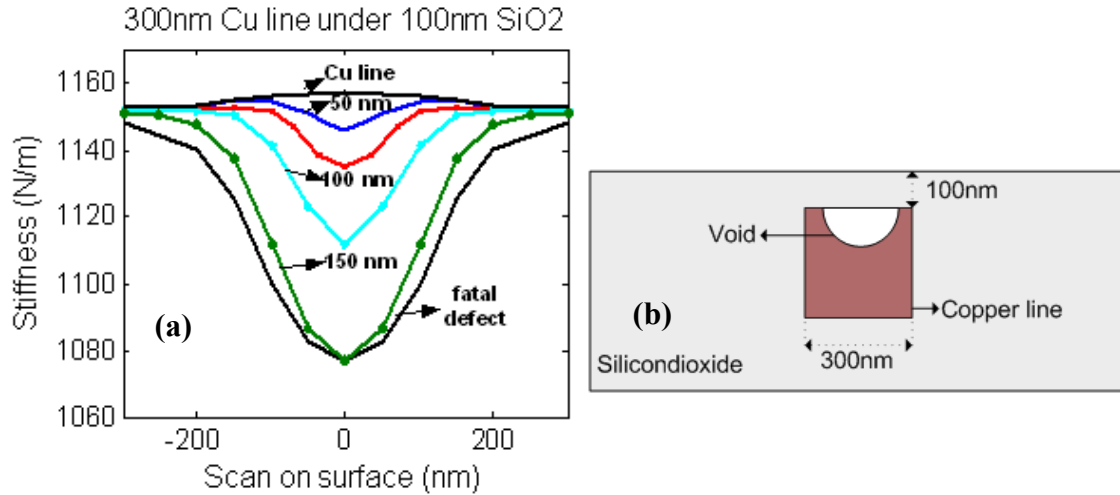


Figure 13 (a) The calculated contact stiffness on a Cu interconnect line with a electromigration defect.(b) The geometry of the simulated electromigration defect.

The results show that ultrasonic AFM is expected to provide better performance than X-ray during the electromigration void monitoring in thin Cu lines [65]. One of the shortcomings of ultrasonic AFM is the low penetration depth of the method. Although higher forces will provide an increase in the penetration depth, it may be destructive. Therefore, the material on the interconnect lines may need to be thinned down to about 100 nm. In addition, AFM cannot be used to detect electromigration defects under a via, since the necessary via height causes the defect area to be far from the AFM probe.

2.5 Chapter Summary

To be able analyze the elasticity of samples, proper modeling of AFM tip-sample contact is necessary. Previously analytical and finite element models are used by researchers to analyze half-space substrates and substrates with layers. In this study, a 3-D subsurface imaging model by finite element analysis is implemented. This model can

simulate scan of AFM tip on a sample with finite size nano-scale subsurface structures. The resolution on embedded structures, the effects of subsurface structure materials and shapes, and practical cases are investigated by employing this 3-D model.

CHAPTER 3

EXPERIMENTAL VERIFICATION OF THE 3-D FINITE ELEMENT ANALYSIS MODEL

3.1 Ultrasonic Methods of AFM

The sensitivity limitation in the force curve measurements can be eliminated by using ultrasonic AFM methods. Ultrasonic methods of AFM rely on the dynamic stiffening of the cantilever in frequencies higher than the first resonance order. Several ultrasonic AFM techniques, such as atomic force acoustic microscopy (AFAM) [23, 25, 29, 67, 68], ultrasonic atomic force microscopy (UAFM) [26, 55, 69], and ultrasonic force microscopy (UFM) [28, 70], have been developed during the past decade. Most of these techniques use higher flexural or torsional vibration modes of the cantilever, which are detected by a photodiode while the cantilever tip is in contact with the substrate. In these techniques, the AFM tip and the sample are in contact with a well-known force, and the sample (or the cantilever) is vibrated in an order higher than first resonance frequency. In UFM, the vibration frequency is away from the cantilever's any resonance and the amplitude of the vibration is modulated so that the tip jumps off the contact periodically. In AFAM and UAFM, constant small vibration amplitude near the contact resonance frequency is applied to the AFM tip-sample contact by vibrating the sample or the cantilever. UFM can be used for understanding multiple surface properties but encounters problems when quantifying them, while AFAM and UAFM can provide sensitive elasticity information. In this work, AFAM is used as the material characterization method.

AFM cantilevers exhibit multiple resonance modes. The behavior of the cantilever beam in high frequencies can easily be determined by using well-known analytical expressions or finite element analysis (FEA) [71, 72]. Fig. 14 shows the shape of the cantilever for different contact stiffness, k^* , and cantilever stiffness, k , ratios in higher resonance modes. When the contact resonance mode is sensitive to a k^*/k value, the change on the cantilever vibration shape is the maximum. For example, first contact resonance mode is sensitive for k^*/k around 10 since the cantilever shape deviates from its free form. But when k^*/k is as high as 100, the first mode shape is nearly same as the fixed end. This means that, when k^*/k is 100, first contact mode cannot differentiate it from infinite stiffness. For k^*/k as high as 1000, the third resonance mode is the most sensitive of three orders. Since stiff materials like silicon (Young modulus of 135 GPa) and the contact force of 1 μ N results in around 1500 N/m of contact stiffness, someone interested in the sensitive elasticity measurements and subsurface imaging on the stiff materials should monitor the higher resonance orders.

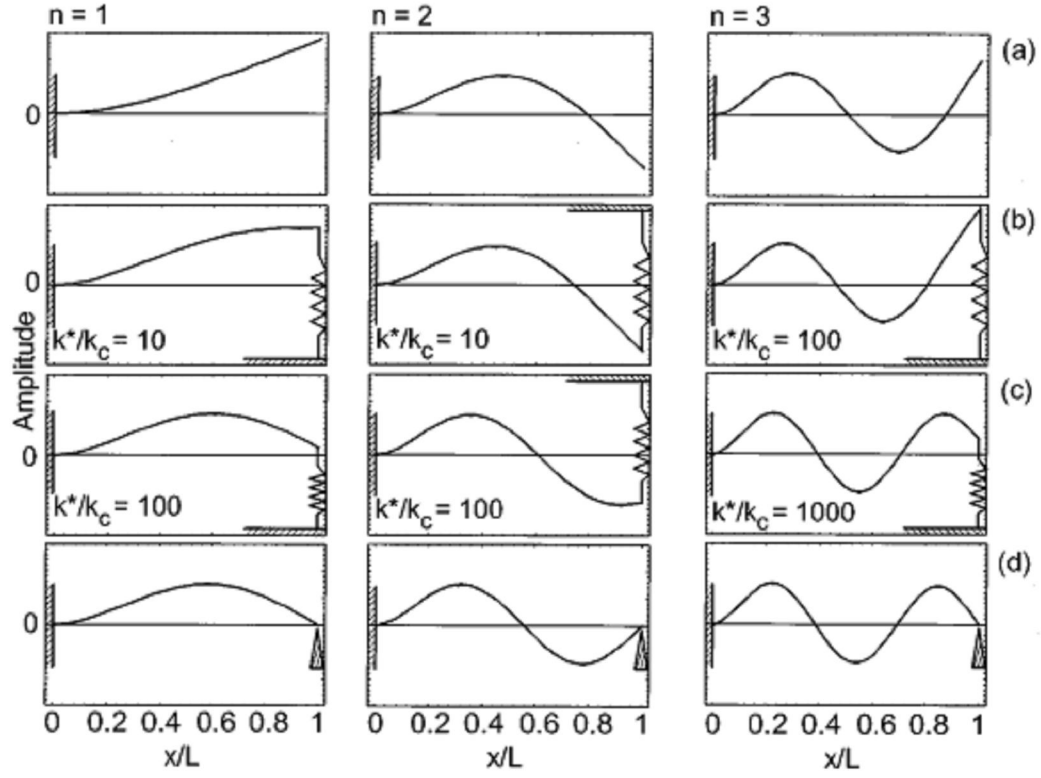


Figure 14 Calculated local vibration amplitudes along a cantilever with rectangular cross section for mode $n=1, 2$, and 3 (from left to right) for different values of k^*/k_c (from top to bottom).

The analytical expressions for the flexural and torsional resonances of a cantilever beam have been discussed by several authors [23, 72]. In these expressions, an infinite set of flexural modes are defined with wave number k_n and frequency f_n . The relation between k_n and f_n is:

$$\frac{k_n}{f_n} = \sqrt{4\pi^2 \frac{12\rho}{b^2 E}} = c_B \text{ and} \quad (3.1)$$

$$k_n L = c_B L \sqrt{f_n}, \quad (3.2)$$

where c_B is the characteristic cantilever constant, E is the Young modulus, ρ is the mass density, b is the width, and L is the cantilever length [25]. Although the repulsive and attractive forces are highly non-linear to the tip-sample distance, the contact spring can be

approximated as linear for small amplitudes. The simplified model of the cantilever in contact is shown in Fig. 15. In this model, cantilever has the length L , the tip is placed at position L_1 , and $L' = L - L_1$. The lateral stiffness of the tip-sample contact and damping coefficients are ignored in this simple model.

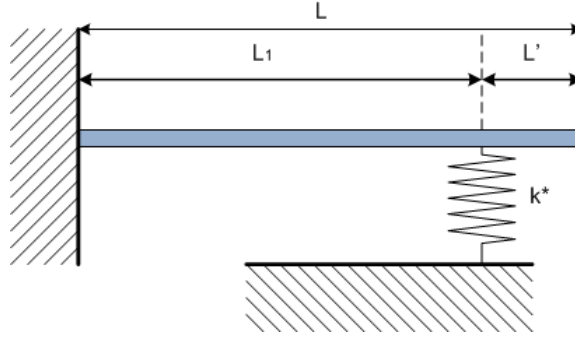


Figure 15 The simplified model for cantilever in contact.

The characteristic equation of the simplified model (Fig.15) for a contact stiffness k^* is [23]:

$$\frac{k^*}{k} \left[\frac{-(\cosh k_n L_1 \sin k_n L_1 - \sinh k_n L_1 \cos k_n L_1) \times (1 + \cos k_n L' \cosh k_n L') + (\cosh k_n L' \sin k_n L' - \sinh k_n L' \cos k_n L') \times (1 - \cos k_n L_1 \cosh k_n L_1)}{2 \frac{(k_n L_1)^3}{3} (1 + \cos k_n L \cosh k_n L)} \right] = \quad (3.3)$$

Since L , L_1 values and the thickness of the cantilever differ even in cantilevers from the same batch, a calibration step is required for each cantilever. First, the free resonance frequencies are measured and c_B is calculated using the free resonances. Then, contact resonances of the cantilever for two different contact forces on a well-known material have to be obtained. These two different forces will create two different k^* and f_n 's; by substituting those values into Eq. 3.3, one can solve the unknowns; L_1 and L . Although, L_1 and L values also can be measured by using SEM image of the cantilever, finding these values accurately is essential for the contact stiffness measurements. After

this point, since L_I , L , and c_B are known, observing the contact resonance frequency on any surface is enough to calculate k^* . As a result, one can calculate elasticity of a surface from k^* by using Hertzian contact theory:

$$k^* = \sqrt[3]{6E^*R F}, \quad (3.4)$$

where E^* is reduced Young's modulus (calculated by Eq. 2.8), R is the radius of the indenter and F is the contact force.

AFAM can evaluate k^* by detecting the flexural mode resonance frequencies. Since the value of k^* is a function of the mechanical properties of the substrate [26, 73], these methods offer the ability for material characterization [63, 64]. Not only the material type of the substrate but also the presence of the nanostructures in the penetration depth changes the contact stiffness [43, 59, 68, 74, 75]. To carry out subsurface imaging experiments, an AFAM setup is implemented. The AFAM setup is depicted in Fig. 16.

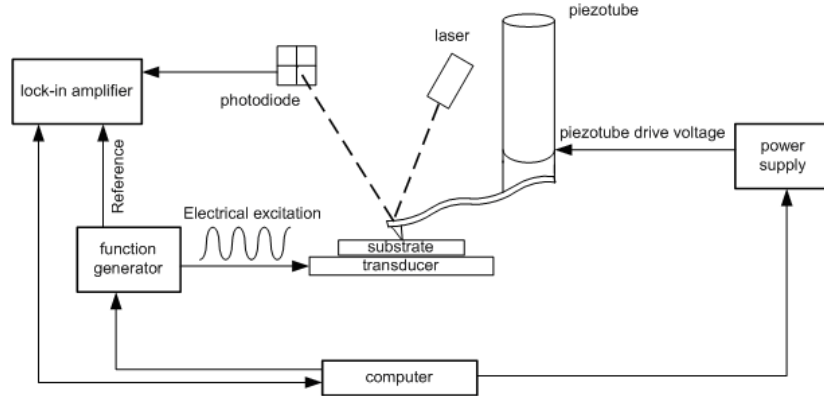


Figure 16 Schematic of the AFAM setup.

The AFAM setup can be constructed by modifying a commercially available AFM system. In this setup, the substrate is bonded to a piezoelectric transducer that generates out-of-plane vibrations while the cantilever tip and the surface are in contact with a DC force. A function generator synchronized with the lock-in amplifier excites the

piezoelectric transducer with a sinusoidal voltage, which in turn vibrates the sample. The feedback system of the AFM keeps the contact force constant; while the vibration of the surface is coupled to the cantilever and the cantilever bending is detected by the bi-cell detector. The lock-in amplifier measures the RMS value and the phase information of the photodiode output at the ultrasonic excitation frequency. The lock-in amplifier output is acquired and the frequency response on each pixel of surface can be obtained from this output. One can obtain contact resonance frequencies on each pixel and eventually calculate the contact stiffness.

Different materials cause different contact stiffnesses for the same contact force (Eq. 3.4) and these stiffness changes create shifts in the contact resonance frequencies. The frequency spectra on silicon and photoresist presented in the work of Crozier et al. [59] are shown in Fig. 17. Since photoresist is softer than silicon substrate, the contact stiffness and the contact resonances are lower. The presence of the substructures and layers may change the stiffness on the surface compared to the bulk media and AFAM is capable of detecting even minor changes due to the high quality factor of the cantilever.

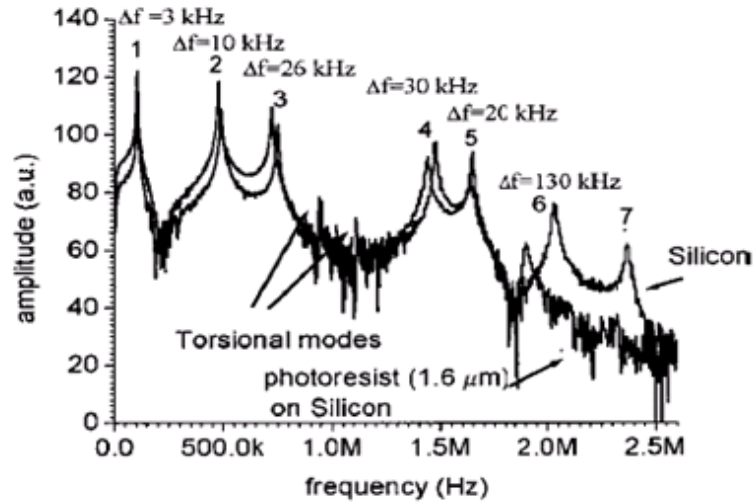


Figure 17 Frequency response of an AFM cantilever while it is in contact with photoresist and silicon [59].

3.2 Ultrasonic AFM Experiments for the Verification of the 3-D FEA Model

For experimental verification of the 3-D FEA contact model, an ultrasonic AFM set-up and a sample with a well-known finite size subsurface structure are needed. AFAM set-up described in Fig. 16 is implemented. The resonance frequency of a selected contact mode is measured at each point of the scan and the data is stored in the computer for further processing. The x-y piezo of the AFM is used to move the cantilever laterally to scan the sample. The lines of $2.8\ \mu\text{m}$ with 50 data points are scanned in the presented experiments. A commercial AFM cantilever with $3\ \text{N/m}$ stiffness and free resonance frequency of $42.4\ \text{kHz}$ is used for conducting experiments. Because of the lateral forces AFM tip radius may change during the scanning, so the tip is blunted intentionally before running the set-up. To extract stiffness information from the contact resonance frequency data, parameters depending on the cantilever dimension and the tip location on the cantilever are obtained before the experiments. The calibration data is used to interpret the resonance frequency shifts by using analytical models. According to these models, the

steps of 500 Hz in the frequency sweep cause 8 N/m steps in stiffness measurement and this step size provides enough sensitivity for subsurface imaging. MATLAB 7.4 Instrument Control Toolbox is used for programming of instruments and data acquisition [76].

In the AFAM experiments carried out on this sample, frequency sweep range is determined to be around 1.21 MHz for a 1 μ N contact force. Third contact mode appears around 1.21 MHz, which is not affected by the lateral forces as much as the lower modes [72], so the possible effects of lateral forces are ignored in this work. According to the extracted contact stiffness data, the AFM tip and half-space silicon contact has 1702 N/m stiffness for 1 μ N contact force. With these values, assuming a spherical tip and the mechanical properties shown in Table II, the tip radius is calculated as 173 nm by Hertzian contact theory. Since the SEM image of the AFM tip shows approximately 245 nm radius of curvature for the tip, the calculated value is acceptable for further analysis.

A suitable sample is as important as the experimental set-up to verify the 3-D FEA model. The sample should have a smooth surface, well known material properties, and well-defined subsurface structures. A simpler method than previous works [62] is followed to fabricate the test sample and focused ion beam (FIB) (Nova Nanolab 200) system is used for fabrication. Conical shaped cavities are milled from the side of a silicon piece at different dimensions and depths from the surface. The conical cavity used for the experiments here has 500 nm radius at the widest point (base) located under approximately 50 nm silicon and the estimated height is 3 μ m.

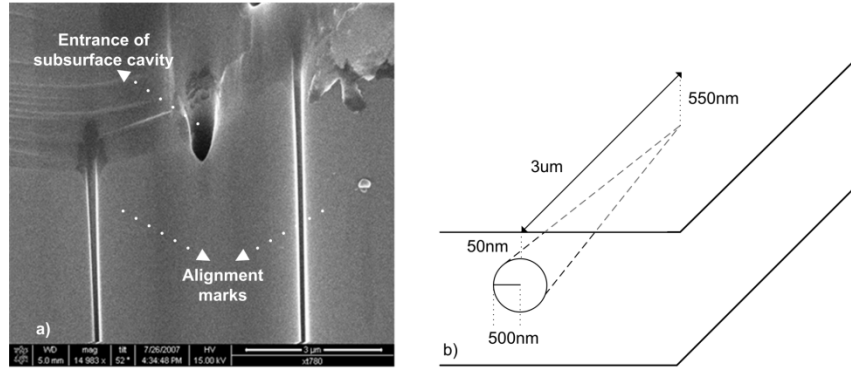


Figure 18 (a) SEM side view of the substrate used in the experiments. (b) Schematic of the subsurface cavity structure.

Although topography creation is avoided with this sample fabrication procedure, some particles are unintentionally located around the area of interest. These particles limit the imaging area for contact stiffness measurement. During the experiment, the contact stiffnesses of 3 different lines are measured after taking the AFM image of the substrate (Fig. 19). According to the calculations, at the lines represented as A, B, and C, holes have radii of 315 nm, 350 nm, and 465 nm while their centers are 550 nm under the surface. The typical topography on these lines is plotted in Fig. 19(b). The maximum topography is 6 nm on 1 μm scan.

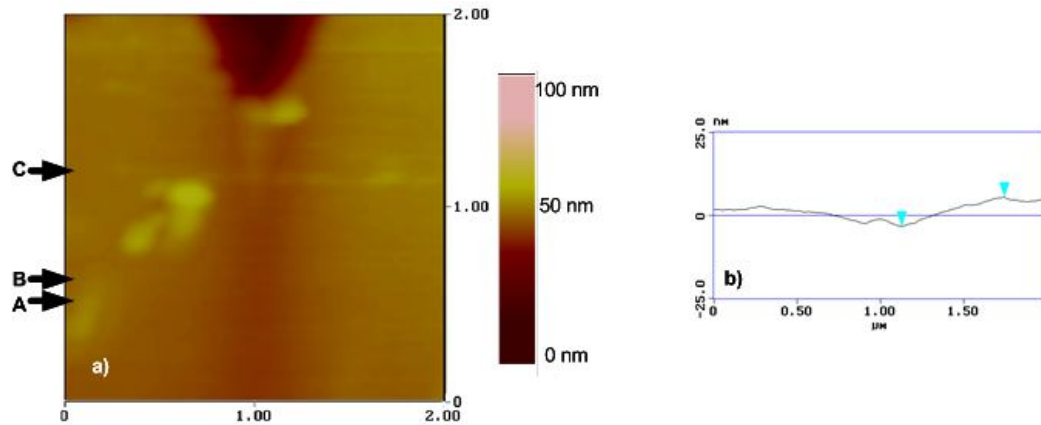


Figure 19 (a) AFM topography image of the substrate. Scan size is 2 μm x 2 μm. Arrows A, B, and C in (a) represent the lines where the measurements are performed. (b) Cross section of sample surface on line C, showing maximum 6 nm height difference.

The experimental and simulated contact stiffness results obtained on the lines A and B are shown in Fig. 20 (a) and 20 (b). The observed tilt from the line A to the line B in experimental data can be either a result of the shift in the lateral piezo position or the direction of subsurface structure. For the line C, the cantilever tip is moved closer to the entrance of the cavity. At this location the subsurface cavity has an approximately 465 nm radius. The experimental and simulated contact stiffness results of line C are presented in Fig. 20 (c). For comparison, the simulation results are plotted on the experimental data.

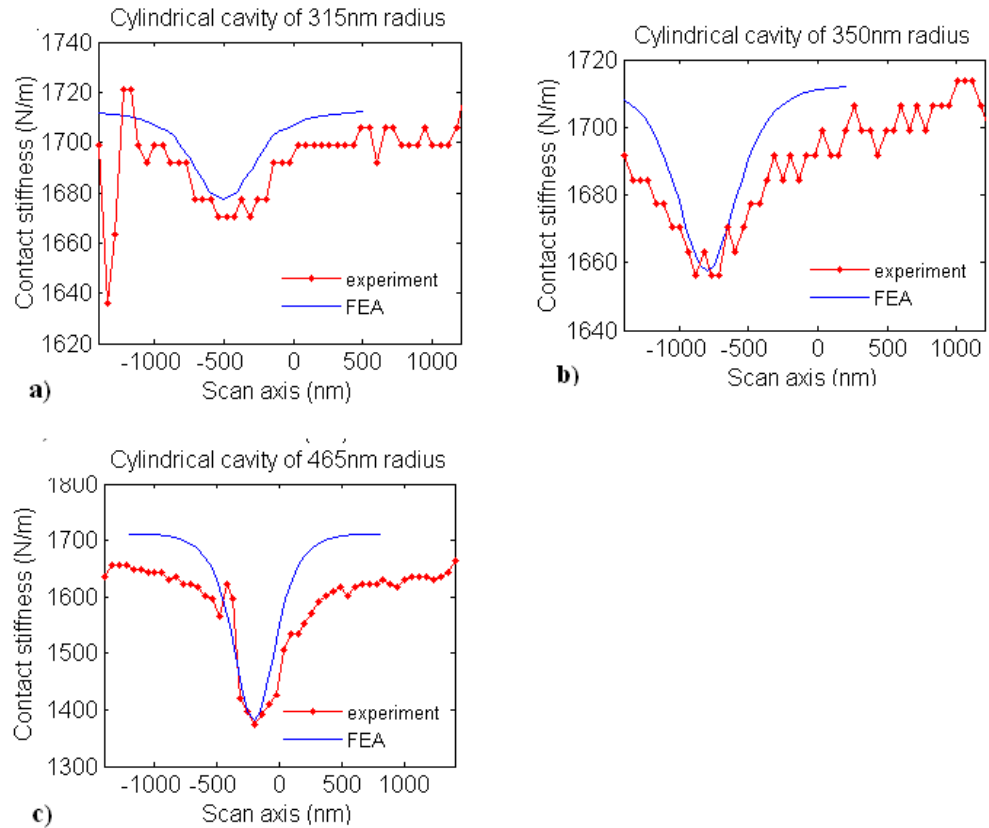


Figure 20 Comparison of experimental and simulation scan data for (a) 315 nm, (b) 350 nm, (c) 465 nm radius of cylindrical cavities [65].

Note that in the FEA simulations, there are no fitting parameters except for the estimated tip radius, cavity radius and cavity depth. The contact force is measured and silicon material properties (see Table 2) are used. Given these conditions, the agreement of the measured and simulated contact stiffness values are remarkable for all cases. Maximum difference from the contact stiffness on bare silicon surface is around 3% for Fig. 20 (c). For Fig. 20 (a), experiment suggests a 1670 N/m contact stiffness at the center of the cavity while the simulation gives 1678 N/m for the same point. Also note that, according to the calculations, there is a 235 nm silicon layer over the smallest cavity and this structure is still detectable through the contact stiffness measurement at the surface. In Fig. 20 (b) and 20 (c), the simulated contact stiffness changes more rapidly than the experimental results. The reason can be that either the cavities are not perfect as the constant radius cylinders assumed in FEA, or additional thinning on the substrate occurred on these lines, which are closer to the entrance of the cavity. Nevertheless, given the experimental uncertainties and possible errors, these results justify the use of the 3-D model for analyzing other types of defects and subsurface structures on the AFM tip-substrate contact [65].

3.3 Application of the 3-D FEA Model and Discussion

In the second chapter, the 3-D FEA model is used to predict the effects of several defect geometries, as well as imaging parameters such as contact force on ultrasonic AFM. In addition, since this model can evaluate the effects on the contact stiffness caused by multiple subsurface structures with more complex geometries, the resolving power of ultrasonic AFM for certain types of defects is investigated. A practical example of subsurface defect such as electromigration voids in microelectronics interconnects is

also presented in the second chapter. After the experimental verification of the 3-D FEA model, it can be concluded that the results presented in chapter 2 are validated.

According to the experimental data, the particular AFAM set-up developed can detect 10 N/m or more of contact stiffness change. Thus, the minimum detectable contact stiffness change, Δk , is 10 N/m. If the simulation results are analyzed with this information, one can decide on what kind of subsurface structures are detectable. For example, when there is a spherical cavity of 300 nm radius under 200 nm silicon material, the contact stiffness change is 16 N/m on the softest spot, which is barely detectable by the current set-up (Fig. 10). However, if a cylindrical cavity of the same radius and position is imaged, the contact stiffness change is 32 N/m and this cavity can be detected much easier.

According to the model, an electromigration void creates 18 N/m contact stiffness decrease under 100 nm SiO₂ when its radius reaches 70 nm (Fig. 13). It means that the early stages of an electromigration defect can be detected on a very thin interconnect in a non-invasive manner.

3.3.1 Effects of Elastic Properties of Subsurface Structures

One interesting parameter to investigate is the effects of the elastic properties of the substructures on the detection limits. For this purpose, long cylindrical inclusions in silicon made of SiO₂ and tungsten as practical materials (see Table 2) are simulated. To simulate the limiting cases, the results for a cylindrical cavity or a perfectly rigid inclusion of the same shape are generated. A contact force of 1 μ N and tip radius of 100 nm are used in the simulations. As mentioned before, the minimum detectable contact stiffness change, Δk of 10 N/m is calculated for the constructed AFAM set-up. In Fig. 21,

the minimum defect size and depth required for the detection of these subsurface defects are plotted. Each line shows the depth and the radius of the corresponding inclusion that results in Δk of 10 N/m in contact stiffness. For each material, the region to left of the contours shows the detectable range of the cylindrical defect radius and depth. According to Fig. 21, when there is higher contrast between substrate and structure, smaller inclusions can be detected. As expected, subsurface structures with mechanical properties with large contrast as compared to silicon can be detected easier at larger depths. Consequently, the lines corresponding to rigid structure and void defects are the rightmost curves. Similarly, the tungsten inclusion generates more contrast than a similar silicon dioxide structure. Rigid inclusions can be detected easier than the voids of similar size when they are close to the surface. The steep increase in detectable rigid cylinder radius shows that the penetration depth for this type of defects is limited to about 280 nm regardless of its size for this particular tip radius, tip and substrate material. In contrast, a void located deeper in the substrate can still be detected if it has large enough diameter. Note that although the results in this figure are valid for this particular example they can serve as a guideline for subsurface detection.

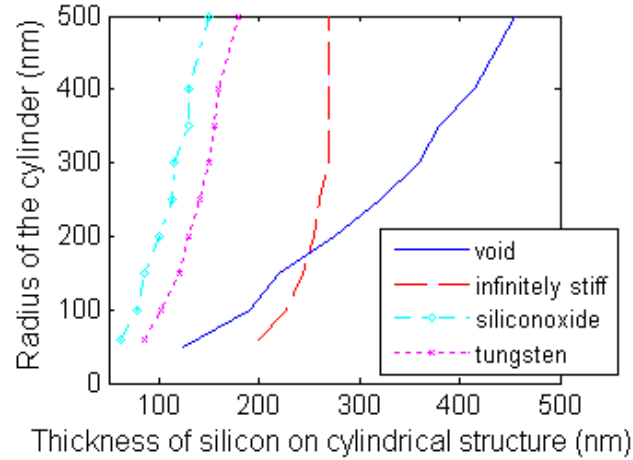


Figure 21 The detection limit contours for the cylindrical defects in silicon substrate [65].

3.4 Chapter Summary

Ultrasonic AFM methods provide sensitive contact stiffness measurements even on stiff samples and have been used by researchers for quantitative contact stiffness imaging on heterogeneous materials. In this research, an ultrasonic AFM method –AFAM– is used to verify the 3-D subsurface imaging model presented in second chapter. An AFAM set-up is constructed and a special sample with well-known subsurface structure is fabricated. The verified 3-D model can be employed for predicting the contact stiffness images of samples and also for determining the detection feasibility of the subsurface structures [65]. The results presented in this thesis are focused on AFM tip-sample contact and they can be used as guidelines for subsurface imaging by AFM.

CHAPTER 4

MECHANICAL PROPERTIES IMAGING BY MEASURING TIME-RESOLVED INTERACTION FORCES

Intermittent contact mode is the preferred mode of topography imaging by AFM when the lateral forces and the friction on the surface have to be avoided. In this broadly used mode, interaction forces between the probe tip and the sample are minimized and the tip taps the surface lightly. Tapping mode (TM) AFM is the most common intermittent contact mode of AFM. In the TM AFM, an AFM probe is vibrated with an AC signal –usually in the vicinity of the probe’s resonance– and the contact of the tip with the surface decreases the vibration amplitude. The feedback control keeps the probe base-sample distance constant by using the vibration amplitude as a parameter and follows the topography. During the TM AFM, the tip interacts with the surface periodically and this interaction contains crucial information about mechanical and chemical properties of the sample [36, 77, 78].

4.1 Methods of Material Characterization by Tapping Mode AFM

4.1.1 Imaging the Phase

When the AFM tip scans the surface with TM, the vibration amplitude is kept constant by using the feedback circuit. Another component of the vibration is the phase of the taps, which is not controlled by the feedback. The phase shift in the detection signal leads to the high contrast images of relative material properties and can be used to determine different materials deposited on a surface [44]. Since the phase shift is associated with attractive-repulsive state transition, viscoelastic properties, adhesion

forces, and friction; it can be considered as a map of dissipated energy during the taps [44, 79] and the quantitative interpretation of the phase shift in terms mechanical properties is not trivial [44, 77, 79, 80].

Quantitative expression of the phase shift has been studied by several authors. In addition to this, researchers have introduced different TM AFM methods that utilize phase data as the material characterization tool. One of these methods is called bimodal AFM, in which the probe is vibrated with the first and the second flexural vibration modes [81]. While the amplitude of the first mode is used to image the topography, the second mode is not controlled by the feedback mechanism and the phase of the second mode shows high contrast due to the surface properties [82, 83].

4.1.2 Harmonic Imaging

The detected taps on the surface during the TM AFM are time-dependent periodic signals. Imaging the harmonic content of the detection signal can be used for material characterization by TM AFM hence the impact with the surface gives rise to higher harmonics. However, the frequency spectrum of a regular AFM cantilever is complicated with multiple resonance modes and obtaining mechanical properties of the sample requires extensive mathematical modeling and data processing [45, 78, 84]. Since the amplitudes of the harmonics are influenced by the resonance frequencies of the frequency spectrum, the acquired tip-sample interaction forces are hard to analyze as shown in Fig. 22 [78]. The attractive and repulsive forces occur in the small time duration of a tapping period but the complex dynamics of the cantilever moves the tip even when the tip does not interact with the surface.

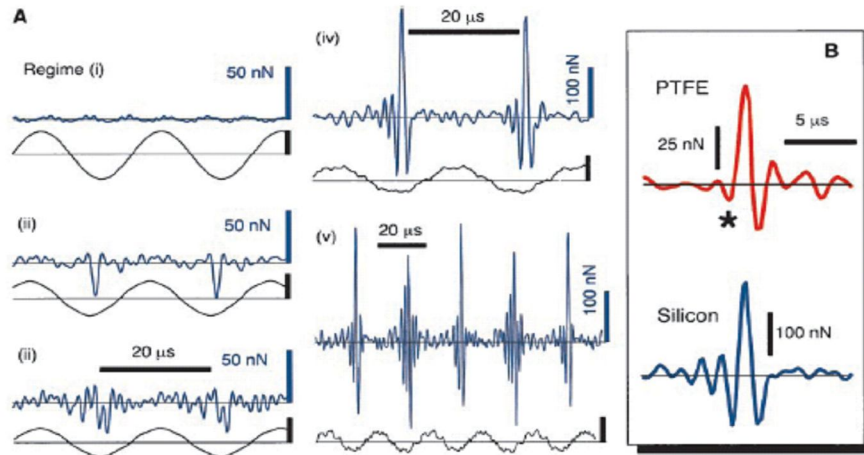


Figure 22 (A) The reconstructed interaction force and photodiode outputs. Free oscillation is shown in (i), whereas (ii) is the attractive force region. (iv) Repulsive forces become dominant and exceed 200 nN. (B) Taps on different materials [78].

One of the methods that exploits the dynamics of the regular AFM cantilevers is to actuate the cantilever by a submultiple of the fundamental resonance frequency and to measure the harmonic at this fundamental resonance [46, 85]. Sahin et al. proposed another method called harmonic cantilevers (Fig. 23) in which an AFM cantilever is tailored to have a resonance frequency in a higher harmonic [86]. Observing the harmonics is helpful for elasticity imaging but obtaining time-resolved tip-sample interaction force signal is still necessary for extensive material characterization since the attractive forces have an impact on the harmonic content.

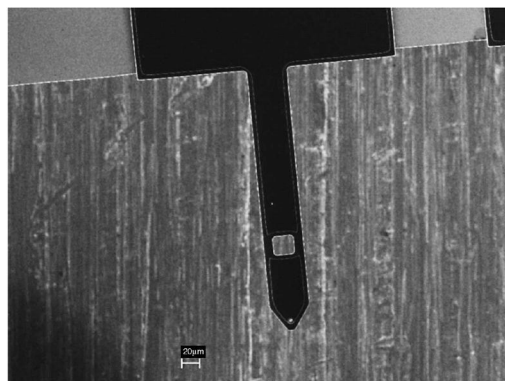


Figure 23 SEM image of a harmonic cantilever [86].

The flexural frequency response of the cantilever shows multiple higher-order modes around the higher harmonics while the torsional frequency response has one resonance at a very high frequency. Torsional harmonic cantilevers (THC) are based on this property and they are designed with a tip that has an offset from the axis of the cantilever as shown in Fig. 24 [47]. The cantilever is still vibrated in the first flexural mode while the interaction forces cause torsional vibrations in the harmonics of the first mode. Correcting the coupling from the flexural modes will provide the time-resolved interaction forces through the reconstruction of the harmonics.

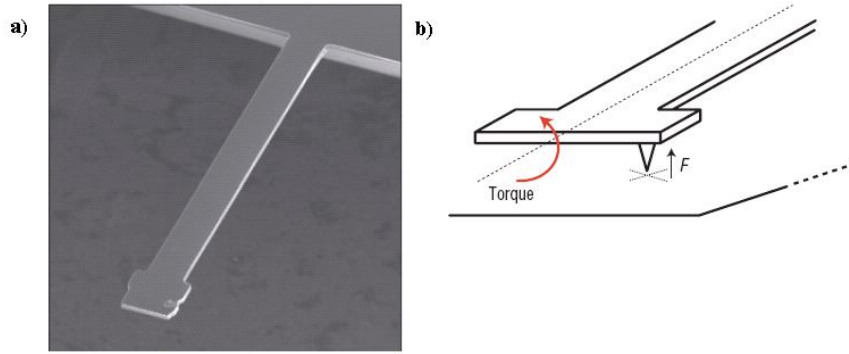


Figure 24 (a) SEM image of a torsional harmonic cantilever. (b) An illustration of the THC while it is tapping [47].

4.1.3 Time-resolved Interaction Forces Imaging

Measuring the harmonics of the taps is actually a way for constructing time-resolved interaction forces, which are valuable for material characterization. It is also possible to obtain interaction forces without mathematical reconstruction of the harmonics. One of the methods is to modulate the z-piezo at a frequency much lower than the resonance of the cantilever while the cantilever is resting. As the modulated piezo causes contact of the tip and the surface at a low frequency, deflection of the cantilever – interaction forces– can be measured in a time-resolved manner. The jumping mode [87],

pulsed-force mode [5, 22, 88], and peak-force AFM [89] are the examples of this method. Actually, these methods are more similar to force curve measurements than TM AFM since the z-piezo is modulated and the probe is kept still until it reacts to the interaction force. However, they are much faster than the usual force curves and they can image the mechanical properties of a surface while obtaining the topography. Although the z-piezo modulation frequency is lower than the first resonance frequency of the cantilever, ripples with that frequency occur in the tap due to the high Q of the probe. These additional ripples are usually removed by filtering while processing the data. For sensitive operation, one should select the appropriate probe that matches the contact stiffness during the operation. While using a soft cantilever for soft samples (softer than 500 MPa), the first free resonance frequency of the cantilever is close to the operation frequency and the results are not reliable due to the high Q of the cantilever (Table 1). Because of this, one should submerge the cantilever in fluid to create more damping and lower Q.

4.2 FIRAT Probes

Cantilever beams are known to have high Q with complex frequency spectrums. Imaging the time-resolved interaction forces is difficult with such a frequency response. To solve this problem, a micromachined pressure sensor based novel AFM probe with high bandwidth is introduced by Degertekin group in 2005 [51]. This probe has integrated interferometric optical detection and electrostatic actuation. It is called force sensing integrated read-out active tip (FIRAT) and in earlier designs a circular membrane or a doubly supported beam are used instead of the traditional AFM cantilevers. FIRAT probe consists of two parts; a micromachined electrically conducting beam fabricated on

a transparent substrate and a focused ion beam (FIB) deposited platinum tip (Fig. 25) [50, 90]. As seen in Fig. 25, electrically conducting gratings are deposited on the transparent substrate. The grating provides the diffraction of the light into different orders while the intensity of the orders depends on the gap height. The gratings are used for not only optical detection but also the actuation of the beam and biasing the beam to an optically sensitive point. Since the substrate is transparent, the laser goes through the substrate and reflects from the beam and the gratings. FIRAT has high bandwidth, interferometric optical sensitivity and electrostatic actuation capability and it can be used for fast imaging and time resolved interaction forces (TRIF) imaging.

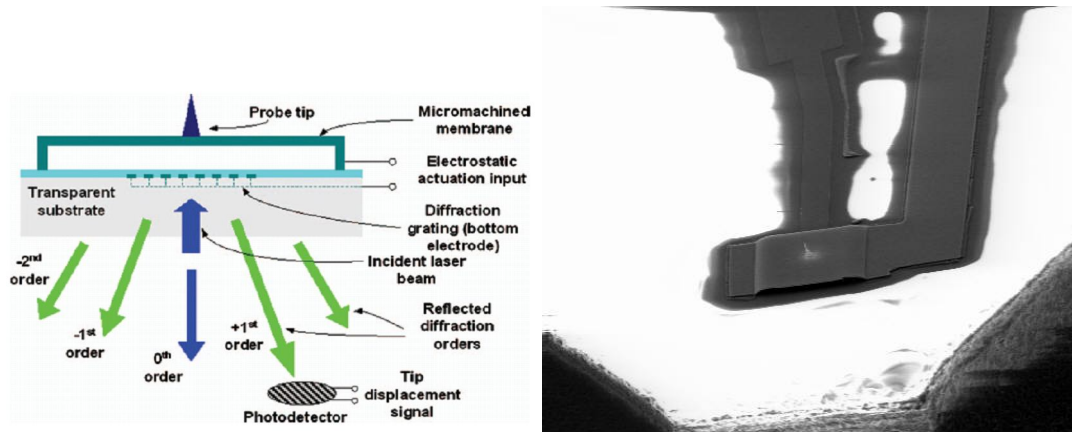


Figure 25 Schematic of the FIRAT probe and the diffraction based optical detection [50].

In the current TRIF mode of FIRAT set-up, the beam is biased electrostatically to an optically displacement sensitive position and the z-piezo of the AFM system is vibrated at 2 kHz (Fig. 26). This configuration is similar to the pulsed-force and peak-force AFM. The tip-sample interaction forces cause displacements in the beam and the laser intensity of the orders changes due to the displacement as the tip taps the surface.

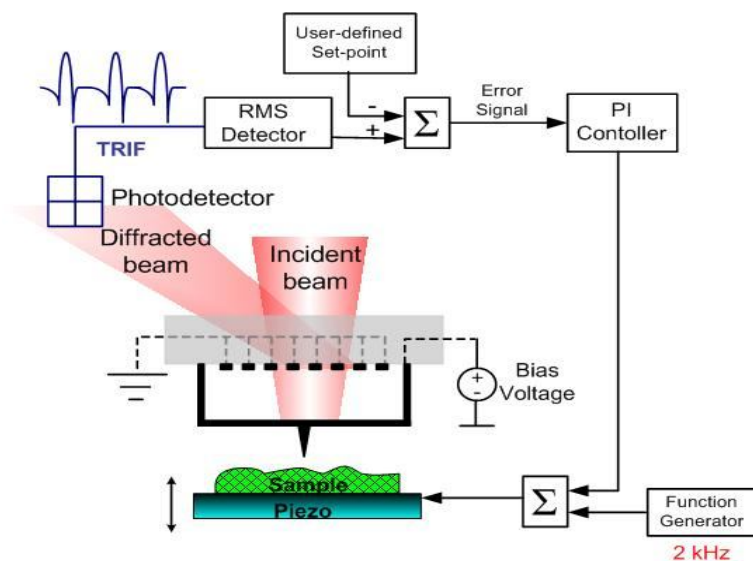


Figure 26 Schematic of the TRIF mode set-up.

FIRAT probe is designed to have a low quality factor and high cut-off frequency, so there is no ringing on the tap signals as in cantilevers [22, 49]. Recently, the real-time material characterization by TRIF mode of FIRAT probe has been demonstrated on different materials (Fig. 27) [52] without any complicated mathematical reconstruction [49, 91]. The tap signals clearly indicate attractive and repulsive forces. The repulsive force region provides elasticity of the sample while the attractive force peaks show the surface energy and the hysteresis of adhesion.

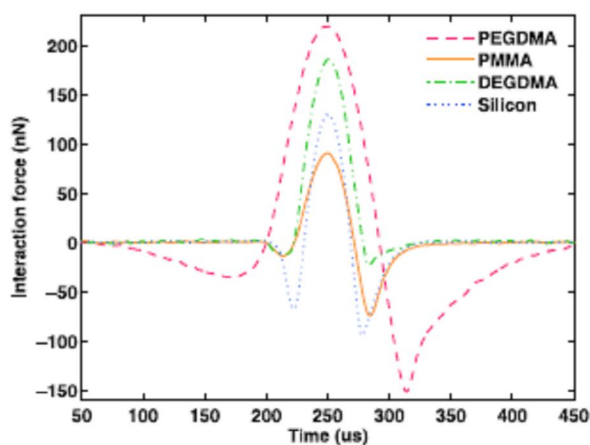


Figure 27 Experimental TRIF signals on different materials [52].

4.3 Modeling of the FIRAT Probes

4.3.1 Dynamics of FIRAT Probes

The deflections on the beam during imaging are small and the bias voltage is constant, thus it is possible to model the probe dynamics with mechanical elements. The FIRAT probe structure has stiffness and mass while the squeezed film between the probe and the substrate causes damping. One can use the electrical conjugates of these mechanical elements and create an equivalent circuit to examine the probe dynamics. The electrical conjugates of the force and the velocity are the voltage and the current in a circuit [92]. The equivalent circuit of the FIRAT probe is shown in Fig.28.

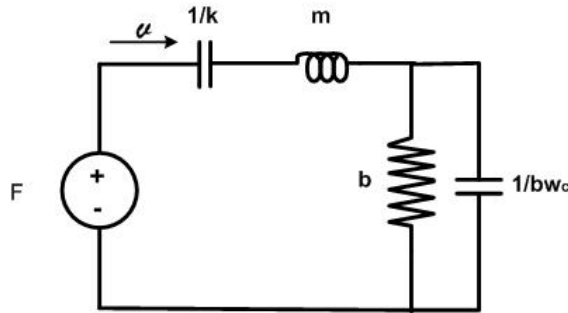


Figure 28 Spring-mass-dashpot model using a squeezed-film damping element [92].

In this equivalent circuit, the beam stiffness, k , is represented by a capacitor since it is also associated with the stored potential energy, while the mass, m , is added to the circuitry as an inductor. Damping may occur due to the loss in the beam structure and this loss will be the main source of damping when the probe is placed in vacuum. However, the mechanical loss in the beam structure is much smaller than the squeezed film damping caused by the small gap between the beam and the quartz substrate. The squeezed film damping, b , is added to the equivalent circuit as a resistor. The damping of the film dissipates energy as a resistor does and decreases the quality factor of the system.

Both a resistor and a capacitor are required for the modeling of the squeezed film since there are both damping and stiffening effects of the film. For the frequencies much lower than ω_c , only the damping component will be effective. When the film is vibrated at higher frequencies, the impedance of the film capacitor will increase and cause stiffening. The cut-off frequency ω_c is calculated by using the following equation:

$$\omega_c = \frac{\pi^2 h_0^2 P_0}{12\eta W^2}. \quad (4.1)$$

In this equation, h_0 is the gap height, P_0 is the ambient pressure, η is the viscosity, and W is width of the beam. The transfer function between the force, F , and the displacement, x , is shown below:

$$\frac{x(s)}{F(s)} = \frac{s / \omega_c + 1}{ms^3 / \omega_c + ms^2 + (b + k / \omega_c)s + k}. \quad (4.2)$$

Although it is possible to simplify this equation for different cases, the non-simplified version is applicable to a wider variety of probes. For very low frequencies, only the stiffness of the probe will be effective. As the frequency increases, the behavior of the probe becomes more complex. Fig. 29 shows the measured frequency spectrum of a FIRAT probe and the frequency spectrum of a matching equivalent circuit.

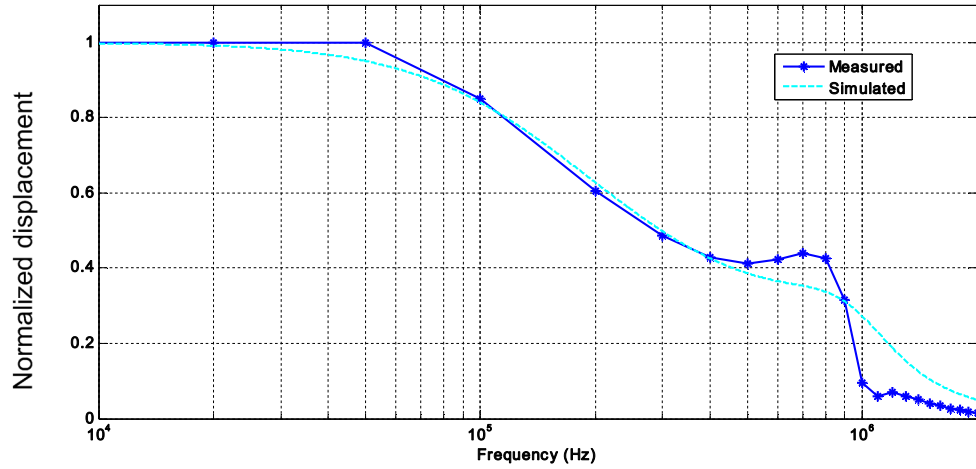


Figure 29 The measured and simulated frequency response of a FIRAT probe.

Quality factor (Q) of a regular FIRAT probe varies between 0.3-4 and is highly dependent on the gap height. The gap can be adjusted by applying a DC bias voltage and the probe dynamics can be tailored for the desired response. Meaning that, one can apply high DC bias and have a lower cut-off frequency or low DC bias voltage and obtain higher Q . In addition to the changes in the loss, the beam will be softer due to the spring softening effect when the DC bias is increased [92, 93]. The frequency spectrums of the FIRAT probe with 3 and 2.5 μm gaps are calculated by Eq. (4.2) and demonstrated in Fig. 30. In this figure, it is assumed that the gap is decreased by applying higher DC bias. Due to the softening effects, the spring constant of the probe is 0.6 times smaller than the higher gap case [93]. By decreasing the gap 0.5 μm , the cut-off frequency is reduced from 225 kHz to 65 kHz.

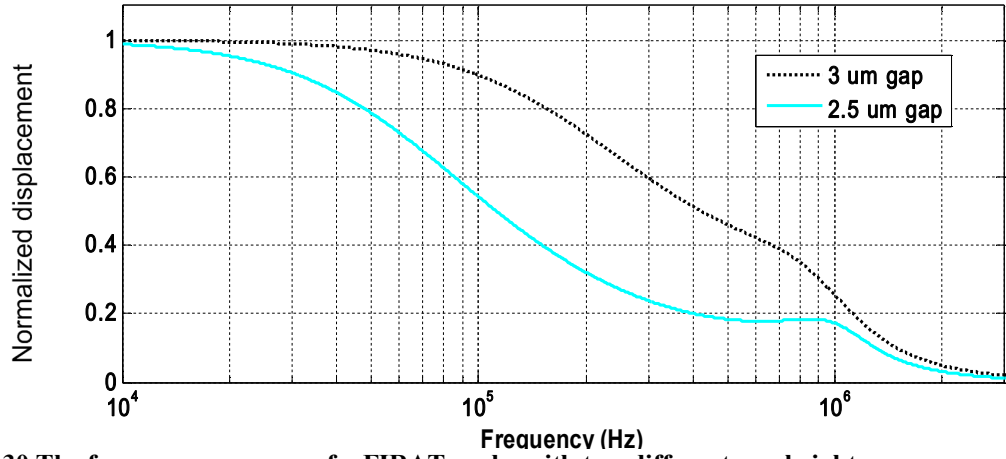


Figure 30 The frequency response of a FIRAT probe with two different gap heights.

As the z-piezo is actuated by a sine wave at 2 kHz close to the tip-sample contact, the probe tip goes through non-contact and contact regions of the tap periodically. The interaction forces between the tip and the surface cause deflection in the beam and this deflection can be monitored by using the PD output (Fig. 31). The tips of the current FIRAT probes are fabricated in a serial manner by FIB and they are not as reliable as the silicon tips. So, for testing purposes tipless FIRAT beams are used and the material to test is deposited on top of the beams. A silicon cantilever is placed to the z-piezo and used as a sample. Pentacene (a p-type organic semiconductor) [94, 95], which can be deposited in room temperature and ambient conditions, is imaged by this sample tip as well as the aluminum beam (Fig. 31).

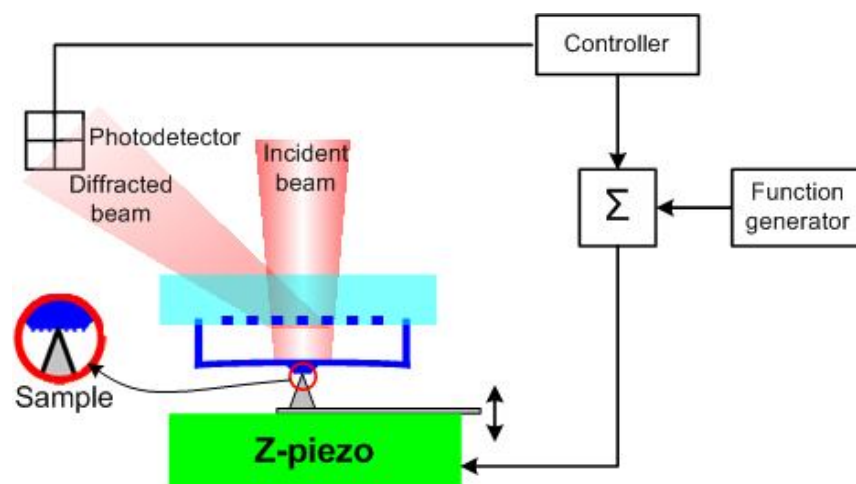


Figure 31 The experimental set-up of TRIF mode of FIRAT with a sharp tip.

The experimentally obtained time-resolved tap signals of one period are shown in Fig. 32 (a). The blue line represents the tap of a silicon tip on aluminum while the red line represents the tap of the same tip on pentacene. Although the tips are the same, the taps show different characteristics because of the material properties of the samples. One can clearly observe that the attractive forces are much higher when the taps are obtained on the pentacene sample. Another evident difference is the slope of the taps. In Fig. 32 (a), the taps are plotted in a time-dependent fashion. However, plotting the interaction forces versus the z-piezo movement is also helpful for analyzing material properties and the taps are plotted as force curves in Fig. 32 (b). As explained before, the slope of a force curve can be used to calculate the elasticity of a sample. In the Fig. 32 (b), it is obvious that pentacene is much softer than aluminum since the slope of the force curve is smaller. Note that, if a sample stiffer than aluminum was imaged instead of the pentacene, the force curves would not be as distinct as Fig. 32 due to the decreased sensitivity.

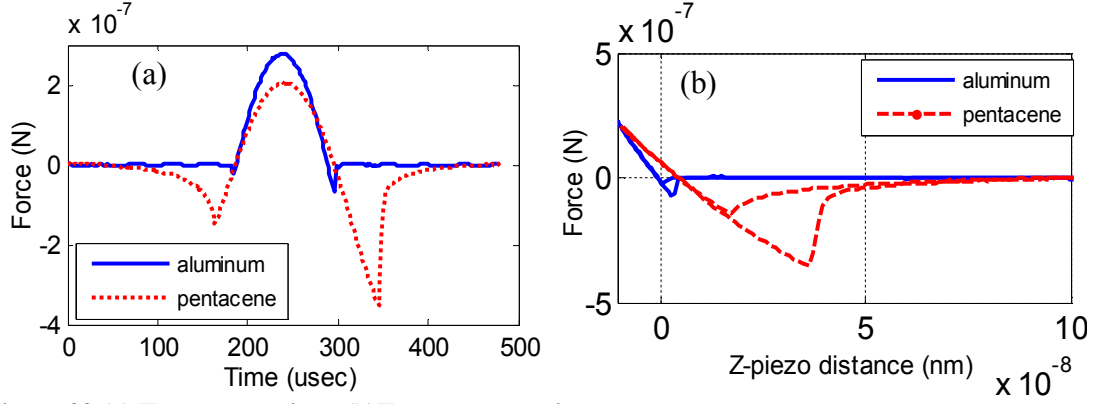


Figure 32 (a) Taps versus time. (b) Taps versus z-piezo movement.

4.3.2 Simulink Model of the FIRAT Probe

The interaction forces depend on the stiffness of the surfaces and the surface forces. Understanding these forces requires proper modeling, in which probe dynamics, material properties, and different operation possibilities can be studied. In addition to these, one can test data analysis accuracy by using model generated data. In this work, Simulink is used to model the TRIF mode operation of the FIRAT probes.

The experimental set-up for the TRIF mode of FIRAT probe is shown in Fig. 26. In this set-up, interaction forces will cause deflection on the beam depending on the probe dynamics. It is possible to model TRIF mode operation by using the block diagram shown in Fig. 33.

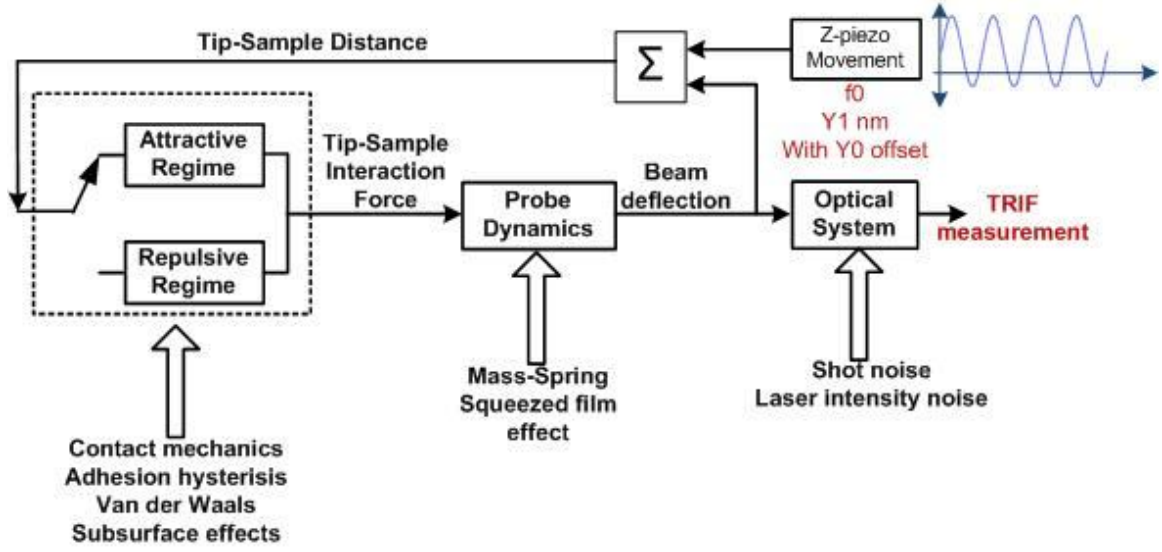


Figure 33 The block diagram of the taps on the probe. Sample properties, probe dynamics, and detection system is included in this model.

In this block diagram, the z-piezo moves at f_0 frequency with Y_1 amplitude and Y_0 offset distance from the surface. The piezo movement is defined by the following equation:

$$Z(t) = Y_1 \sin(2\pi f_0 t) + Y_0. \quad (4.3)$$

In the current experimental set-up, f_0 is 2 kHz, Y_1 is 57.5 nm. The tip-sample distance is used as a parameter for the interaction force calculation and different contact mechanics models can be applied for the interaction forces block. Depending on the tip-sample distance, either non-contact or contact model will be selected. The tip-sample distance, $d(t)$, is the sum of the probe deflection and the z-piezo movement.

$$d(t) = Y_1 \sin(2\pi f_0 t) + Y_0 + x(t). \quad (4.4)$$

The deflection, $x(t)$, is calculated by the transfer function in Eq. 4.2. To simplify the calculation of the tip-sample distance, one can compute $x(t)$ as $F(t)/k$ [52]. As the z-piezo

pushes the sample to the tip, the beam deflects. Since the probe is not a perfect spring and it has loss, the deflection is obtained after using the transfer function of the probe mechanics in the Simulink model. This transfer function can be calculated by using the probe dimensions. Experimentally obtained $x(t)$ and $Z(t)$ are plotted in Fig. 34.

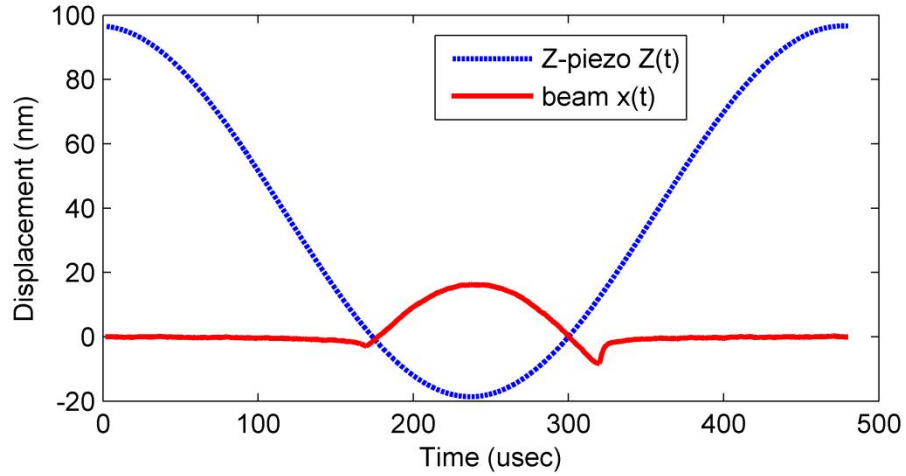


Figure 34 Experimental $Z(t)$ and $x(t)$ measured on the sample.

One factor that has not been accounted for in this model is the variation in the probe dynamics. The interaction between the tip and the surface can be linearized as a spring for the small signals. The addition of this spring changes the response of the probe and this change can be calculated after complicated analysis. For the FIRAT probe, the cut-off frequency increases during the repulsive force region while for the cantilevers fundamental resonance frequency is shifted. This property is not included in the current Simulink model.

The diagram shown in Fig. 33 is the basic Simulink model. It is possible to extend this model for the taps on the layered media, hysteresis, and different operation possibilities. This Simulink model will help to understand the effects of different probe dynamics on the obtained interaction forces. As an example, taps by two different probes

are simulated and shown in Fig. 35 (a) and (b). The first probe has a 143 kHz resonance frequency and a Q of 180, while the second probe has a 130 kHz cut-off frequency and a Q of 0.43. When the probe has a high Q and low resonance frequency, the interaction forces may require post-processing and this may alter some of material characterization results. Similar cases are studied with FIRAT probes (Fig. 35 (d)) and AFM cantilevers (Fig. 35 (c)).

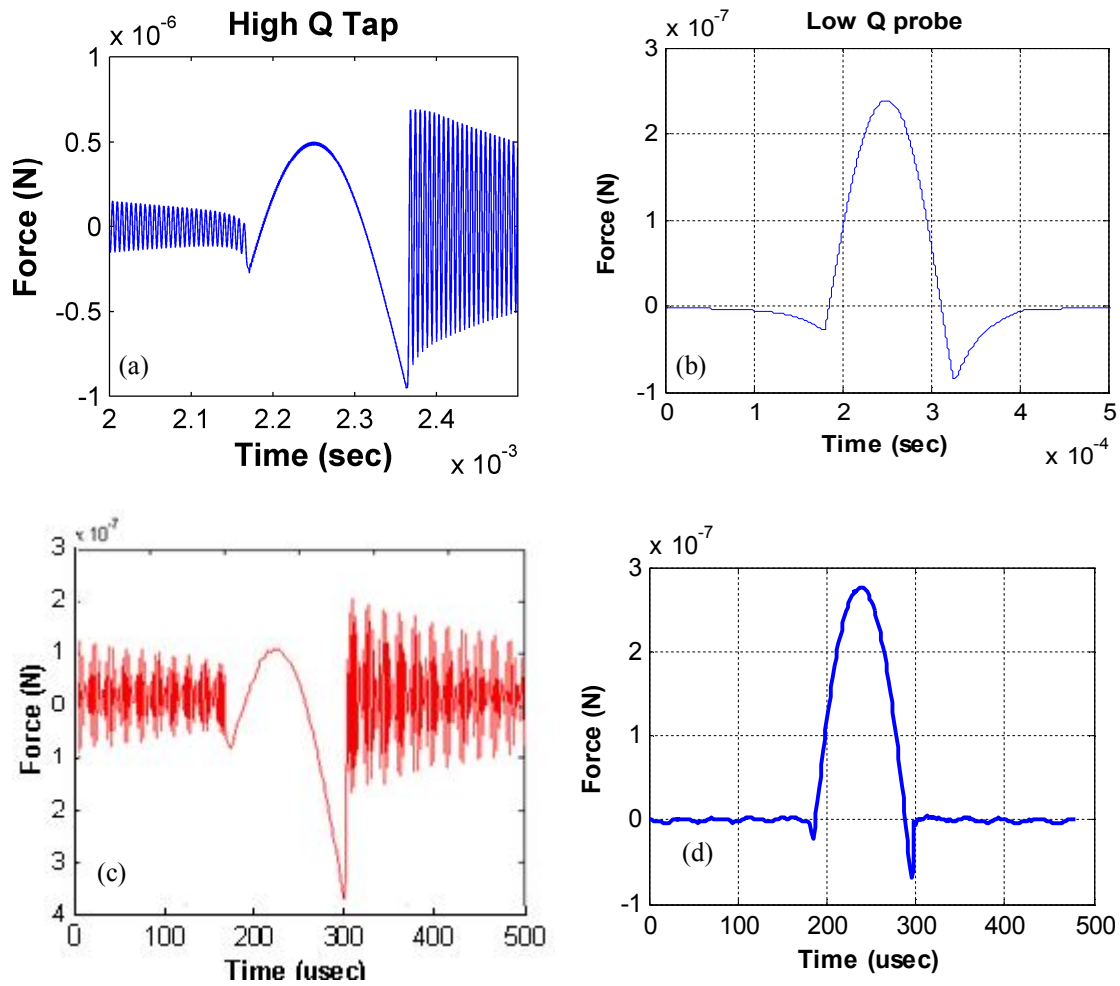


Figure 35 Taps simulated for a high Q (a) and low Q (b) probe. Taps measured by using a cantilever (c) and FIRAT probe (d).

4.3.3 Theoretical Modeling of the Interaction Forces

4.3.3.1 Surface Forces during the Non-contact Region

When two bodies are brought together, surface forces are always present but these forces become more apparent at small scales. For characterization of materials at the nanoscale, the surface forces are valuable and a part of the characterization process.

In TM AFM, TRIF mode of FIRAT probe, and nanoindentation, the probe tip approaches to the surface, makes contact with it and then it is separated. This cycle is called advancing/receding or loading/unloading. Although repulsive forces dominate during the contact region of this cycle, both attractive and repulsive forces occur while the tip and the surface are approaching and separating. These surface forces can be present both in vacuum and in solutions –like air–. In this section, the focus is on the surface forces that appear during the operation of the FIRAT probe in air.

The following figure shows the schematic of the force law between two bodies. In Fig. 36, one of the bodies is attached to a non-stationary base by a spring while the second body is fixed. This schematic can also be applied to FIRAT probe. The upper base is the z-piezo and it is actuated at 2 kHz. As the bodies approach, interaction forces become effective and the spring deforms. If the deflection of the spring can be measured and the vibration of the base is well-defined, one can calculate the distance, D , and the force, F . A typical force law curve is shown also in Fig. 36. Please note that, in Fig. 32 (b) force versus D is plotted while in Fig. force versus D_0 is plotted.

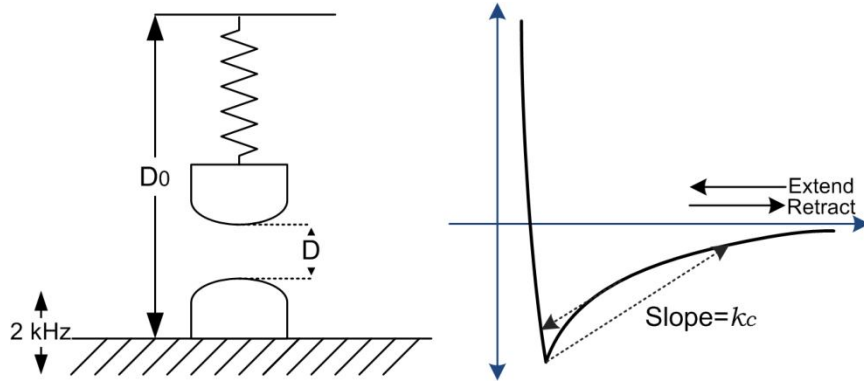


Figure 36 The schematic of the force curve; two bodies, one is connected to the non-stationary base by a spring. Second body (sample) on the z-piezo.

The force curve shown in Fig. 36 (b) has an attractive approach region near contact, a repulsive contact region when the tip indents the sample and an attractive separation region after the contact. When the tip approaches the sample, the tip may not follow the interaction force curve and find an equilibrium point by following the dashed line and the body #2 jumps into the contact. As a result, one may not be able to measure the real adhesion force between two bodies during the approach curve [15]. Similarly, as the bodies are separated from the contact, the probe cannot balance the interaction forces with the probe stiffness. Thus, it experiences the highest adhesive force point and then jumps out of the contact in the separation curve. When the probe jumps out of the contact, a cantilever will fall into an instable regime and follow the dashed line in Fig. 36. The slope of this line is equal to k_c in slow rate operations by AFM cantilevers, where damping is assumed to be zero. Stiffer probes will follow the interaction forces with less instability, so they are used for measuring the surface forces or imaging in TM AFM. Due to the high damping in FIRAT probes, FIRAT probes follow a damped version of the dashed line which shows a smaller slope than k_c . The experimental data on pentacene

is shown in Fig. 37; k_c is 18 N/m while the slope of the retraction is 15.74, slightly lower than k_c .

The adhesion force is 350 nN for silicon tip-pentacene contact in this measurement. The extraction curve has much lower slope than the retraction curve on pentacene that shows that probe instability does not occur in the extraction curve. As a result, the maximum attraction force for extraction curve is calculated as 140 nN.

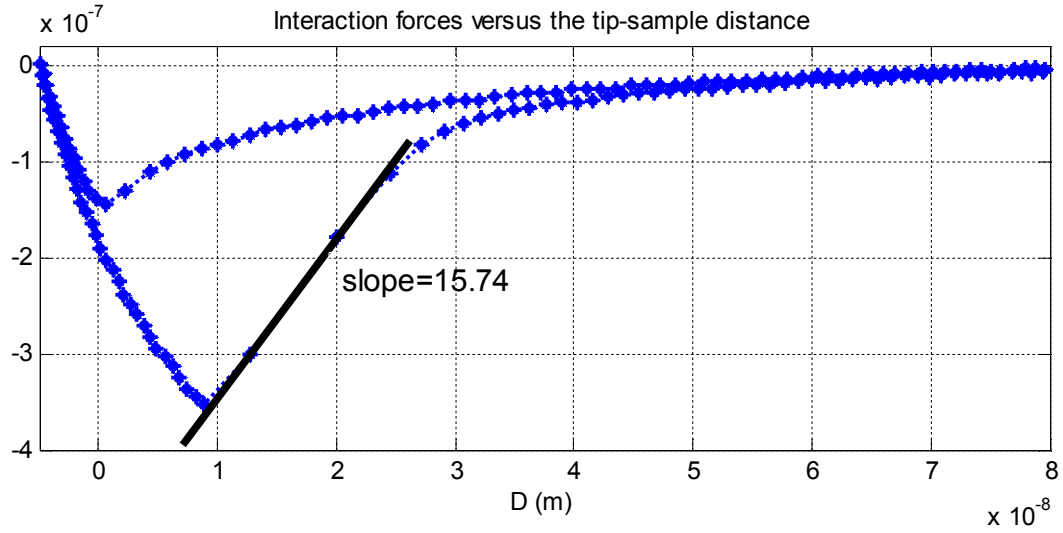


Figure 37 Interaction force versus tip-sample distance measured by FIRAT probe on pentacene.

A FIRAT set-up has to be used in ambient conditions since the damping of the squeezed film is required for the low quality factor. Electrostatic and van-der-Waals forces are the two main long range interaction forces in air. Water vapor in air causes a surface layer of condensed water and organic molecules around the contact; this capillary condensation makes the attractive forces stronger. In addition to these, FIRAT probe measures interaction forces between the tip and the surface by a dynamic operation so hydrodynamic and viscous forces may become effective [15, 16].

As discussed above, adhesion hysteresis arises with the interaction of the tip and the surface. It can be a result of probe instabilities, wetting angles, viscoelasticity and chemically inhomogeneous systems. However, one should not think of adhesion hysteresis as an imperfection of the system. Even after correcting the probe instabilities, using purely elastic homogenous materials in vacuum, one can observe adhesion hysteresis. Because of the chemical and mechanical changes in the tip and the sample after the contact, surface roughness and chemical heterogeneity will be induced and this will result in adhesion hysteresis.

Fig. 37 is the force-displacement curve obtained from the taps on the pentacene. Taps on the pentacene exhibit high adhesion and adhesion hysteresis without probe instability in the extraction curve. It means, the adhesion hysteresis is due to the losses – wetting, viscosity, lubricity, ext. – and changes that appear during the contact. While modeling the non-contact force regime, the patch-charge model with $1/(1+D/Z)^2$ dependence is used where Z is the distance between the charge to the tip end. This non-contact force region has the best fit for the materials imaged.

4.3.3.2 Contact Mechanics Models for AFM Tip-Sample Contact

As explained in previous sections, attractive forces exist and become effective on small enough scales. The force that keeps two surfaces together after contact is higher than the initial attractive forces and it is called adhesion force. The contact mechanics require more complicated models than Hertzian contact model since attractive forces are present for small scales.

The details on Hertzian contact theory are presented in section 2.1. When the contact forces are high and the surface forces are low, Hertzian theory is valid as in

UAFM experiments. On the other hand, one should use loading and unloading curves of the taps –or force curves– to characterize different mechanical properties and these curves have both low and high contact force regions. Accordingly, Hertzian theory cannot be applied to the taps. The relationship between the force and the deformation is explained by the following equation,

$$F = K\delta^{1.5}R^{0.5}, \quad (4.5)$$

where F is the force, δ is the deformation, and R is the tip radius. K is the reduced Young's modulus and is calculated as:

$$\frac{1}{K} = \frac{3}{4} \left[\left(\frac{1 - \nu_{tip}^2}{E_{tip}} \right) + \left(\frac{1 - \nu_{sample}^2}{E_{sample}} \right) \right], \quad (4.6)$$

in which ν is the Poisson ratio and E_{tip} and E_{sample} are the Young's modulus of the tip and the sample.

Another model that can be used is DMT (Derjaguin, Muller, Toporov) mechanics, which is usually used for rigid systems, low surface forces, and sharp tips [16]. This model is quite similar to Hertzian theory with an adhesion offset. As with Hertzian, DMT also does not suggest hysteresis in the loading and unloading curves. In DMT mechanics, the tip-sample contact starts with a negative adhesion force and then behaves as a Hertzian contact model:

$$F = K\delta^{1.5}R^{0.5} - 2\pi R\bar{w}, \quad (4.7)$$

where \bar{w} is the work of adhesion at contact. DMT is used to analyze the taps for FIRAT system and pulsed-force mode measurements. It is not necessarily the best fit for modeling tip-sample contact for AFM since it suggests a discontinuous slope for the start of the contact. However, it is preferred over other methods due to its simplicity.

BCP (Burnham, Colton, Pollock) was introduced after DMT to provide a better fit for the force curves. During the taps, the probe tip is attracted by the surface before the contact, and then a transition region appears between the initial contact and the high contact force. In BCP mechanics, it is assumed that sample surface will bulge out to the tip with the effects of attractive forces before the contact. Thus, deformation is negative at initial contact [16]. BCP mechanics is more complicated than DMT, so although it is more realistic to use BCP for modeling the taps, DMT is used while extracting data for material characterization. The equations for BCP mechanics are:

$$F = \frac{Ka^3}{R} - \sqrt{\frac{3\pi\bar{w}Ka^3}{2}} - \pi R\bar{w} \text{ and} \quad (4.8)$$

$$a = \sqrt{\delta R + \left(\frac{\pi^2 R^4 \bar{w}^2}{K^2} \right)^{1/3}}, \quad (4.9)$$

where a is the contact radius.

BCP mechanics do not have hysteresis, meaning that if the cantilever is infinitely stiff and attractive forces of the surface do not change during the contact, loading and unloading curves will follow the same pattern.

Another model that can be used for analyzing force-displacement data is the JKRS (Johnson, Kendall, Roberts, Sperling) mechanics. JKRS mechanics is suitable for high tip radius, high adhesion forces, and soft materials. One of the assumptions of the JKRS mechanics is that the attractive forces exist only when the tip and the sample are in contact and these forces are short-ranged [16]. As the tip is retracted from the sample, a connective neck is created and then broken as a rupture. This model has hysteresis but it

is not suitable for the FIRAT probes since it underestimates the attractive forces before the contact. The force and deformation equations are more complex than before:

$$F = \frac{Ka^3}{R} - \sqrt{6\pi wKa^3} \quad \text{and} \quad (4.10)$$

$$\delta = \frac{a^2}{R} - \frac{2}{3} \sqrt{\frac{6\pi wa}{K}}. \quad (4.11)$$

In 1992, Maugis improved a contact mechanics model that is more complex but more accurate and applicable on a wider range of tip-sample combinations. When using Maugis mechanics model, one does not need to use any assumptions about the material types or the geometry. Maugis mechanics employs a key parameter, λ , in the governing equations:

$$\lambda = \frac{2.06}{\varepsilon_0} \left(\frac{Rw^{-2}}{\pi K^2} \right)^{1/3} \quad (4.12)$$

In this equation, ε_0 , is the interatomic equilibrium distance. This key parameter, λ , helps to decide which mechanics model to apply [16]. If the λ of the system is much smaller than 1, DMT mechanics is applicable. If the λ is close to infinite, JKRS mechanics is a good fit for the system. BCP mechanics is used for moderate λ values.

For a typical FIRAT probe measurement, tip radius is 15-80 nm, w is 0.5-1, and K is 0.1-200 GPa. As a result, λ value is between 0.5 and 5. For these values, BCP and DMT can be used. According to the experimental data, samples like silicon, chromium fit well with DMT contact mechanics while BCP is a better fit for soft polymers.

To simulate the taps in Simulink, DMT and BCP contact mechanics are used. Both of these models do not include hysteresis while the actual taps have high adhesion hysteresis. As explained before, this hysteresis is not due to the probe mechanics. Since

DMT and BCP contact mechanics models do not include hysteresis, a variable surface energy block has to be added to the Simulink model (Fig. 33). By the help of this block, the surface energy that keeps the bodies together will increase during the contact and cause adhesion hysteresis as in the experiments.

To demonstrate the difference of the both models, taps on a sample with a 1 GPa Young's modulus are simulated by using BCP and DMT models. While DMT model suggests a sharp transition region, BCP model shows a smoother transition from non-contact to contact region, which is consistent with measurements on compliant materials. DMT is much easier to analyze and extract the stiffness data. Because of that, DMT has been used to analyze the taps both in FIRAT [52], torsional cantilevers [47], and pulsed-force mode [88] experiments.

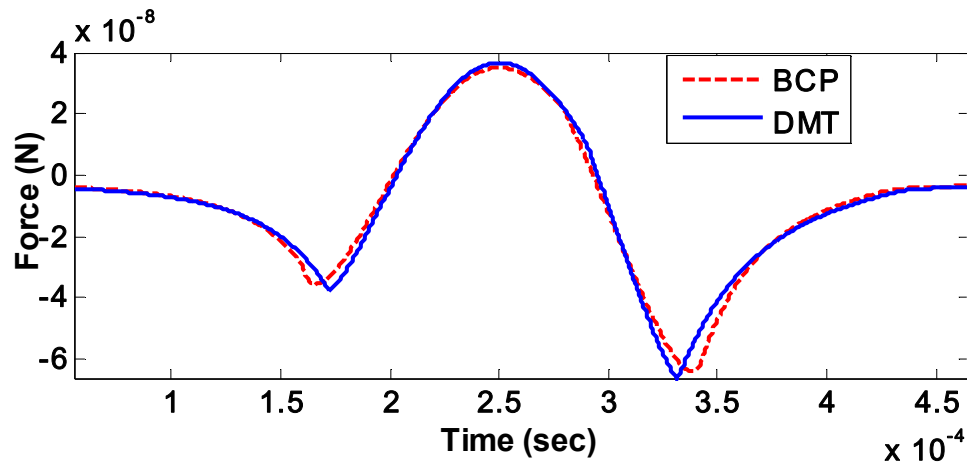


Figure 38 Tap simulated by using DMT and BCP mechanics.

4.3.4 Inverting the Taps for Material Characterization

The taps obtained by the FIRAT probe are examined, fits to different models are studied and possible taps are simulated by using Simulink. These studies give us the capability of inverting the taps for quantitative material characterization. When one can analyze the tap data quantitatively, the surface energy and Young's modulus on the sample can be mapped in nanoscale resolution.

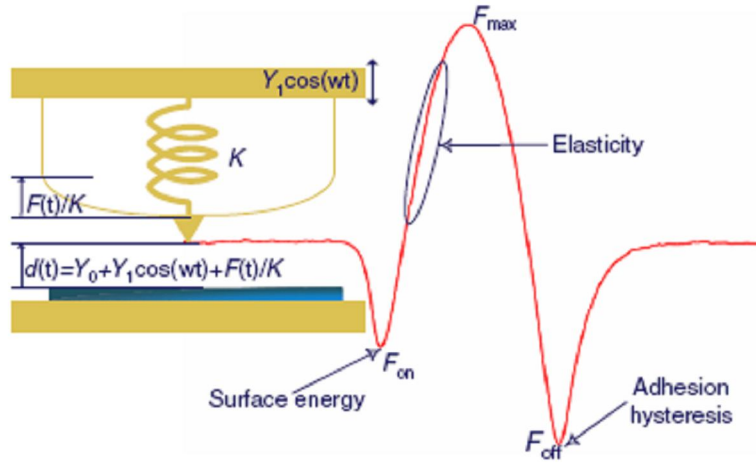


Figure 39 FIRAT probe interacting with the sample surface. Material properties can be extracted from the taps [52].

The expression needed for tip-sample distance, $d(t)$, is stated by Eq.4.4. DMT contact model uses $d(t)$ to calculate the interaction force, F ;

$$F(d) = K\sqrt{R}(-d)^{1.5} - 2\pi R\bar{w} \text{ for } d < 0, \quad (4.13)$$

where K is reduced Young's modulus calculated by Eq.4.6.

To obtain the reduced Young's modulus from the taps, one can assume a value for K , and calculate Y_0 (offset of the z-piezo movement signal) by:

$$Y_0 = Y_1 - \left[(F_{\max} - F_{on}) / (K\sqrt{R}) \right]^{2/3} - F_{\max} / k, \quad (4.14)$$

in which F_{max} is the maximum tap force and F_{on} is the force in initial contact. Then, the expected tap force can be simulated using the calculated value of Y_0 , assumed K , and measured F_{on} :

$$\Phi(t) = K\sqrt{R}[Y_0 + Y_1 \sin(2\pi f_0 t) + F(t)/k]^{3/2} + F_{on}. \quad (4.15)$$

The error, $\int |\Phi(t) - F(t)| / \int F(t)$, is computed for different values of K and the error is minimized for the correct K value. With this calculation, one can obtain K and Y_0 on the surfaces in nanoscale. In addition to this, it is possible to analyze taps generated by Simulink with the same method and address different error sources. These error sources can be the low cut-off frequency of the probe response, and ambiguities in the probe stiffness and the tip.

4.4 Sensitivity of the Elasticity Measurement by FIRAT Probe

4.4.1 Dependence of the Sensitivity on the Probe Dynamics

The FIRAT probes are highly damped low Q structures. The simulated and measured frequency responses of a FIRAT probe are shown in Fig. 29. The response is nearly flat until the cut-off frequency (Fig. 29) and it is possible to tailor the cut-off frequency by changing the gap (Fig. 40 (a)). To investigate the effects of the frequency response of the probe, the Simulink model shown in Fig. 33 is used. The cut-off frequencies between 10 kHz and 200 kHz are assigned as the probe response in the model, while K values of 1 and 5 GPa are used. Different taps with these configurations are generated without adding noise and then analyzed by using the analysis method. Since analysis method works with flat response assumption (losses and cut-off frequencies are ignored), calculated K values are not same as the assigned K values. The

error caused by frequency response is demonstrated in Fig. 40 (b) and according to these results; the cut-off frequency should be more than 40 kHz to provide error less than 5%.

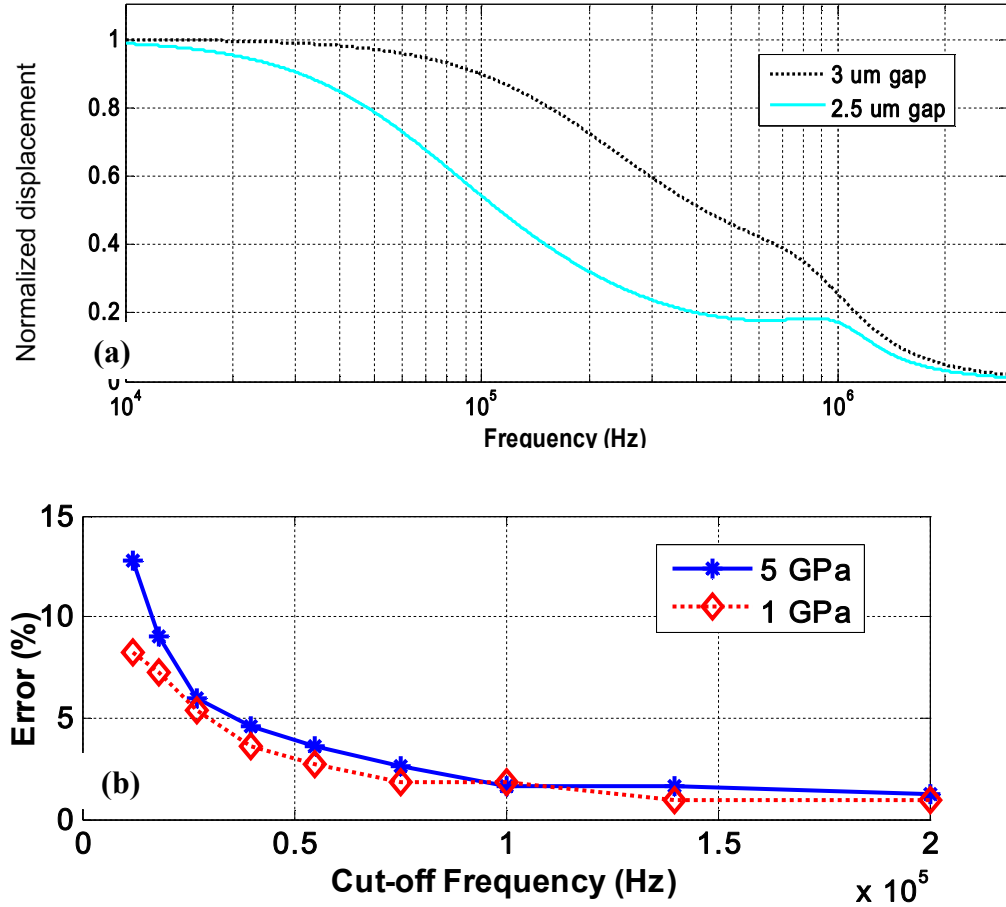


Figure 40 (a) Frequency response of the probe for different gaps. 3 μm gap provides 200 kHz cut-off frequency while 2.5 μm gap provides 70 kHz cut-off frequency. (b) Error in the Young's modulus calculation for different cut-off frequencies.

4.4.2 Effects of Experimental Uncertainties on the Elasticity Measurement

Sensitivity

Another error source is the ambiguity in the probe stiffness. Although AFM users usually know the range of the probe stiffness, calibration is required to find the exact probe stiffness. Even after the stiffness calibration, the calculated probe stiffness may have up to 20% error. This error margin will cause inaccuracy in K calculations. The

following figure shows how the error in probe stiffness affects the results for a 20 N/m probe. Users should be aware of this error margin while analyzing the results.

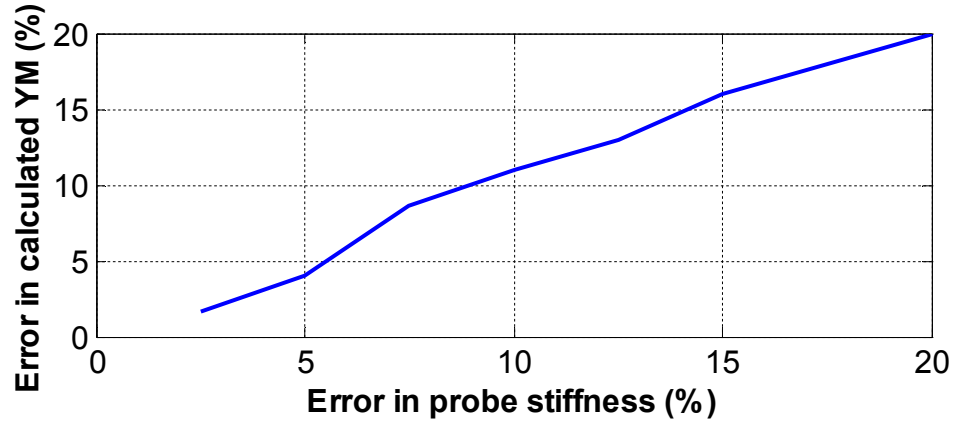


Figure 41 The error in measured Young's modulus due to the ambiguity in probe stiffness.

One of the problems of material characterization analysis by interaction force imaging by AFM is the validity assumption of DMT mechanics. DMT mechanics is the preferred analysis model since it is much easier to extract the mechanical properties. However, samples like soft polymers with high adhesion show contact characteristics similar to BCP mechanics as shown in Fig.38. To analyze the error due to the modeling, taps on a material with 500 MPa Young's modulus are simulated by using BCP mechanics. Then, the mechanical properties on this material are extracted from the taps by using DMT. The elasticity calculated by DMT is 280 MPa, which is much lower than the assigned value. It is important to know that when soft polymers are imaged by any probe with interaction force imaging capability, the data analysis with DMT method may provide K values lower than the real K value of the sample.

4.4.3 Effects of the Noise and Probe Stiffness on the Elasticity Measurement

Sensitivity

The FIRAT probe has diffraction gratings that create multiple orders and the intensity of these orders change with the displacement of the beam. Differential detection of these orders can decrease the noise to the shot noise level by eliminating the intensity noise. However, only the first diffracted order can be detected with the current FIRAT set-up and it results in high intensity noise, approximately 4 nNrms for a 100 kHz bandwidth. Material characterization sensitivity highly depends on the noise level.

To understand the effects of the noise and probe stiffness on the elasticity measurement sensitivity, the Simulink model shown in Fig. 33 is used. In that model, a white laser intensity noise is added to the probe deflection output resulting in 1.5 Årms displacement noise. The laser intensity noise does not depend on the probe stiffness, deflection, or dynamics. For a typical FIRAT probe, such a laser intensity noise results in 4 nNrms force noise. To analyze the elasticity measurement sensitivity, different probe stiffnesses with 100 kHz cut-off frequency are computed for each stiffness value. Then, the resulting taps are examined by using the algorithm outlined in the previous section. Computed K values with less than 12% error for each probe stiffness value is depicted in Fig. 42 and the lines represent the sensitive regime. According to this graph, there is no magical probe stiffness that can be used on a broad sample elasticity range. When the elasticity is too low, the tip indents into the sample and the probe barely deflects, causing the noise to dominate. On the other hand, for stiff materials the indentation into the sample becomes less than the noise level. Obviously, less noise on the system can provide wider error bars. In addition to this, one can use tips with a higher radius of

curvature (the simulated radius of curvature is 50 nm in this figure) to be able to analyze softer materials than the error bar limits. Basically, a higher tip radius will shift the bars down. This figure is not only a guideline for the FIRAT probes, but it can also be used for pulsed-force mode and torsional cantilevers that utilize interaction forces to calculate the elasticity.

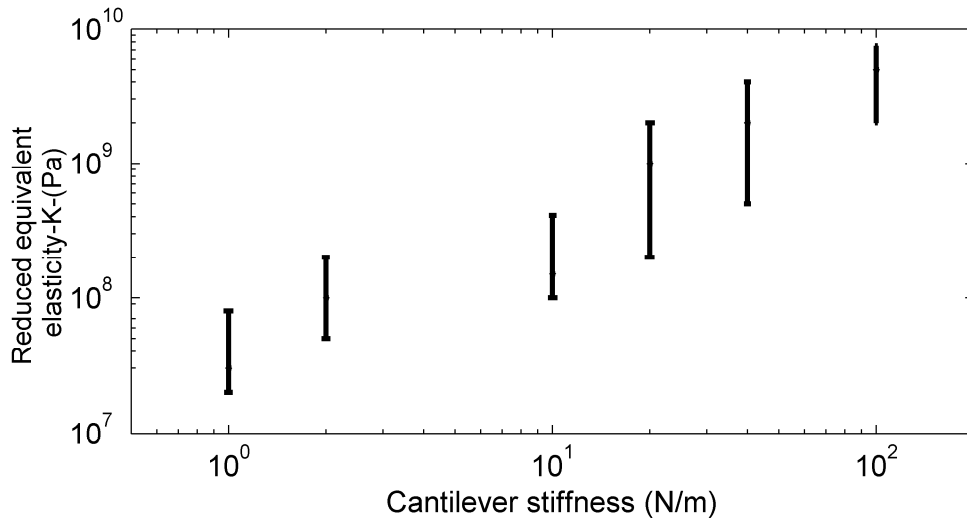


Figure 42 The elasticity values that can be measured accurately for different probe stiffnesses.

To enhance the sensitivity, one can apply averaging on the data. The force noise after averaging is shown in Fig. 43. The reduced noise levels can help to provide elasticity data with more accuracy but high averaging requires slow scan rate. It has been shown in Degertekin group that making an AFM head for differential detection will solve this problem without averaging and provide fast material characterization capability [96, 97]. The ideal AFM head has a laser source, split photodiodes and a circuitry for differential detection. A similar structure is built for imaging biomolecular forces by micromachined membrane based active probes [97].

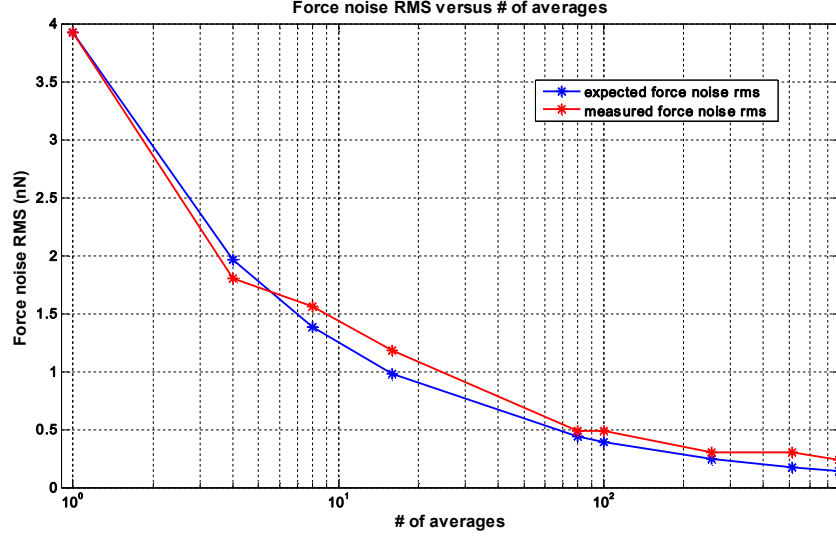


Figure 43 Force noise RMS versus number of averages.

4.5 Inversion of the Taps for Layered Media Characterization

TRIF mode of the FIRAT probe can provide mechanical properties on the surfaces by measuring the interaction force curves. Until now, bulk materials are used in the tap simulations. However, the sample may contain subsurface layers and structures. The reduced Young's modulus is constant on a half-space substrate while it changes as a function of the contact force when the sample has subsurface layers. This difference causes variations in the taps.

Although the basic Simulink model for TRIF mode is constructed for constant K , it is possible to compute $K(d)$ for the layered material. $K(d)$ means K values are dependent on the indentation of the sample and the methods to calculate $K(d)$ values are explained in Chapter 2.

For a soft 4 nm polymer layer of 100 MPa Young's modulus on 30 GPa substrate, the effective Young's modulus increases from 100 MPa to 5 GPa with the indentation. In the following figure, taps are generated for the substrate with and without the soft top

layer. According to the simulations, one can easily observe the parts of the sample with and without soft top layer.

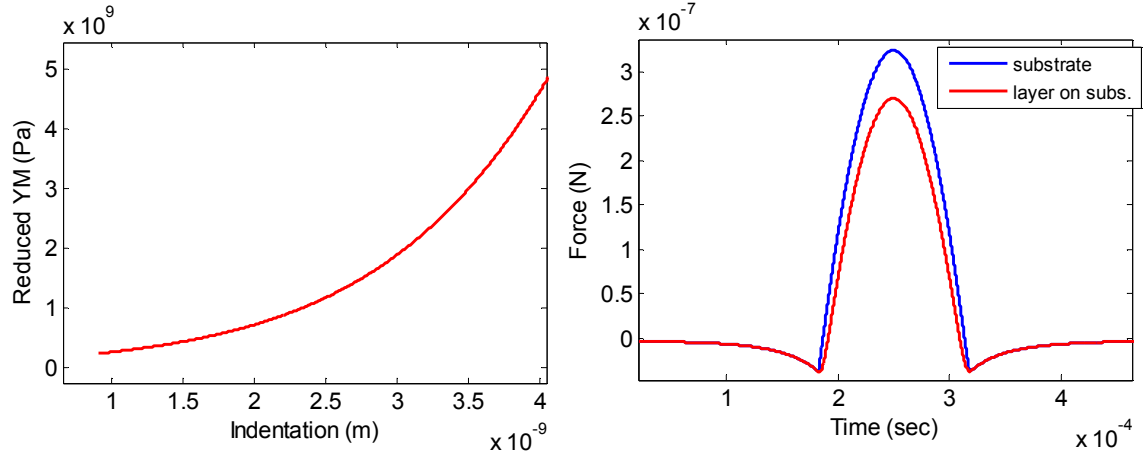


Figure 44 (a) The effective elasticity on the surface changes with the indentation. (b) The taps show differences for bulk material and the layered material.

4.5.1 Mechanical Properties Imaging on the Layered media

The current method for calculating K simultaneously solves the two unknowns; Young's modulus, K , and offset, Y_0 . To do so, the whole repulsive force region is used. However, the existence of the subsurface structures causes modifications in F_{max} and the slope. As a result, the previously introduced tap inversion method cannot be applied for the layered media.

To resolve this issue, a different tap inversion algorithm is introduced for layered media. In this method the initial contact of the tip with the surface (F_{on} location Fig. 39) is used to calculate Y_0 .

$$F_{on} = F(t_0) = K \sqrt{R} |Y_0 + Y_1 \cos(2\pi f_0 t_0) + F(t_0)/k| + F_{on} \quad (4.16)$$

and

$$Y_0 = -Y_1 \cos(2\pi f_0 t_0) - F_{on} / k. \quad (4.17)$$

After obtaining the offset value, one can analyze an individual tap by computing K versus indentation. The subsurface composition can be obtained by using this data. The Simulink generated tap on the layered material is examined by this inversion algorithm and the results are plotted with the assigned Young's modulus values.

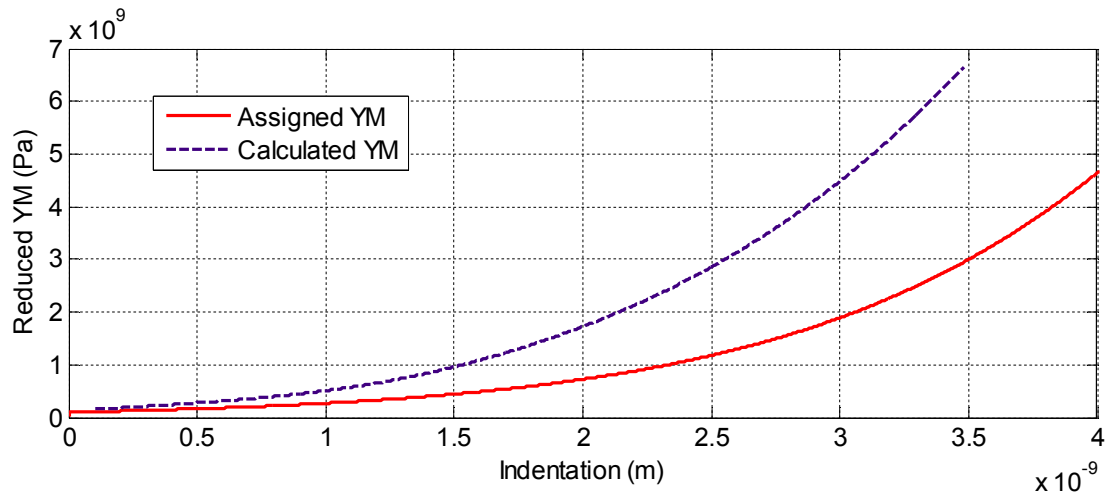


Figure 45 The taps simulated for layered material is then analyzed and the calculated values and the real values are plotted.

As seen in Fig.45, the calculated K values are higher than the assigned K values. Since the probe has loss due to the squeezed film effect, the probe responds to the interaction forces with a delay. This delay causes error in t_0 and consequently in the Y_0 calculations. The probe simulated in this example has a 200 kHz cut-off frequency and probes with lower cut-off are not suitable for characterizing the layered media with this algorithm.

The method proposed for layered media can also be used for the half-space materials. Nevertheless, since this method relies on one force point instead of the whole curve, the calculated K results have higher error rates than the previous method.

4.6 Chapter Summary

Although intermittent contact mode is the preferred mode of operation for compliant samples, it is challenging to obtain interaction forces between AFM tip and surface while imaging because of the cantilever dynamics. Various methods like imaging the phase or harmonics have been introduced as well as modified cantilevers. In 2005, a membrane based active probe with interferometric detection scheme was developed by Degertekin group and elasticity imaging capability of this probe is demonstrated by applying an inversion algorithm. In this research, the effects of probe dimensions on the probe dynamics are examined and a Simulink model of intermittent contact mode imaging with the probe dynamics and different contact mechanics models is implemented. The interaction forces simulated by this model is investigated by the inversion algorithm and the effects of the different parameters, such as cut-off frequency, probe stiffness, and assumed contact mechanics model, on the measured elasticity are observed. In addition, the previously demonstrated inversion algorithm is extended to substrates with subsurface structures. The results and models presented in this chapter guides the future AFM probe designs and determines the error rates on the experimental analysis.

CHAPTER 5

ACTIVE TIP CONTROL OPERATION OF FIRAT PROBES

The instability of the taps and the high repulsive forces have been two contradicting problems in the intermittent contact mode. The instability [98] is caused by attractive forces of the surface; the probe tip jumps into the contact due to the attractive forces while it is approaching the surface and can't leave the contact until it jumps out of the contact. The instability increases with higher attractive forces so it is observed clearly while examining the taps of the FIRAT probe. To overcome this instability, one may apply higher oscillation amplitude, or use stiffer AFM probes [53] which may cause tip wear or sample deformation due to higher contact forces. In addition to this, a stiffer probe may reduce the force sensitivity. Softer AFM probes provide better material characterization sensitivity on the compliant samples [91], however these probes are more susceptible to the instability. An ideal AFM probe for the soft materials should act as a soft probe while the tip is in contact with the sample to limit repulsive forces, and as a stiff probe against attractive forces for stable operation. Since regular AFM cantilevers are passive force sensors, one needs to compromise force sensitivity for stability and sample deformation. This trade off can be overcome if one can change the probe characteristics during individual tapping events, requiring an active and fast AFM probe.

5.1 The Working Mechanism of FIRAT Probes with Active Control

The FIRAT probe is an active AFM probe which is “active” due to its integrated electrostatic actuator. The “active” nature of the FIRAT probe can be used to control the interaction forces during a single tap and removing the trade off in TM imaging. This is

achieved by using active tip control (ATC) circuitry which is activated to retract the tip while it is still in contact with the sample surface and consequently reduce the tip-sample interaction force only when the interaction force exceeds a certain threshold during a single tapping event. The ATC circuit is switched off when the tip is not in contact. Using this capability, one can control the repulsive forces on the tip as well as indentation into the soft sample regions while avoiding instability due to attractive forces during TM imaging. Tip wear and high indentation into the soft samples can be decreased, more accurate topography imaging becomes possible and attractive forces do not affect the repulsive forces.

The FIRAT probe can measure TRIF signals while tapping on the sample surface and different phases of these TRIF signals can be used to interpret nanomechanical material properties of that sample [52]. A typical TRIF signal in absence of ATC is shown in Fig. 46 (a). During phase I and phase II, the tip is attracted by the sample as it approaches the surface, the contact occurs and the repulsive force causes deflection of the FIRAT probe. As the FIRAT probe is brought closer to the surface, the repulsive force and the indentation to the sample will increase (phase III). The aim of ATC is to reduce the repulsive force during phase III by applying the FIRAT control signal (Fig. 46 (b)) to retract the tip and limit the indentation.

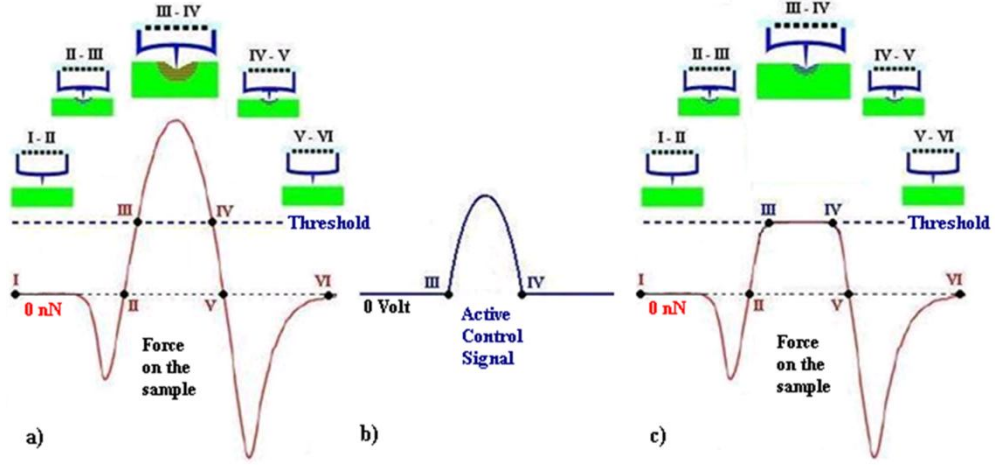


Figure 46 The shape of the FIRAT probe and the indentation on the sample during different phases of intermittent contact mode. Phase III is depicted with and without active tip control. When ATC is employed in phase III, less indentation of the sample occurs.

As the tip scans the surface and taps, both the tip and the sample get deformed. Especially for the soft samples, sample deformation may affect the topography measurement. Depending on the material and the applied force, this deformation can be significant, more than a few nanometers, and may cause the loss of crucial information. According to the Hertzian contact theory, the deformation due to contact is a function of the equivalent Young's modulus of the materials in contact, E^* , the radius of curvature of the tip, R , and the applied contact force, F_c . The maximum deformation of the contact, h , is formulized as following:

$$h = \sqrt[3]{\frac{9F_c^2}{16E^{*2}R}}. \quad (5.1)$$

Decreasing F_c is a trivial solution for better topography measurement. F_c can be reduced by changing the setpoint while it may result in insufficient contact time and consequently cause instable operation. On the other hand, ATC can alter the maximum of the contact force without decreasing the duration of the contact as depicted in Fig. 45.

During the phase III of Fig. 46, probe tip is retracted by ATC signal for avoiding the higher indentation into the surface. The indentation decreases because F_c is the difference of the total mechanical force resulted from the probe deflection, F_{probe} , and the electrostatic force applied to the probe to retract the tip, F_e ;

$$F_c = F_{probe} - F_e. \quad (5.2)$$

When ATC is not employed, F_c is equal to F_{probe} since the deflection in the tip is only caused by the tip-sample interaction. On the other hand, some deformation is needed for the mechanical property measurement. By controlling F_e , one can adjust the sample deformation to a level so that mechanical property information can still be obtained with minimum effect on topography measurement [99].

5.2 Experimental Set-up for the Active Tip Control

The experimental set-up used to implement this scheme is shown in Fig. 47. A multimode AFM is modified to obtain time-resolved interaction forces (TRIF) during the topography imaging in this set-up. Note that in this setup a peak detector is used instead of an RMS detector in the loop controlling the z-piezo, since individual tap signals can be captured by the FIRAT probe. With this configuration, the maximum repulsive force in each tap is kept constant while attractive forces change during scan. Consequently, attractive force differences on the surface will not cause unruly contact forces, which may lead to tip wear or severe indentation of the sample. For the ATC implementation, the probe deflection is compared with a threshold value by the precision rectifier (also known as super-diode) and an output signal is generated and amplified for only the part of the signal over the threshold value. This output signal is added to the bias voltage and applied to the probe. Since the FIRAT probe has a high cut-off frequency, the tip responds to the

fast actuation signal and moves up to reduce the force applied to the surface. To obtain the real interaction force when ATC is in use, the calibrated tip deflection caused by the ATC is subtracted from the PD signal. Calibration of ATC is achieved by applying a sine wave to the electrostatic actuator and monitoring the resulting PD output.

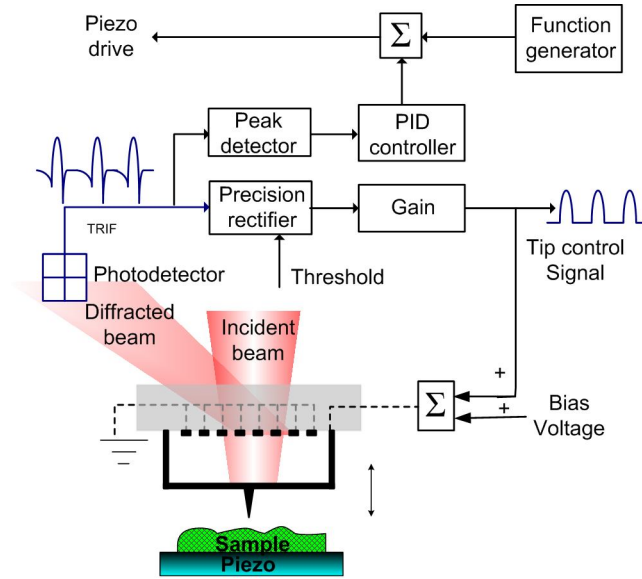


Figure 47 Experimental set-up integrating FIRAT probe with AFM system and ATC circuitry. Peak detection of PD signal is used for controlling Z-piezo. ATC signal is generated from PD signal and is used to retract the FIRAT probe when the contact force exceeds a threshold value.

5.3 Results

Typical tap signals observed during the imaging experiments with and without ATC are shown in Fig. 48. The particular signals are obtained on a 20% mass fraction of Polyisoprene (PI) and 80% mass fraction of Polystyrene (PS) polymer mixture [100] residing on a silicon (100) substrate. The measured TRIF signal without ATC is shown in Fig. 48 (a). The maximum of the F_c is 740 nN and this force is applied to both the polymer surface and the tip. The tip is retracted by the signal shown in Fig. 48 (b) with a peak of 23 nm. The signal is applied to the tip and it changes the tap into the signal shown in Fig. 48 (c), the photodiode output is represented as dashed line while the real

force signal is shown as the solid line. Although the repulsive force is decreased by 400 nN in Fig. 48 (c), the contact time is same. As a result, less repulsive force and consequently less indentation without decreasing the contact time and causing instability is provided [99].

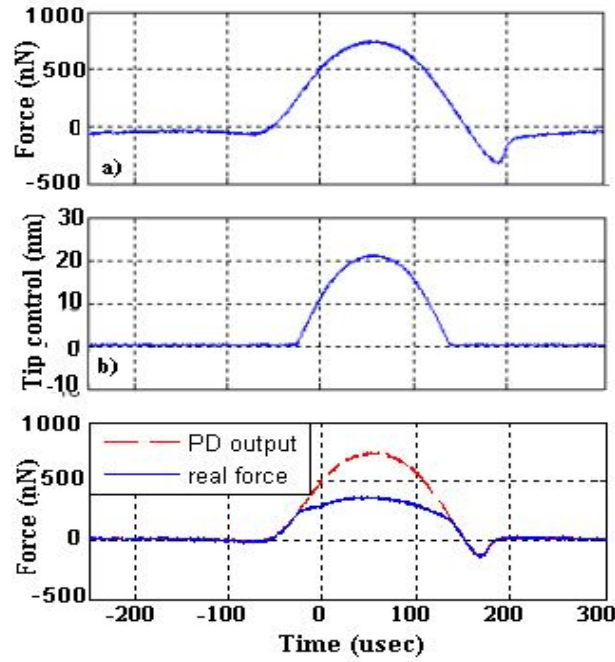


Figure 48 (a) Individual tap signal without the active tip control. (b) Active tip control signal to the FIRAT probe. (c) Force on the FIRAT probe and real interaction force signal.

To demonstrate the advantage of the reduced repulsive force for accurate topography imaging of soft samples, a PS ($E=2-5$ GPa)/PI ($E=1-3$ MPa) [101] polymer mixture on a silicon ($E=150$ GPa) substrate is used as a test sample and 250 nm thick patterned chromium ($E=279$ GPa) layers on silicon [50] as a control sample. The force curves by an AFM cantilever on different points of the samples are shown in Fig. 49 (b) and (d). According to these measurements, in the polymer sample (Fig. 49 (a)) the low topography indicates higher force curve slope and consequently stiffer surface while the rest of the surface is coated with softer thick polymer. The force curves on the control

sample (Fig. 49 (d)) have the same slope, showing that the stiffness of these materials is higher compared to the polymer mixture.

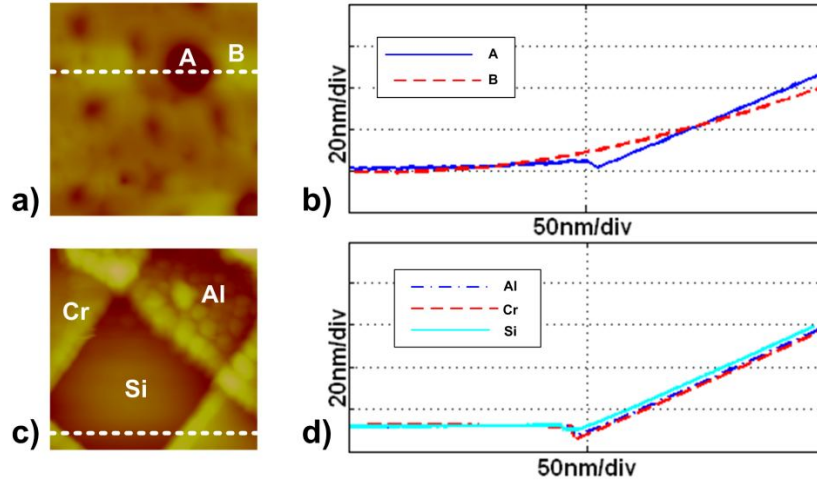


Figure 49(a) Topography of the polymer sample. Point A and B indicates lower and higher regions of the sample. (b) Force curves on point A and B. (c) Topography of the grating sample. (d) Force curves of different materials on the grating sample.

The blue straight line in Fig. 50 (a) indicates the topography of the polymer sample on the white line of Fig. 49 (a). To see the effect of the force levels on topography, first the same line on the sample is scanned with peak force of 400 nN. Then, the peak force is decreased to 150 nN by employing ATC. The topography difference between regular and active tip controlled TRIF mode is shown as the red dashed line in Fig. 50 (a). Note that with the exception of spikes around the edges of the topography, there is significant difference ($\sim 1\text{nm}$) over the flat sections of the polymer layer whereas negligible difference is observed on the lower regions ($\sim 0.3\text{nm}$). As a control experiment to demonstrate that sample indentation causes topography difference, the patterned chromium sample is scanned with the same peak force levels. The results are shown in Fig. 50 (b). Except for the spikes in the transitional regions, the smooth silicon and

chromium surfaces have negligible (0.1 nm) topography difference. In contrast to the soft sample, the reduced force by ATC on the stiff sample does not change the indentation and consequently the measured topography remains unchanged.

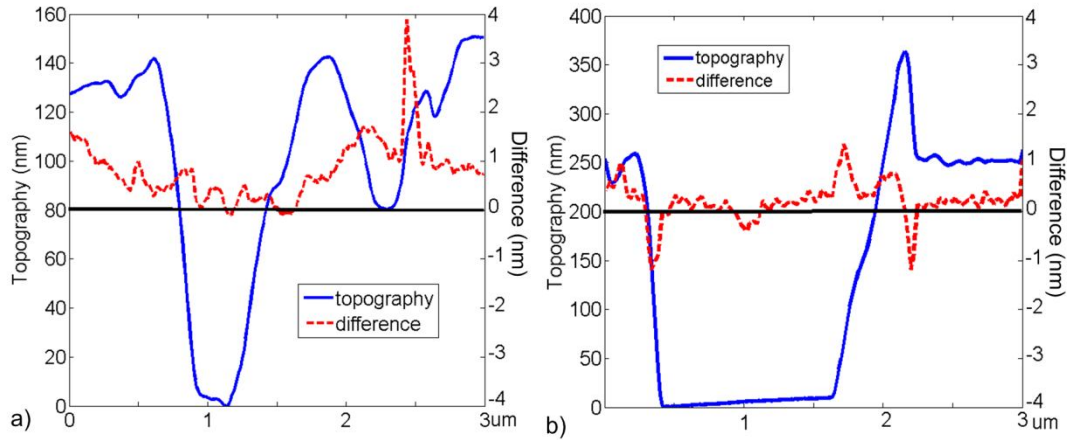


Figure 50 Topography and the topography difference observed by employing ATC on a (a) PS/PI polymer mixture and (b) patterned chromium on silicon [99].

5.4 The Applied Forces to the Surface during ATC

While operating TRIF mode of FIRAT probe with ATC capability, the user observes the deflection of the FIRAT probe through the PD output. Some of this deflection is the result of the tip-sample interaction force while the rest is the electrostatic force. Although a calibration procedure is applied before the operation to obtain applied voltage-deflection ratio, more simulations are necessary to understand the applied force to the sample. The results shown in Fig. 48 (c), are not accurate since the calibrated ATC signal is directly subtracted from the measured deflection. However, the ATC signal calibration requires including a scaling factor for the electrostatic forces and the delay.

One of the most important parameters for ATC signal analysis is the probe response. Because, subtracting the ATC signal from the probe deflection assumes a flat frequency response while FIRAT probes can have cut-off frequencies between 40 kHz

and 300 kHz. To analyze the effects of the probe dynamics, the previously generated Simulink model of FIRAT probe operation is modified. The modified scheme is shown in Fig. 51.

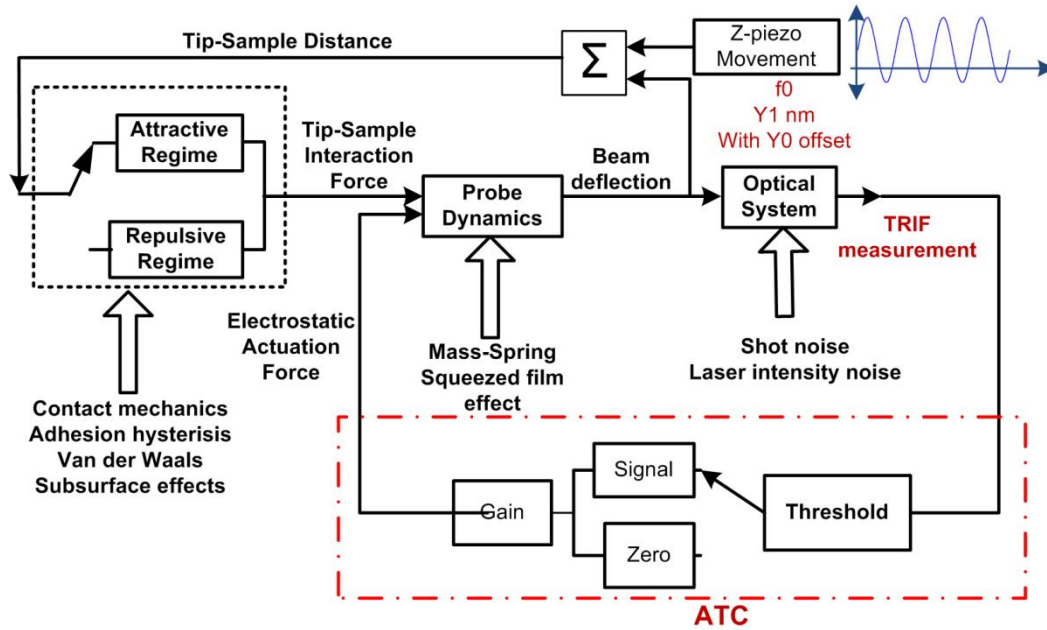


Figure 51 ATC block is added to the Simulink model shown in Fig. 33.

In this model, a block for ATC operation is added. This block works similar to the current experimental set-up. When the tip deflection is detected, it is compared with a threshold and then an ATC signal is generated from the high contact force regions. This force is sent back to the probe and the probe is retracted to avoid high contact force. The probe deflection and the interaction forces can be simulated by this model. Fig. 52 shows the interaction forces simulated for a FIRAT probe with 80 and 300 kHz cut-off frequencies. If the probe was ideal, the interaction forces curve would have a flat top. Since the response is not ideal, some delay is added to the ATC signal and the reduced cut-off frequency causes distortion in the interaction forces. The ATC signal duration is shorter than a normal TRIF signal, so it requires higher bandwidth. As a result, the

interaction forces are not as low as ATC intended and they become higher as the cut-off frequency of the probe decreases.

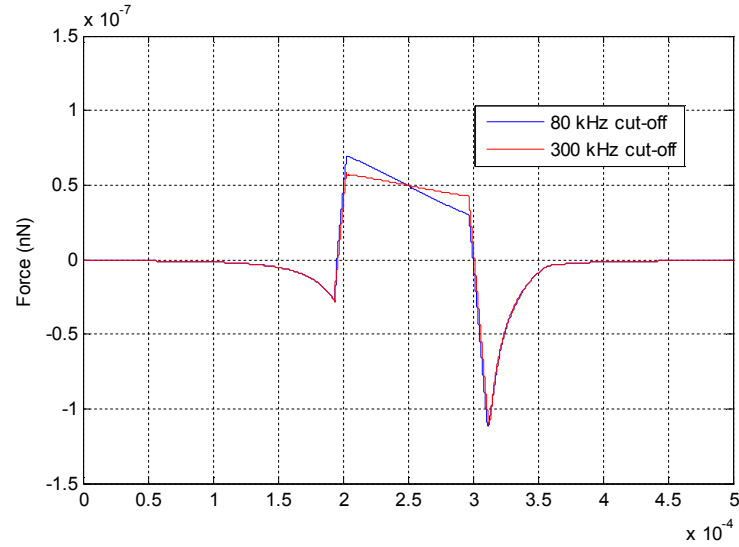


Figure 52 The interaction forces after applying ATC.

When the tip of the probe makes contact with the surface, the force is applied as a point load. On the other hand, the electrostatic force is applied all over the FIRAT probe beam (Fig. 53). The deflection is detected by the interferometric detection, in which a laser spot of 20 μm radius is illuminated on the beam. In fact, the detection measures the average displacement of the beam under the laser spot, not the displacement of the tip. However, this does not create a problem in normal TRIF mode operation since the electrostatic forces are not used with interaction forces.

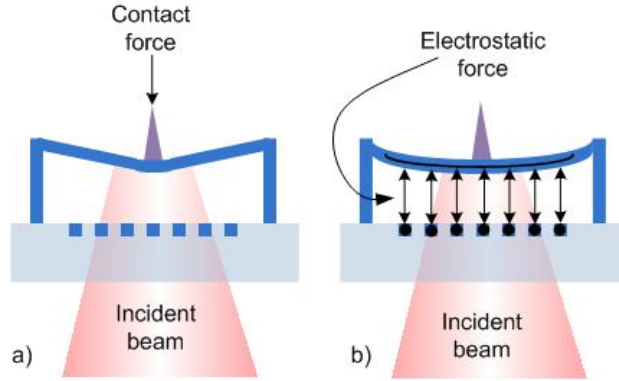


Figure 53 (a) The deflection of the beam when contact force is applied. The area around the tip deflects more than the rest of the beam and the laser beam averages out the displacement. (b) The deflection of the beam when ATC is used. Beam deflects with a smoother profile.

When ATC is employed, a scaling factor, that represents the ratio of the tip deflection to the average deflection, is required to adjust the electrostatic deflection in terms of the tip deflection. To examine the geometry affects on the scaling factor, a 3-D FEA model of the doubly-supported FIRAT probe beam is constructed. Then the average displacement is calculated for different laser spot sizes and compared with the tip deflection. The scaling factor is closest to unity (meaning no need for scaling) when the beam is large (as 100x100 μm beams) and spot size is small, as expected. The scaling factor may become as low as 0.85 for small beams and large spot sizes. The scaling factor can be added to the Simulink model (Fig. 51) as the gain parameter in the ATC block.

5.5 Chapter Summary

A method is developed to actively control the interaction forces during individual tapping events of intermittent contact mode [99]. This is achieved by ATC circuitry integrated with an AFM system that retracts the FIRAT probe tip during each tap cycle when the force exceeds a user-specified threshold. This method enables stable imaging with reduced repulsive forces, preserves a desired section of the force curve for nanoscale

material characterization, and provides more accurate topography data especially on soft samples. This imaging method is particularly useful for imaging soft, heterogeneous samples regardless of the substrate material. By accurately controlling the repulsive forces, one can investigate the effect of indentation on the force curve during dynamic AFM imaging, helping accurate nanomechanical characterization of layered surfaces.

CHAPTER 6

SIMULTANEOUS TIME-RESOLVED INTERACTION FORCE AND ULTRASONIC AFM MEASUREMENT FOR BROAD RANGE OF MATERIALS: ULTRASONIC TRIF MODE

The AFM mode selection depends on both the sample properties and the desired parameters to measure. While imaging compliant samples, intermittent contact AFM is used to minimize sample damage. Topography, elasticity, adhesion, and adhesion hysteresis can be measured concurrently on a surface by monitoring transient tip-sample interaction forces during intermittent contact AFM [47, 49, 50, 86]. In this mode, the probe should be soft enough to avoid high indentation, while it should also be stiff enough for a stable operation. Even though these requirements can be satisfied by optimizing the probe stiffness [53] or applying active control [99], the probe stiffness has to be matched with contact stiffness to maintain sensitive mechanical characterization. The elasticity range that can be imaged by a probe due to the stiffness limitation is shown in Fig. 41. On stiff samples, contact stiffness can easily reach few kN/m even at low contact forces [23]. High probe stiffness decreases the force sensitivity and also if the material type varies on the same substrate, the sensitivity of the probe will be different all over the sample. To overcome the difficulty of fabricating and employing very stiff probes, mechanical property measurements on a stiff surface is usually performed in contact mode AFM with ultrasonic actuation [25, 26, 63, 64, 68, 69, 74, 102]. In the ultrasonic AFM (UAFM), the effective probe stiffness is increased by using higher order vibration modes of the probe [25].

One uses different imaging modes and probes [89] when analyzing materials of different stiffness since intermittent contact probes are not sensitive on the stiff materials

and contact mode UAFM may be destructive especially on soft samples. Consequently, composite samples, like polymer mixtures, with stiff and compliant regions especially pose a challenging problem for sensitive, quantitative and nondestructive imaging of mechanical properties. One approach to address this challenge is to combine several imaging modes. For example, pulsed-force imaging has been combined with UAFM for this purpose [103]. However, the quantitative nature of the measurements obtained from each mode, especially UAFM, has not been retained. In this study, a method that combines time-resolved interaction force (TRIF) imaging with UAFM is described and an analysis of the results is presented to take full advantage of both modes. The method is gentler on the sample as compared to regular UAFM because of intermittent contact and lack of lateral forces, provides quantitative UAFM data over a range of forces during a single tap, and maintains high sensitivity to both soft and stiff features. A FIRAT probe based system is used to demonstrate the method. The broad bandwidth of the FIRAT probe is useful for TRIF imaging capability, while its integrated ultrasonic actuator simplifies UAFM operation at MHz frequencies [50, 52].

When the dynamic stiffening at ultrasonic frequencies is employed during the interaction force imaging, it is possible to characterize materials with high sensitivity. Such an application increases the range of the samples that can be characterized by an AFM probe, nanocomposites can be analyzed with higher accuracy, and the elasticity of the samples can be obtained for multiple force points.

6.1 Experimental Set-up and the Results

The experimental set-up for the combined TRIF and UAFM mode imaging is shown in Figure 54. For TRIF mode imaging, the z-piezo is actuated at 2 kHz to generate taps

on the sample surface and the controller keeps the RMS value of the tap signal constant while the interaction force signal at the photodetector (PD) is digitized. Simultaneously with TRIF imaging, the FIRAT probe tip is vibrated using the integrated electrostatic actuator at an ultrasonic frequency to perform UAFM imaging. As a result, the PD output not only has the signal related to the TRIF, but also the high frequency UAFM signal which is much smaller in amplitude as compared to the TRIF signal. The UAFM component of the PD output is analyzed by a lock-in amplifier (LIA) in a time-resolved manner and its phase and amplitude are recorded for further analysis [104].

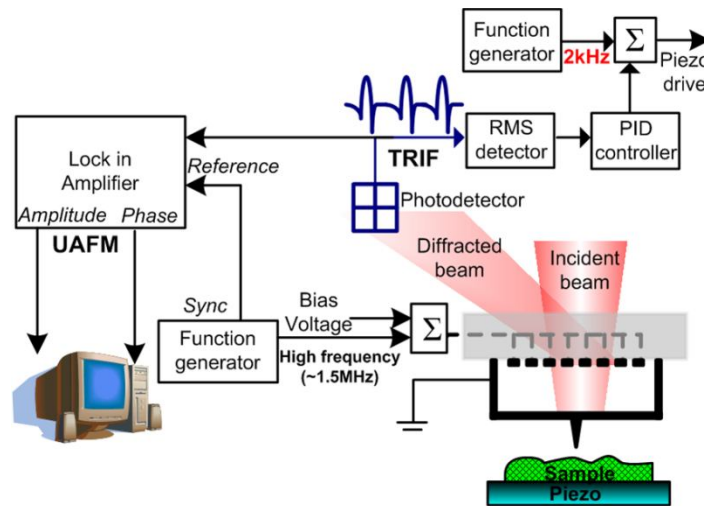


Figure 54 The experimental set-up for ultrasonic TRIF mode.

Quantitative analysis of elasticity and adhesion based on the TRIF signal has been described in the fourth chapter [52]. That analysis relies on the static spring constant of the probe and is accurate on samples with less than 2 GPa elasticity for a 25 N/m FIRAT probe. To quantify the UAFM signal, one considers how the response of the probe changes with tip-sample contact, specifically how the higher order mode resonances change with contact stiffness, k^* . The equation for contact stiffness calculation is also explained and shown in second chapter. Contact stiffness provides elasticity information

through the Eq. 6.1 which relates k^* to the contact force, F , tip radius, R , and reduced elastic properties of the tip and the sample, E^* ;

$$k^* = \sqrt[3]{6FRE^{*2}} \quad (6.1)$$

During TRIF imaging, the tip goes through non-contact and contact regions in every tap (Fig. 55 (a)). In the non-contact region, the frequency response of the FIRAT probe is close to the free probe response (Fig. 55 (b)). When the probe contacts the surface, the tip-sample contact stiffness effectively acts as a spring attached to the probe and causes changes in the response of the probe. The response of the same probe in contact with the surface at a fixed force of 224 nN is also shown in Fig. 55 (b). The particular FIRAT probe has resonance modes around 800kHz and 1.2 MHz with low quality factors, which generates oscillation free tap signals suitable for TRIF mode imaging. When the probe contacts the surface with 224 nN force, the resonance frequency at 1.2 MHz moves to 1.4 MHz, and its vibration amplitude is amplified.

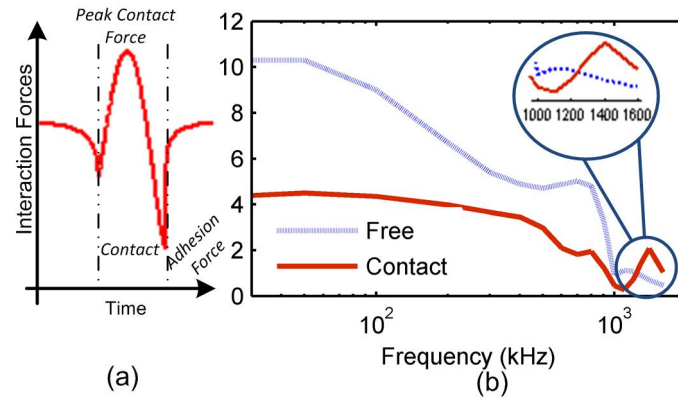


Figure 55 Frequency response of free FIRAT probe and probe in contact. Higher resonance modes are amplified with the contact [104].

The contact force, hence the contact stiffness is not constant during a tap (Fig. 55) and consequently the frequency response of the probe is altered in the course of the

contact region [23]. Figure 56 shows the TRIF signal and the UAFM signal amplitude when the FIRAT probe is driven by a 1.25 MHz signal (Fig. 54). The UAFM signal amplitude decreases with the initial contact and then increases as the resonance frequency is first smaller, then larger than the measurement frequency. It is evident from this behavior that dynamic changes in contact resonance can be tracked in real-time with the FIRAT probe. However, this interesting result is difficult to quantify for elasticity measurements. When the same probe is actuated at 1.4 MHz, higher tip-sample contact force creates a monotonic increase in the magnitude of the vibration (Fig. 57), which provides a single valued, quantitative calibration curve. Therefore, the UAFM frequency is chosen at a frequency where this type of behavior is observed.

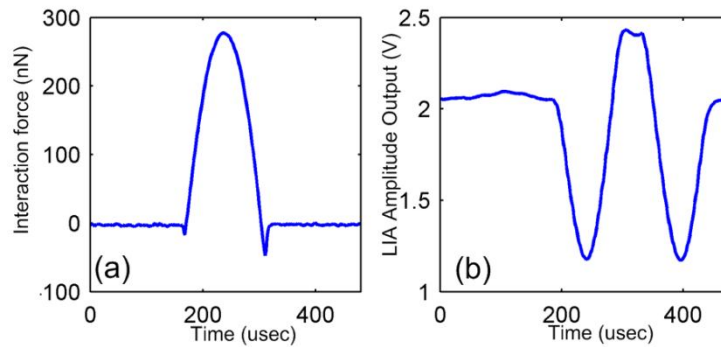


Figure 56 Interaction forces during the tap and the vibration amplitude for 1.25 MHz. By the initial contact amplitude decreases but then increase in the stiffness boosts the amplitude.

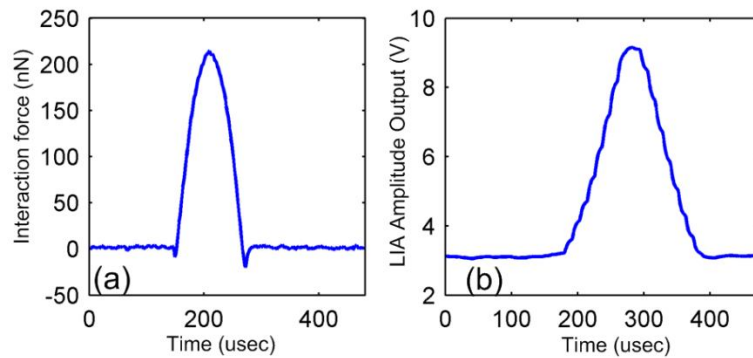


Figure 57 Interaction forces during the tap and the vibration amplitude for 1.4 MHz.

Fig. 58 shows a calibration curve where the lock-in amplifier output amplitude is plotted for different contact stiffness values obtained by increasing the contact force (Eq. 6.1). The probe used in this calibration procedure is actuated by a small signal at 2.25 MHz. The calibration curve is generated as follows: First, the tip is placed on a clean silicon surface and the TRIF measurements are performed at 2 kHz. Then, different set-points are assigned to the controller which resulted in taps with peak-forces ranging from 100nN to 800 nN. The interaction forces and UAFM signals are recorded for each peak contact force. With other parameters in Eq. 1 known, one can match the increase in the amplitude of the lock-in amplifier with the contact stiffness (Fig 58). This particular calibration curve shows that if the contact stiffness reaches 500 N/m, the amplitude change reaches 0.4 V. For contact stiffness values higher than 600 N/m, the amplitude change starts to saturate.

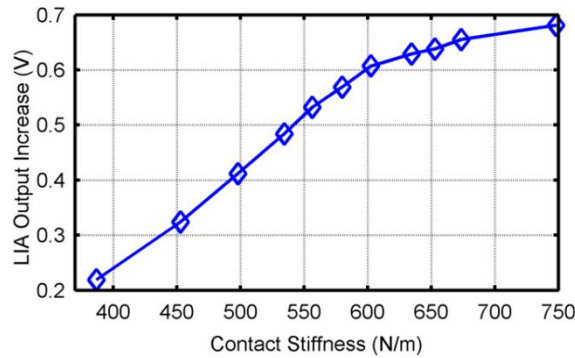


Figure 58 The vibration amplitude change created by contact stiffness at 1.45 MHz.

Combined TRIF and UFAM imaging is performed on a sample composed of silicon, aluminum, and chromium to compare TRIF and UAFM based elasticity measurement results on stiff samples. During imaging, the TRIF mode provides topography, adhesion

and elasticity data (Fig. 59 a-c). The UAFM mode elasticity image (Fig. 59 d) is obtained using the calibration curve in Fig. 58, and converted into reduced Young's modulus by Eq. 1. Although both methods provide three distinct regions of different stiffness, the standard deviation of the UAFM image is lower, providing an improved measurement of reduced Young's modulus as compared to the TRIF mode (Fig. 59 e). UAFM measurements show 2.5 GPa standard deviation while the TRIF elasticity measurement has 14.9 GPa standard deviation on the smooth silicon surface with 52 GPa expected reduced Young's modulus. This is due to the low spring constant of the probe at TRIF mode frequencies which does not match to the sample.

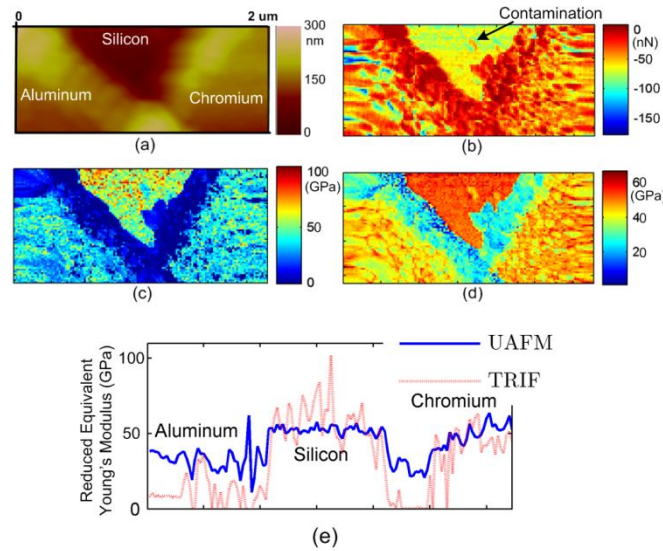


Figure 59 (a) Topography and (b) adhesion force image of a sample composed of aluminum, silicon, chromium. Elasticity is measured by (c) TRIF. (d) UAFM modes concurrently. (e) Elasticity data by two methods on the same line exhibit higher standard deviation by TRIF due to non-matching probe surface stiffness. Contamination on the silicon surface is clearly observed by UAFM [104].

6.2 Modeling of the FIRAT Probe for Ultrasonic TRIF mode

6.2.1 Analytical model

As it is explained in previous sections, FIRAT probe can be utilized for sensitive elasticity imaging on both compliant and stiff samples after a thorough calibration procedure. Although the calibration method worked out well, a better understanding is necessary to guide the experiments and even to decrease the calibration steps.

As the probe tip contacts the surface, some of the resonance frequencies of the probe changes. To quantitatively analyze the resonance frequency data, a calculation method for the frequency shifts with respect to the contact stiffness is necessary. There are analytical expressions for the frequency shifts in AFM cantilevers when the probe tip is in contact. These expressions are used to convert the contact resonance frequencies into contact stiffness data. Since FIRAT probe is a doubly supported beam, the analytical expressions of the cantilevers are not applicable. Therefore, the equations for resonance frequencies in FIRAT probe have to be derived by using the geometry shown in Fig. 60 (a). The used geometry is a doubly supported beam with $2L_I$ length and the center is attached to a spring. If the spring constant is zero, it means that the probe is not in contact. Since the tip is placed to the center of the probe, one can define the model as two connected beams with L_I length (Fig. 60 (b)).

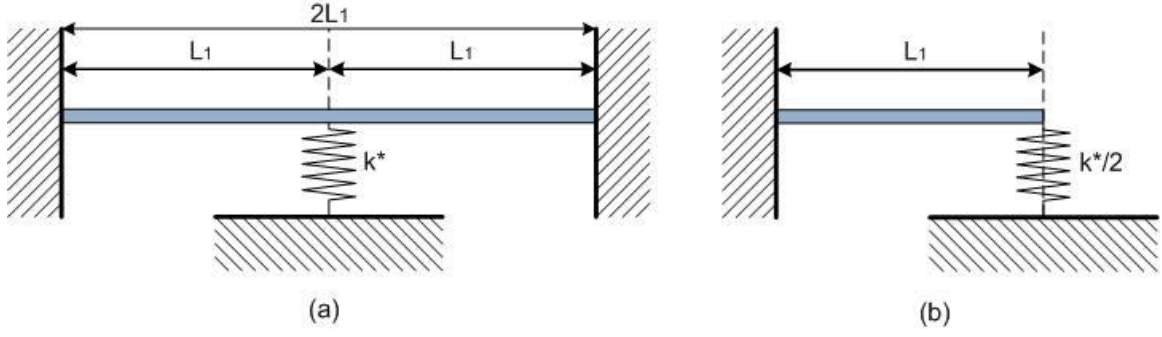


Figure 60 (a) The simple model of FIRAT probe in-contact. (b) The model is symmetrical and can be cut into half.

The vertical displacement of one of these two beams is expressed with y . The boundary conditions due to the supports are:

$$y=0, \frac{\partial y}{\partial x} = 0 \text{ for } x=0. \quad (6.2)$$

Although many modes will appear for a probe like FIRAT, frequency shifts occur in symmetric modes and these modes should be modeled. For a symmetric mode, the boundary conditions caused by the contact stiffness are the force on the spring and the slope of the probe:

$$\frac{\partial^3 y}{\partial x^3} = \frac{3k^*}{2k_c L_1^3} y, \frac{\partial y}{\partial x} = 0 \text{ for } x=L_1, \quad (6.3)$$

where k^* is the contact stiffness and k_c is the cantilever stiffness. If a general solution of the equation of motion is solved by using these boundary conditions, following characteristic equation is obtained:

$$\begin{aligned} &(\sin k_n L_1 + \sinh k_n L_1) * (k_n^3 (\cos k_n L_1 + \cosh k_n L_1) + \frac{3k^*}{2k_c L_1^3} (\sin k_n L_1 - \sinh k_n L_1)) = \\ &(\cos k_n L_1 - \cosh k_n L_1) * (k_n^3 (\sin k_n L_1 - \sinh k_n L_1) - \frac{3k^*}{2k_c L_1^3} (\cos k_n L_1 - \cosh k_n L_1)) \end{aligned} \quad (6.4)$$

The k_n values that fulfill the characteristic equation are the wavenumbers for the resonance modes. The resonance frequency, f_n , for k_n is:

$$f_n = \frac{(k_n L_1)^2}{c_c^2} \quad (6.5)$$

with

$$c_c = L_1 \sqrt{2\pi^4 \frac{\rho A}{EI}} \quad (6.6)$$

C_c is a constant, that contains density, ρ , cross-section area, A , and moment of inertia, I .

Note that, the geometry for this model is two dimensional with parameters for the width.

This model assumption is true when the width of the probe is smaller than the length of it.

However, a wider probe may have additional resonance orders since it behaves as a

plane, not a beam. The resonance frequencies with respect to the contact stiffness are

calculated by using Eq. 6.4 for a FIRAT probe with 100 μm length, 750 nm thickness,

and 2.5 μm width:

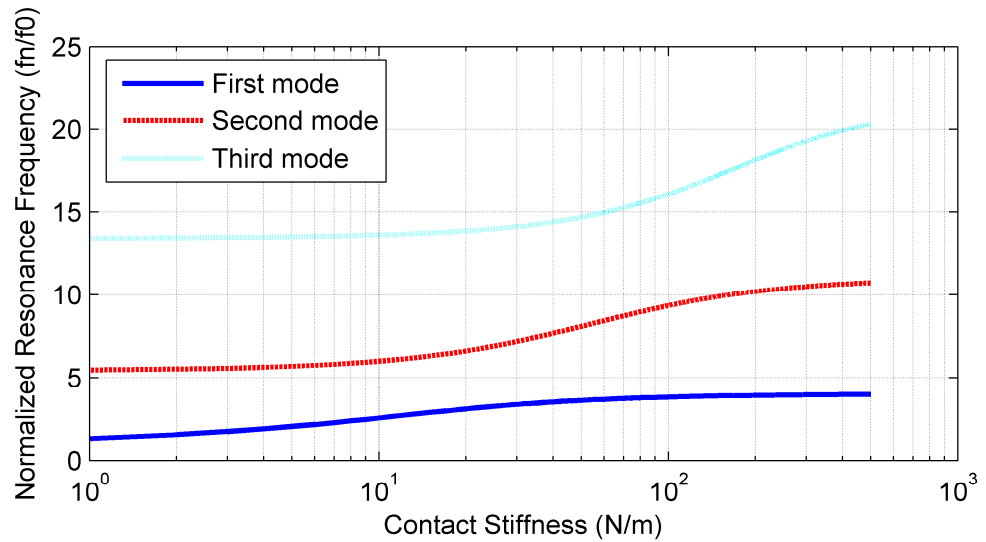


Figure 61 Normalized resonance frequencies for a thin FIRAT beam in-contact.

For the low contact stiffness values, first resonance frequency shifts, while the second and third resonances remain constant since they are much stiffer. Although the analytical solutions are helpful to quantify the resonance data, the equations cannot be reliable for wider probes. The commonly used FIRAT probe has at least 40 μm width so the analytical solution can only be used as a guideline.

6.2.2 Modal Analysis by the FEA Model

As explained before, an appropriate model of the FIRAT probe in-contact is needed to analyze the effects of the contact stiffness on frequency shifts. Nevertheless, the analytical expressions become complicated when handling the plates and the beam approximations are not suitable for the FIRAT probe. To solve these problems, modal analysis of FEA can be used. One can examine the mode shapes and the resonance shifts by using the modal analysis of FEA.

In FEA of FIRAT probe for ultrasonic TRIF mode measurements, SHELL181 is used to model the beam while COMBIN14 is used for the spring. Two sides of the beam are fixed while the spring element is attached between the center of the probe and a fixed location outside of the probe plane. To verify the results of the FEA analytically, the probe in previous section is simulated. This probe is a doubly supported beam with 100 μm length, 2.5 μm width and 0.75 μm thickness. The analytically calculated first and second resonance frequencies are plotted with the FEA results in the following figure. For a probe with these dimensions, FEA results agree with analytical solutions and the FEA model is verified by this calculation.

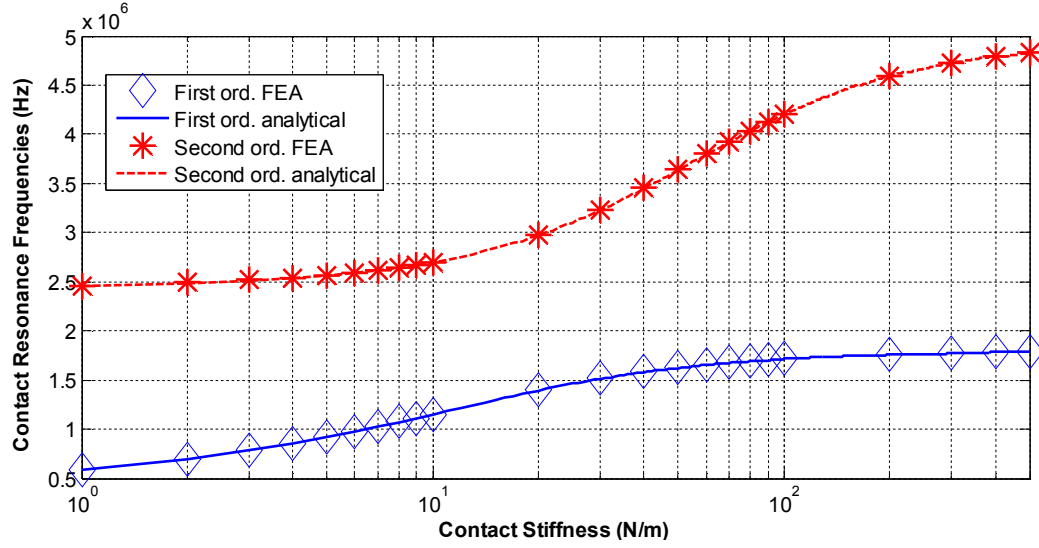


Figure 62 The FEA calculations for the contact resonances and the analytical solution.

The FIRAT probe simulated in this FEA model is not realistic since it is much narrower than the laser beam. In reality, the FIRAT probes used in the experiments are wider than 40 μm but the accuracy of the analytical model decreases for these probes. Since FEA is verified, it can be used for the actual FIRAT probes. To understand the real resonance frequencies of a FIRAT probe while it is in contact, a 100x100 μm FIRAT probe is simulated. The free resonances of the doubly supported probe are shown in Fig. 63 (a). One important difference from a narrower beam is the extra resonance occurring due to the width of the probe. The resonances at 569 kHz, 922 kHz, 1.44 MHz, 1.7 MHz, and 1.87 MHz are taking place at higher frequencies for a narrower beam. As seen in Fig. 63, the first free resonance order at 469 kHz moves to 637 kHz for an attached spring while for the narrow probe, this resonance becomes 1.79 MHz. This difference comes from the softening effect of the wider probe; the sides of the probe can still make a flapping motion while their motion is restricted for the narrow beam. In a mode like the second free mode at 569 kHz, the mode shape and frequency do not change with the

attached spring since the center does not move in this mode. The second symmetric mode occurs at 2.63 MHz for a free probe and this mode shifts to 2.69 MHz when the probe is in contact. The free resonance frequency at 922 kHz is an order due to the wider probe and cannot be predicted with the shown analytical expression. Unlike the resonances at 569 kHz or 1.44 MHz, this mode is affected by the contact and is shifted to 1.52 MHz.

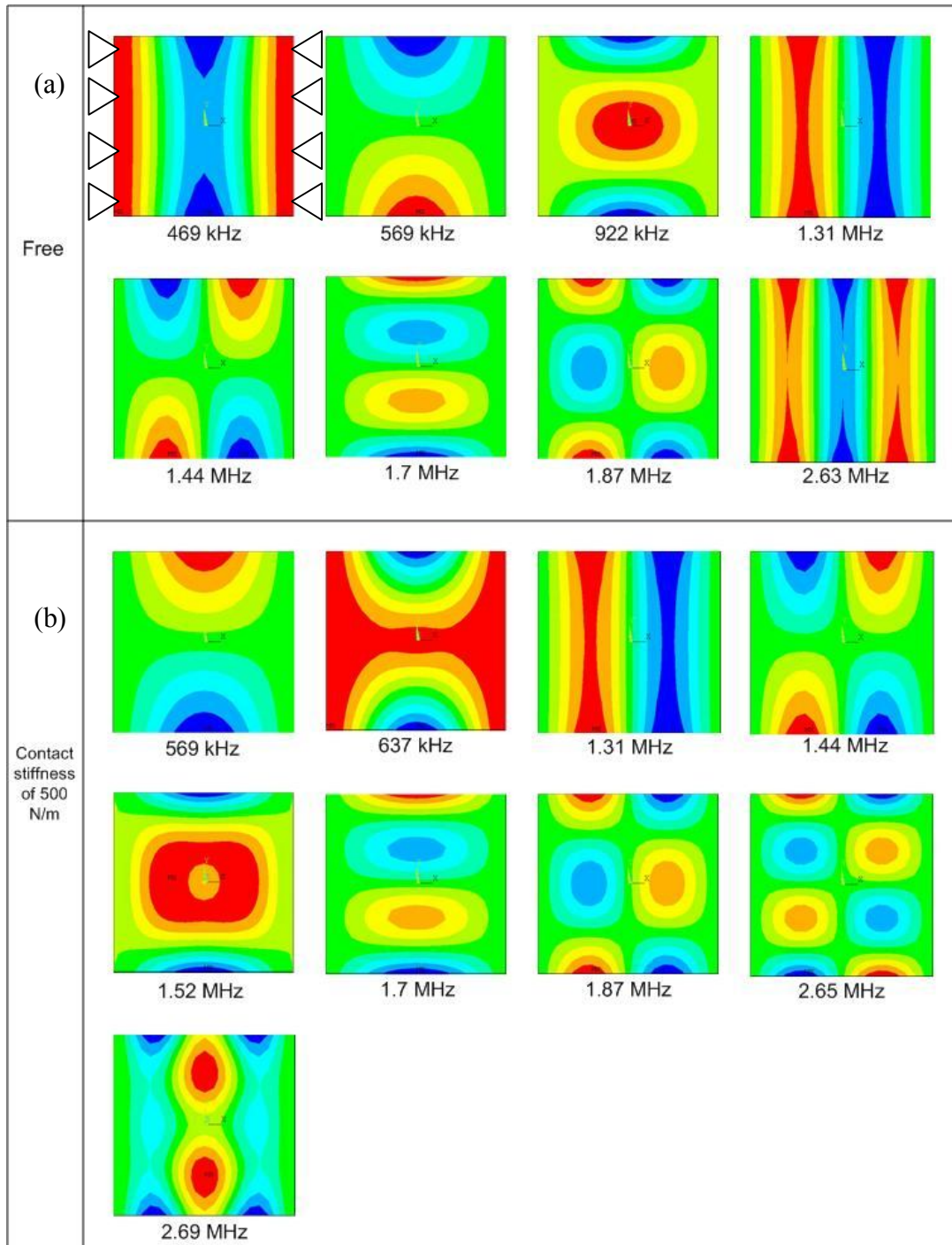


Figure 63 Mode shapes of a FIRAT probe when it is free and it is in contact.

The complicated nature of the plane geometry of the FIRAT probe makes it difficult to analyze quantitatively. While performing ultrasonic TRIF mode experiments, one should be aware of the asymmetric modes and choose resonance orders that may not be affected by these modes. In addition to this, FEA models can be helpful to select the modes and the frequency range.

6.2.3 Frequency Response Analysis with the Squeezed Film Effects

The modal analysis by FEA can be used to understand the mode shapes and the frequency shifts with respect to the contact stiffness. However, the frequency response and higher order resonances are affected by the squeezed film (Fig. 55) and the FIRAT probes in contact should be analyzed by including these effects. Modal projection technique is applied to couple the squeezed film with the modal analysis of FEA [105]. This technique adds the dissipative and stiffening effects of the fluid film between the beam and the substrate for damped harmonic analyses.

3-D FEA calculations are implemented by ANSYS 11.0.25. The 3-D structural plane element (PLANE45) is used to mesh the beam and it is clamped at two ends. In addition, the fluid film under the FIRAT probe is meshed with the squeezed film element (FLUID136). It is assumed that there is a spring connected to the center of the probe, representing the linearized contact stiffness. It is meshed with a spring element (COMBIN14). The two sides of the beam is clamped as it is in the FIRAT probes, while constant pressure is applied to the two remaining sides.

First, the resonance modes are calculated without the squeezed film effects. The mass normalized mode shape, Φ_i , of the i^{th} mode and the corresponding modal frequency,

w_i are computed using the modal analysis by FEA and recorded for further process. Then, the damping ratio, ζ_i , and the film-stiffness ratio, r_i , are extracted for each mode [106].

One can calculate the modal excitation force by using Φ_i of the resonance modes.

The P is the distributed pressure on the beam; in this case it is uniform pressure.

$$F_i = \int_A P \Phi_i dA. \quad (6.7)$$

The scalar modal displacement x_i of mode i for a frequency, w , can be calculated by using the following equation:

$$x_i = \frac{F_i}{w_i^2(1 + r_i) - w^2 + 2i\zeta_i w_i w}. \quad (6.8)$$

After solving Eq. 6.7 and 6.8, one can use MATLAB to compute the displacement on the beam for each mode:

$$\delta = \sum_{i=1}^k x_i \Phi_i. \quad (6.9)$$

Frequency response is computed using the described formulation. The simulated frequency response of the free FIRAT probe and in-contact probe are shown in the following figure. The damping on the beam and the amplified contact resonance frequencies (Fig. 64) demonstrate similar behavior to the experimental results (Fig. 65). As a result, this model can be used to analyze high frequency behavior of the FIRAT probes for sensitive elasticity measurements.

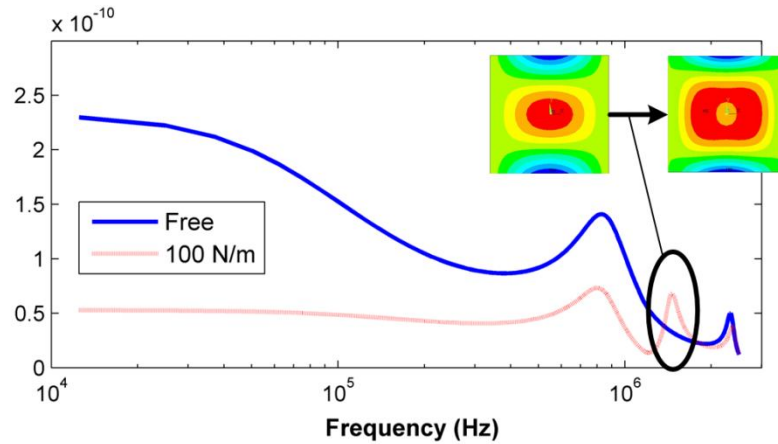


Figure 64 The simulated frequency response of the free FIRAT probe and probe in contact. Third mode is amplified by the contact.

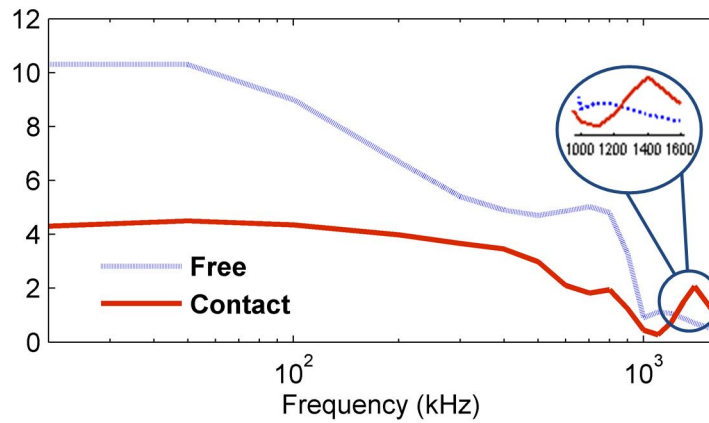


Figure 65 The measured frequency response of the free FIRAT probe and probe in contact.

At low frequencies, the contact limits the membrane movement and decreases the vibration amplitude. Interesting enough, the addition of the contact stiffness expands the area of vibration at the third resonance mode (Fig. 64). Expanding the area of movement amplified the vibration of the third mode. As a result, not only the frequency is shifted for the third mode (from 1.12 MHz to 1.445 MHz) but also the amplitude is increased.

6.3 Future Improvements for Ultrasonic TRIF Mode

The initial ultrasonic TRIF mode experiments are carried out by using FIRAT probe, which was introduced to measure interaction forces during intermittent contact mode. In these experiments, the vibration amplitude of a high frequency component is measured by FIRAT probes with different dimensions and gap heights. When the aim is to detect amplitude change due to the contact stiffness, one should use low Q probes since low Q factor slows down the rate of the amplitude change. However, Q factor should be higher to be able to detect resonances.

It is possible to modify the FIRAT probes so that they are low Q for interaction forces imaging but high Q while detecting contact resonances. This can be achieved by changing the excitation force for a mode. Currently, uniform pressure is applied through the electrostatic actuation and this uniform pressure causes different vibration modes (Eq. 6.7). One can pattern the electrodes to actuate a higher contact resonance mode with higher Q and this time P will not be constant. For example, to have higher Q in the third resonance mode (Fig. 64), P should match the mode shape, Φ_3 . Such kind of modification does not affect the performance of the FIRAT probe for TRIF mode, since no AC actuation is necessary for TRIF mode and the high frequency signal has small amplitude.

To obtain more reliable and quantitative contact stiffness data, an experimental set-up with resonance tracking capability should be used. To solve this issue, one should implement a high frequency detection scheme by employing a phase comparator and voltage controlled oscillator (VCO) (Fig. 66). A similar set-up was used before for fast ultrasonic AFM measurements [69, 74], however in these set-ups contact mode was used and a single contact force was applied. In the proposed ultrasonic TRIF imaging set-up

contact resonance frequencies are going to be calculated for many force points, which will give us 3-D subsurface imaging capability. This set-up will detect the phase of the vibration and change the actuation frequency accordingly to find the desired phase which is going to be the phase of the resonance order. The design of this circuit will define the how fast the resonance frequency can be tracked. The probe used in such a set-up can have higher Q values but one should not forget that high Q will cause ringing in the tapping data.

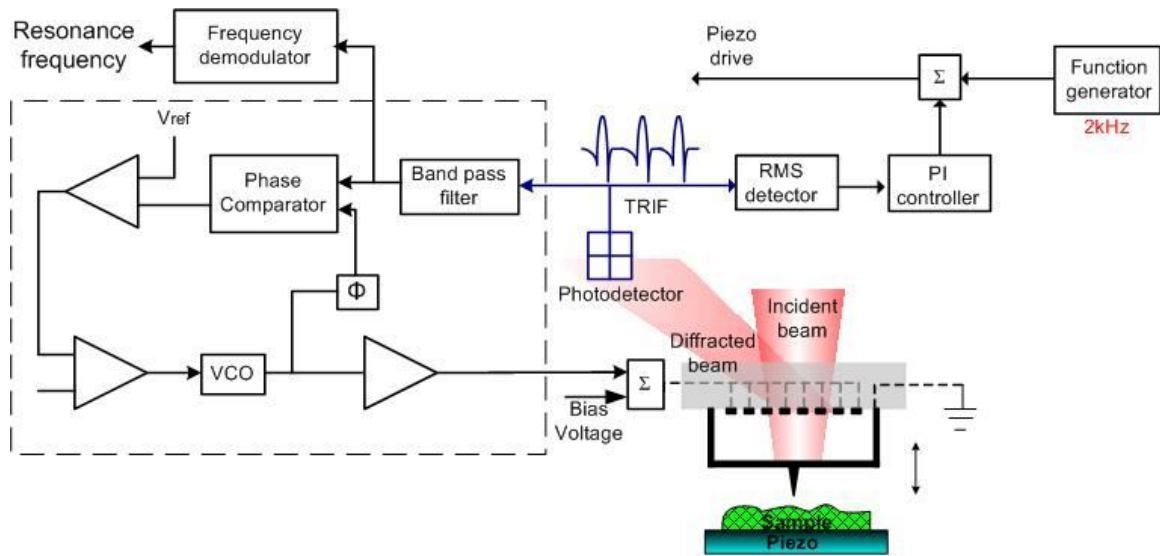


Figure 66 The proposed set-up for real-time resonance frequency tracking during the tap.

One of the advantages of the FIRAT probe is the embedded electrostatic actuation with high bandwidth, which provides clean actuation signal. In the UAFM and AFAM experiments, the tapping piezo, cantilevers with ZnO, and piezoelectric transducers attached to the samples are used. Different configurations show that it is important to actuate only the tip-sample contact and the probe; otherwise the vibrations will couple

into other structures and cause errors. The clean electrostatic actuation embedded in FIRAT probes makes it an attractive tool for ultrasonic AFM methods.

6.4 Chapter Summary

Mechanical properties imaging on nanocomposites is not feasible due to the reduced elasticity sensitivity for different stiffness regions during intermittent contact mode. A combined ultrasonic AFM and TRIF mode is introduced in this research to solve this problem. The experimental set-up, calibration steps for quantitative elasticity measurement and measurement results are presented in this chapter. Higher elasticity sensitivity over stiff samples –like silicon– is demonstrated. In addition to this, analytical and finite element models of a FIRAT probe in contact is presented. It is possible to improve the FIRAT probe for this combined method by using these modeling studies. This method can also be applied to cantilevers by including an additional piezoelectric transducer in the set-up.

CHAPTER 7

CONCLUSION

The aim of this research was to analyze and model quantitative mechanical properties measurements and subsurface imaging capability of AFM probes and to introduce techniques for providing better control on topography imaging and more sensitive elasticity measurement. For these purposes, thorough understanding of the current AFM techniques is developed, analytical, finite element, and Simulink models are constructed, and experiments are performed. Based on these models and the understanding, different techniques are introduced by utilizing FIRAT, which is an active AFM probe with broad bandwidth.

Subsurface imaging modeling studies presented in this thesis shows that finite size subsurface structures can be detected by using AFM. In addition, the 3-D FEA model explained in chapter 2 can also be implemented for any quasistatic probe contact based elasticity measurement technique for investigating subsurface imaging capability. One can measure the elasticity mapping of a surface and use this model to analyze the depth and size of the embedded nanostructures, or one can use this model prior to experiments to determine if the subsurface structures are detectable.

FIRAT is an AFM probe that can be utilized to measure interaction forces during intermittent contact mode. Probe dynamics, stiffness, stiffness ambiguity, assumed contact mechanics model, and noise are important parameters that determine the error rates on the measured mechanical properties. The guidelines generated in chapter 4 are not only useful for designing FIRAT probes but also useful for analyzing and improving

other time-resolved interaction forces measurement techniques such as pulsed-force mode and torsional cantilevers.

Since using soft probes or decreasing the contact time in a tap causes instability during intermittent contact mode, topography imaging may have inaccuracies on compliant samples in a stable scan. This problem can be solved by employing an active probe with high actuation bandwidth –like FIRAT probe– and applying active tip control (ATC). With ATC, users don't have to compromise either stability or reduced indentation.

The accuracy of the elasticity measurement by intermittent contact (force-displacement curves, pulsed-force mode, torsional cantilevers, and FIRAT probes) highly depends on the probe stiffness (Fig. 42). The user should select the proper probe for the material of interest; however, this constitutes a challenge on the samples with different stiffness regions, such as nanobeads on polymers. It is possible to characterize such samples by combining ultrasonic AFM methods with intermittent contact mode. Combined ultrasonic AFM and TRIF mode is a promising technique that provides high sensitivity on a broad range of materials with non-destructive topography imaging.

7.1 Contributions

The contributions of this work are summarized as the following:

- A 3-D FEA model of AFM tip-sample contact is constructed for simulating subsurface imaging by means of elasticity measurement. This model is verified experimentally by employing ultrasonic AFM methods. The results of this study is published in Journal of Applied Physics [65].

- Mechanical properties imaging capability of FIRAT probe, which is an active and broadband AFM probe, is investigated. Analytical and Simulink models are used to generate realistic taps and to study several parameters such as dynamics and material properties. Then, guidelines for the sensitivity of the mechanical properties measurements with respect to the probe dynamics, stiffness, noise, and contact mechanics assumptions are generated by combining these models. Some of the modeling studies are used in an article published in Review of Scientific Instruments [50].
- To allow the user to control the applied contact force during intermittent contact mode, active nature and high bandwidth of FIRAT probe is utilized and active tip control (ATC) method is introduced. An experimental set-up for ATC is designed and experimental studies that verify the increased accuracy in topography imaging are performed. Then, previously introduced Simulink models are used to analyze ATC operation for a better understanding of the interaction forces. Some of the results of this study are published in Ultramicroscopy [99].
- A combined ultrasonic AFM and interaction forces imaging method is introduced to solve the reduced elasticity measurement sensitivity on stiff materials. An experimental set-up is built to test this idea, the calibration steps for quantitative analysis are determined, and the increased elasticity sensitivity of the combined operation is verified. In addition to these, analytical and finite element modeling studies are performed to understand the contact resonance mechanism of the FIRAT probes that may decrease the calibration steps and can help improving the

probes for combined operation. Some of the results of this research is published in Review of Scientific Instruments [104].

7.2 Future Work

The introduced models and methods in this thesis answered many questions related to improving the subsurface and mechanical properties mapping during topography imaging. The suggested future works related to this thesis are listed as the following:

- ***Spring softening and ultrasonic TRIF mode:*** One can employ spring softening to the FIRAT probes and then operate combined ultrasonic AFM and TRIF mode. This combination can extend the sensitive elasticity measurement to both softer and stiffer materials than the nominal elasticity measurement range of that probe.
- ***Viscoelasticity measurements by ultrasonic TRIF mode:*** In this thesis, we used high frequency component of ultrasonic TRIF mode to analyze stiff materials and assumed that the material is lossless. TRIF mode is more sensitive to soft materials like polymers and biological specimens. One can calculate the elasticity of the compliant material by using TRIF mode measurements and analyze the ultrasonic AFM outputs for viscoelasticity.
- ***Lateral stiffness measurements by ultrasonic TRIF mode:*** In this research, the FIRAT probe is actuated at flexural vibrations and the contact stiffness is calculated. However, it is possible to actuate a torsional resonance of the probe, to monitor the lateral output of the photodiode and to determine the lateral stiffness by analyzing this data during a tap.
- ***Experimental improvements for ultrasonic TRIF mode:*** Current ultrasonic TRIF mode measures the amplitude of a high frequency vibration to calculate the contact

stiffness. One can add a resonance tracking circuitry to obtain a faster and more accurate detection scheme. On top of this, the actuation scheme of the FIRAT probe can be modified for obtaining higher quality factor for an individual contact resonance, which is not possible for cantilevers.

- ***Subsurface imaging by ultrasonic TRIF mode:*** The 3-D subsurface imaging models show that different contact forces are necessary to resolve the depth information of the embedded structures. However, current ultrasonic AFM techniques employ contact mode AFM and the tip –as well as the sample– deforms during multiple scans. In addition to this, many force points mean longer data acquisition. On the other hand, one can employ ultrasonic TRIF mode (preferably with a faster lock-in amplifier than SRS844) and measure the contact stiffness during a tap, which is non-destructive and fast.
- ***Combined ATC and ultrasonic TRIF mode:*** In some applications, such as relaxation time measurements, one can employ ATC, keep the force constant in a tap, and then measure the UAFM amplitude during that constant force.
- ***Piezoresponse measurements by FIRAT probe:*** The conductive FIRAT probes can be utilized for the characterization of the piezoelectric samples. The DC bias and small amplitude high frequency signal causes deflections on the probe. When the probe tip acts as an electrical contact on the piezoelectric materials the material will start to vibrate because of the applied high frequency signal. The combination of these two vibrations can be detected by monitoring the PD output and analysis of this signal provides piezoelectric properties.

REFERENCES

- [1] G. Binnig, C. F. Quate, and C. Gerber, "Atomic Force Microscope," *Physical Review Letters*, vol. 56, p. 930, 1986.
- [2] S. J. T. van Noort, O. H. Willemsen, K. O. van der Werf, B. G. de Grooth, and J. Greve, "Mapping Electrostatic Forces Using Higher Harmonics Tapping Mode Atomic Force Microscopy in Liquid," *Langmuir*, vol. 15, pp. 7101-7107, 1999.
- [3] D. Erts, B. Polyakov, H. k. Olin, and E. Tuite, "Spatial and Mechanical Properties of Dilute DNA Monolayers on Gold Imaged by AFM," *The Journal of Physical Chemistry B*, vol. 107, pp. 3591-3597, 2003.
- [4] S. E. Cross, J. Yu-Sheng, R. Jianyu, and J. K. Gimzewski, "Nanomechanical analysis of cells from cancer patients," *Nature Nanotechnology*, vol. 2, pp. 780-783, 2007.
- [5] O. Marti, M. Holzwarth, and M. Beil, "Measuring the nanomechanical properties of cancer cells by digital pulsed force mode imaging," *Nanotechnology*, vol. 19, p. 384015, 2008.
- [6] V. Vadillo-Rodriguez, H. J. Busscher, W. Norde, J. de Vries, R. J. B. Dijkstra, I. Stokroos, and H. C. van der Mei, "Comparison of Atomic Force Microscopy Interaction Forces between Bacteria and Silicon Nitride Substrata for Three Commonly Used Immobilization Methods," *Appl. Environ. Microbiol.*, vol. 70, pp. 5441-5446, September 1, 2004 2004.
- [7] V. V. Tsukruk, A. Sidorenko, V. V. Gorbunov, and S. A. Chizhik, "Surface Nanomechanical Properties of Polymer Nanocomposite Layers," *Langmuir*, vol. 17, pp. 6715-6719, 2001.
- [8] J. Song, X. Wang, E. Riedo, and Z. L. Wang, "Elastic Property of Vertically Aligned Nanowires," *Nano Letters*, vol. 5, pp. 1954-1958, 2005.
- [9] M. Lucas, W. Mai, R. Yang, Z. L. Wang, and E. Riedo, "Aspect Ratio Dependence of the Elastic Properties of ZnO Nanobelts," *Nano Letters*, vol. 7, pp. 1314-1317, 2007.
- [10] N. A. Burnham and R. J. Colton, "Measuring the nanomechanical properties and surface forces of materials using an atomic force microscope," *Journal of Vacuum Science & Technology A: Vacuum, Surfaces, and Films*, vol. 7, pp. 2906-2913, 1989.
- [11] N. Oyabu, Custance, Oacute, scar, I. Yi, Y. Sugawara, and S. Morita, "Mechanical Vertical Manipulation of Selected Single Atoms by Soft

- Nanoindentation Using Near Contact Atomic Force Microscopy," *Physical Review Letters*, vol. 90, p. 176102, 2003.
- [12] V. Instruments, "Veeco Probes," in Available at: <https://www.veecoprobes.com/>, 2009.
 - [13] K. E. Petersen and C. R. Guarnieri, "Young's modulus measurements of thin films using micromechanics," *Journal of Applied Physics*, vol. 50, pp. 6761-6766, 1979.
 - [14] I. Palaci, S. Fedrigo, H. Brune, C. Klinke, M. Chen, and E. Riedo, "Radial Elasticity of Multiwalled Carbon Nanotubes," *Physical Review Letters*, vol. 94, p. 175502, 2005.
 - [15] B. Bhushan, *Nanotribology and nanomechanics : an introduction*. Berlin :: Springer, 2005.
 - [16] B. Bhushan, *Handbook of micro/nano tribology / edited by Bharat Bhushan*. Boca Raton: CRC Press, 1995.
 - [17] S. A. S. Asif, K. J. Wahl, and R. J. Colton, "Nanoindentation and contact stiffness measurement using force modulation with a capacitive load-displacement transducer," *Review of Scientific Instruments*, vol. 70, pp. 2408-2413, 1999.
 - [18] N. A. Burnham, R. J. Colton, and H. M. Pollock, "Interpretation of force curves in force microscopy," *Nanotechnology*, vol. 4, pp. 64-80, 1993.
 - [19] E. L. Florin, V. T. Moy, and H. E. Gaub, "Adhesion forces between individual ligand-receptor pairs," *Science*, vol. 264, pp. 415-417, April 15, 1994 1994.
 - [20] A. Kovalev, H. Shulha, M. Lemieux, N. Myshkin, and V. V. Tsukruk, "Nanomechanical probing of layered nanoscale polymer films with atomic force microscopy," *J. Mater. Res.*, vol. 19, pp. 716-728, 2003.
 - [21] P. Maivald, H. J. Butt, S. A. C. Gould, C. B. Prater, B. Drake, J. A. Gurley, V. B. Elings, and P. K. Hansma, "Using force modulation to image surface elasticities with the atomic force microscope," *Nanotechnology*, vol. 2, pp. 103-106, 1991.
 - [22] A. Rosa-Zeiser, E. Weilandt, S. Hild, and O. Marti, "The simultaneous measurement of elastic, electrostatic and adhesive properties by scanning force microscopy: pulsed-force mode operation," *Measurement Science and Technology*, vol. 8, pp. 1333-1338, 1997.
 - [23] U. Rabe, K. Janser, and W. Arnold, "Vibrations of free and surface-coupled atomic force microscope cantilevers: Theory and experiment," *Review of Scientific Instruments*, vol. 67, pp. 3281-3293, Sep 1996.

- [24] B. D. Huey, "AFM and Acoustics: Fast, Quantitative Nanomechanical Mapping," *Annual Review of Materials Research*, vol. 37, pp. 351-385, 08/01 2007.
- [25] U. Rabe, S. Amelio, E. Kester, V. Scherer, S. Hirsekorn, and W. Arnold, "Quantitative determination of contact stiffness using atomic force acoustic microscopy," *Ultrasonics*, vol. 38, pp. 430-437, 2000.
- [26] K. Yamanaka, A. Noguchi, T. Tsuji, T. Koike, and T. Goto, "Quantitative material characterization by ultrasonic AFM," *Surface and Interface Analysis*, vol. 27, pp. 600-606, May-Jun 1999.
- [27] U. Rabe, S. Amelio, E. Kester, V. Scherer, S. Hirsekorn, and W. Arnold, "Quantitative determination of contact stiffness using atomic force acoustic microscopy," *Ultrasonics*, vol. 38, p. 430, 2000.
- [28] K. Yamanaka, H. Ogiso, and O. Kolosov, "Ultrasonic Force Microscopy for Nanometer Resolution Subsurface Imaging," *Applied Physics Letters*, vol. 64, pp. 178-180, Jan 1994.
- [29] S. A. U. Rabe, M. Kopycinska, S. Hirsekorn, M. Kempf, M. Göken, W. Arnold, "Imaging and measurement of local mechanical material properties by atomic force acoustic microscopy," *Surface and Interface Analysis*, vol. 33, pp. 65-70, 2002.
- [30] M. A. Hussein and H. Jun, "Materials' impact on interconnect process technology and reliability," *Semiconductor Manufacturing, IEEE Transactions on*, vol. 18, pp. 69-85, 2005.
- [31] A. F. Sarioglu, A. Atalar, and F. L. Degertekin, "Modeling the effect of subsurface interface defects on contact stiffness for ultrasonic atomic force microscopy," *Appl. Phys. Lett.*, vol. 84, p. 5368, 2004.
- [32] G. Xu, D. E. Eastman, B. Lai, Z. Cai, I. McNulty, S. Frigo, I. C. Noyan, and C. K. Hu, "Nanometer precision metrology of submicron Cu/SiO₂ interconnects using fluorescence and transmission x-ray microscopy," *Journal of Applied Physics*, vol. 94, pp. 6040-6049, 2003.
- [33] L. Tetard, A. Passian, R. M. Lynch, B. H. Voy, G. Shekhawat, V. Dravid, and T. Thundat, "Elastic phase response of silica nanoparticles buried in soft matter," *Applied Physics Letters*, vol. 93, pp. 133113-3, 2008.
- [34] G. S. Shekhawat and V. P. Dravid, "Nanoscale imaging of buried structures via scanning near-field ultrasound holography," *Science*, vol. 310, p. 89, 2005.
- [35] A. Briggs, *Acoustic microscopy*. Oxford :: Clarendon Press ;, 1992.
- [36] *Springer handbook of nanotechnology*. Berlin ;: Springer, 2004.

- [37] B. Hecht, B. Sick, U. P. Wild, V. Deckert, R. Zenobi, O. J. F. Martin, and D. W. Pohl, "Scanning near-field optical microscopy with aperture probes: Fundamentals and applications," *The Journal of Chemical Physics*, vol. 112, pp. 7761-7774, 8 may 2000 2000.
- [38] E. Betzig, A. Lewis, A. Harootunian, M. Isaacson, E. Kratschmer, and "Near-Field Scanning Optical Microscopy (NSOM)," *Imaging Technology*, 1986.
- [39] D. Barchiesi, C. Girard, O. J. F. Martin, D. Van Labeke, and D. Courjon, "Computing the optical near-field distributions around complex subwavelength surface structures: A comparative study of different methods," *Physical Review E*, vol. 54, pp. 4285-4292, October 1996 1996.
- [40] X. Su, C. Stagarescu, G. Xu, D. E. Eastman, I. McNulty, S. P. Frigo, Y. Wang, C. C. Retsch, I. C. Noyan, and C. K. Hu, "Quantitative nanoscale metrology study of Cu/SiO₂ interconnect technology using transmission x-ray microscopy," *Applied Physics Letters*, vol. 77, pp. 3465-3467, 2000.
- [41] D. Y. Parkinson, G. McDermott, L. D. Etkin, M. A. Le Gros, and C. A. Larabell, "Quantitative 3-D imaging of eukaryotic cells using soft X-ray tomography," *Journal of Structural Biology*, vol. 162, pp. 380-386, 2008.
- [42] Y. Kazushi, O. Hisato, and K. Oleg, "Ultrasonic force microscopy for nanometer resolution subsurface imaging," *Applied Physics Letters*, vol. 64, pp. 178-180, 1994.
- [43] T. Tsuji and K. Yamanaka, "Observation by ultrasonic atomic force microscopy of reversible displacement of subsurface dislocations in highly oriented pyrolytic graphite," *Nanotechnology*, vol. 12, pp. 301-307, 2001.
- [44] J. Tamayo and R. Garcia, "Effects of elastic and inelastic interactions on phase contrast images in tapping-mode scanning force microscopy," *Applied Physics Letters*, vol. 71, pp. 2394-2396, 1997.
- [45] O. Sahin and A. Atalar, "Simulation of higher harmonics generation in tapping-mode atomic force microscopy," *Appl. Phys. Lett.*, vol. 79, p. 4455, 2001.
- [46] M. Balantekin and A. Atalar, "Enhancing higher harmonics of a tapping cantilever by excitation at a submultiple of its resonance frequency," *Physical Review B (Condensed Matter and Materials Physics)*, vol. 71, pp. 125416-6, 2005.
- [47] O. Sahin, S. Magonov, C. Su, C. F. Quate, and O. Solgaard, "An atomic force microscope tip designed to measure time-varying nanomechanical forces," *Nat Nano*, vol. 2, pp. 507-514, 2007.

- [48] G. G. Yaralioglu, A. Atalar, S. R. Manalis, and C. F. Quate, "Analysis and design of an interdigital cantilever as a displacement sensor," *Journal of Applied Physics*, vol. 83, pp. 7405-7415, 1998.
- [49] A. F. Sarioglu and O. Solgaard, "Cantilevers with integrated sensor for time-resolved force measurement in tapping-mode atomic force microscopy," *Applied Physics Letters*, vol. 93, pp. 023114-3, 2008.
- [50] A. G. Onaran, M. Balantekin, W. Lee, W. L. Hughes, B. A. Buchine, R. O. Guldiken, Z. Parlak, C. F. Quate, and F. L. Degertekin, "A new atomic force microscope probe with force sensing integrated readout and active tip," *Review of Scientific Instruments*, vol. 77, pp. 023501-7, 2006.
- [51] F. L. Degertekin, A. G. Onaran, M. Balantekin, W. Lee, N. A. Hall, and C. F. Quate, "Sensor for direct measurement of interaction forces in probe microscopy," *Applied Physics Letters*, vol. 87, pp. 213109-3, 2005.
- [52] M. Balantekin, A. G. Onaran, and F. L. Degertekin, "Quantitative mechanical characterization of materials at the nanoscale through direct measurement of time-resolved tip–sample interaction forces," *Nanotechnology*, vol. 19, p. 085704, 2008.
- [53] C. Su, L. Huang, and K. Kjoller, "Direct measurement of tapping force with a cantilever deflection force sensor," *Ultramicroscopy*, vol. 100, pp. 233-239, 2004.
- [54] K. L. Johnson, *Contact Mechanics*: Cambridge University Press 1985, 1985.
- [55] G. G. Yaralioglu, F. L. Degertekin, K. B. Crozier, and C. F. Quate, "Contact stiffness of layered materials for ultrasonic atomic force microscopy," *Journal of Applied Physics*, vol. 87, pp. 7491-7496, 2000.
- [56] H. Shulha, A. Kovalev, N. Myshkin, and V. V. Tsukruk, "Some aspects of AFM nanomechanical probing of surface polymer films," *European Polymer Journal*, vol. 40, pp. 949-956, 2004.
- [57] G. S. Kino and C. S. DeSilets, "Design of slotted transducer arrays with matched backings," *Ultrasonic Imaging*, vol. 1, pp. 189-209, 1979.
- [58] B. Honein, A. M. B. Braga, P. Barbone, and G. Herrmann, "Wave Propagation in Piezoelectric Layered Media with Some Applications," *Journal of Intelligent Material Systems and Structures*, vol. 2, pp. 542-557, October 1, 1991 1991.
- [59] K. B. Crozier, G. G. Yaralioglu, F. L. Degertekin, J. D. Adams, S. C. Minne, and C. F. Quate, "Thin film characterization by atomic force microscopy at ultrasonic frequencies," *Applied Physics Letters*, vol. 76, pp. 1950-1952, 2000.

- [60] G. S. Batog, A. S. Baturin, V. S. Bormashov, and E. P. Sheshin, "Calculation of the thicknesses and elastic properties of thin-film coatings using atomic-force acoustic microscopy data," *Technical Physics*, vol. 51, pp. 1084-1089, Aug 2006.
- [61] G. Batog, A. Baturin, V. Bormashov, and E. Sheshin, "Calculation of the thicknesses and elastic properties of thin-film coatings using atomic-force acoustic microscopy data," *Technical Physics*, vol. 51, pp. 1084-1089, 2006.
- [62] H. Geisler, M. Hoehn, M. Rambach, M. A. Meyer, E. Zschech, M. Mertig, A. Romanov, M. Bobeth, W. Pompe, and R. E. Geer, "Elastic mapping of sub-surface defects by ultrasonic force microscopy: limits of depth sensitivity," in *Microscopy of Semiconducting Materials: Institute of Physics Conference Series* 169 (IOP Publishing, Bristol, UK, 2001), 2001, pp. 527-530.
- [63] S. Amelio, A. V. Goldade, U. Rabe, V. Scherer, B. Bhushan, and W. Arnold, "Measurements of elastic properties of ultra-thin diamond-like carbon coatings using atomic force acoustic microscopy," *Thin Solid Films*, vol. 392, pp. 75-84, 2001.
- [64] U. Rabe, S. Amelio, M. Kopycinska, S. Hirsekorn, M. Kempf, M. Goken, and W. Arnold, "Imaging and measurement of local mechanical material properties by atomic force acoustic microscopy," *Surface and Interface Analysis*, vol. 33, pp. 65-70, Feb 2002.
- [65] Z. Parlak and F. L. Degertekin, "Contact stiffness of finite size subsurface defects for atomic force microscopy: Three-dimensional finite element modeling and experimental verification," *Journal of Applied Physics*, vol. 103, pp. 114910-8, 2008.
- [66] A. V. Vairagar, S. G. Mhaisalkar, A. Krishnamoorthy, K. N. Tu, A. M. Gusak, M. A. Meyer, and E. Zschech, "In situ observation of electromigration-induced void migration in dual-damascene Cu interconnect structures," *Applied Physics Letters*, vol. 85, pp. 2502-2504, 2004.
- [67] M. K.-M. A. B. K. R. H. G. D. C. Hurley, "Quantitative Elastic-Property Measurements at the Nanoscale with Atomic Force Acoustic Microscopy," *Advanced Engineering Materials*, vol. 7, pp. 713-718, 2005.
- [68] D. C. Hurley, K. Shen, N. M. Jennett, and J. A. Turner, "Atomic force acoustic microscopy methods to determine thin-film elastic properties," *Journal of Applied Physics*, vol. 94, pp. 2347-2354, 2003.
- [69] K. Yamanaka, Y. Maruyama, T. Tsuji, and K. Nakamoto, "Resonance frequency and Q factor mapping by ultrasonic atomic force microscopy," *Applied Physics Letters*, vol. 78, pp. 1939-1941, Mar 2001.

- [70] O. V. Kolosov, M. R. Castell, C. D. Marsh, G. A. D. Briggs, T. I. Kamins, and R. S. Williams, "Imaging the elastic nanostructure of Ge islands by ultrasonic force microscopy," *Physical Review Letters*, vol. 81, pp. 1046-1049, Aug 1998.
- [71] J. A. Turner, S. Hirsekorn, U. Rabe, and W. Arnold, "High-frequency response of atomic-force microscope cantilevers," *J. Appl. Phys.*, vol. 82, p. 966, 1997.
- [72] U. Rabe, J. Turner, and W. Arnold, "Analysis of the high-frequency response of atomic force microscope cantilevers," *Applied Physics A: Materials Science & Processing*, vol. 66, p. S277, 1998.
- [73] J. A. Turner, S. Hirsekorn, U. Rabe, and W. Arnold, "High-frequency response of atomic-force microscope cantilevers," *Journal of Applied Physics*, vol. 82, pp. 966-979, 1997.
- [74] D. C. Hurley, M. Kopycinska-Muller, E. D. Langlois, A. B. Kos, and N. Barbosa, "Mapping substrate/film adhesion with contact-resonance-frequency atomic force microscopy," *Applied Physics Letters*, vol. 89, Jul 2006.
- [75] A. P. McGuigan, B. D. Huey, G. A. D. Briggs, O. V. Kolosov, Y. Tsukahara, and M. Yanaka, "Measurement of debonding in cracked nanocomposite films by ultrasonic force microscopy," *Applied Physics Letters*, vol. 80, pp. 1180-1182, 2002.
- [76] T. Tsuji, H. Ogiso, J. Akedo, S. Saito, K. Fukuta, and K. Yamanaka, "Evaluation of Domain Boundary of Piezo/Ferroelectric Material by Ultrasonic Atomic Force Microscopy," *Japanese Journal of Applied Physics*, vol. 43, p. 2907, 2004.
- [77] R. Garcia, C. J. Gomez, N. F. Martinez, S. Patil, C. Dietz, and R. Magerle, "Identification of Nanoscale Dissipation Processes by Dynamic Atomic Force Microscopy," *Physical Review Letters*, vol. 97, pp. 016103-4, 2006.
- [78] M. Stark, R. W. Stark, W. M. Heckl, and R. Guckenberger, "Inverting dynamic force microscopy: From signals to time-resolved interaction forces," *Proceedings of the National Academy of Sciences of the United States of America*, vol. 99, pp. 8473-8478, 06/25 2002.
- [79] J. Tamayo and R. Garcia, "Relationship between phase shift and energy dissipation in tapping-mode scanning force microscopy," *Applied Physics Letters*, vol. 73, pp. 2926-2928, 1998.
- [80] M. Balantekin and A. Atalar, "Power dissipation analysis in tapping-mode atomic force microscopy," *Physical Review B*, vol. 67, p. 193404, 2003.
- [81] N. F. Martinez, S. Patil, J. R. Lozano, and R. Garcia, "Enhanced compositional sensitivity in atomic force microscopy by the excitation of the first two flexural modes," *Applied Physics Letters*, vol. 89, pp. 153115-3, 2006.

- [82] J. R. Lozano and R. Garcia, "Theory of Multifrequency Atomic Force Microscopy," *Physical Review Letters*, vol. 100, p. 076102, 2008.
- [83] R. W. Stark, "Dynamics of repulsive dual-frequency atomic force microscopy," *Applied Physics Letters*, vol. 94, pp. 063109-3, 2009.
- [84] R. W. Stark and W. M. Heckl, "Fourier transformed atomic force microscopy: tapping mode atomic force microscopy beyond the Hookian approximation," *Surface Science*, vol. 457, pp. 219-228, 2000.
- [85] M. Balantekin and A. Atalar, "Enhanced higher-harmonic imaging in tapping-mode atomic force microscopy," *Applied Physics Letters*, vol. 87, pp. 243513-3, 2005.
- [86] O. Sahin, G. Yaralioglu, R. Grow, S. F. Zappe, A. Atalar, C. Quate, and O. Solgaard, "High-resolution imaging of elastic properties using harmonic cantilevers," *Sensors and Actuators A: Physical*, vol. 114, pp. 183-190, 2004.
- [87] P. J. de Pablo, J. Colchero, J. Gomez-Herrero, and A. M. Baro, "Jumping mode scanning force microscopy," *Applied Physics Letters*, vol. 73, pp. 3300-3302, 1998.
- [88] A. Gigler, C. Gnahn, O. Marti, T. Schimmel, and S. Walheim, "Towards quantitative materials characterization with Digital Pulsed Force Mode imaging," *Journal of Physics: Conference Series*, vol. 61, pp. 346-351, 2007.
- [89] "PeakForce QNM." vol. 2010 Santa Barbara/CA: Veeco Instruments Inc, 2009, p. pdf.
- [90] B. Van Gorp, A. G. Onaran, and F. L. Degertekin, "Integrated dual grating method for extended range interferometric displacement detection in probe microscopy," *Applied Physics Letters*, vol. 91, pp. 083101-3, 2007.
- [91] O. Sahin and N. Erina, "High-resolution and large dynamic range nanomechanical mapping in tapping-mode atomic force microscopy," *Nanotechnology*, vol. 19, p. 445717, 2008.
- [92] S. D. Senturia, *Microsystem design*. Boston :: Kluwer Academic Publishers, 2001.
- [93] H. Torun, K. K. Sarangapani, and F. L. Degertekin, "Spring constant tuning of active atomic force microscope probes using electrostatic spring softening effect," *Applied Physics Letters*, vol. 91, pp. 253113-3, 2007.
- [94] L. F. Drummy, P. K. Miska, and D. C. Martin, "Plasticity in pentacene thin films," *Journal of Materials Science*, vol. 39, pp. 4465-4474, 2004.

- [95] L. F. Drummy and D. C. Martin, "Thickness-Driven Orthorhombic to Triclinic Phase Transformation in Pentacene Thin Films," *Advanced Materials*, vol. 17, pp. 903-907, 2005.
- [96] W. Lee, N. A. Hall, and F. L. Degertekin, "A grating-assisted resonant-cavity-enhanced optical displacement detection method for micromachined sensors," *Applied Physics Letters*, vol. 85, pp. 3032-3034, 2004.
- [97] H. Torun, J. Sutanto, K. K. Sarangapani, P. Joseph, F. L. Degertekin, and C. Zhu, "A micromachined membrane-based active probe for biomolecular mechanics measurement," *Nanotechnology*, vol. 18, p. 165303, 2007.
- [98] F. J. Giessibl, "Advances in atomic force microscopy," *Reviews of Modern Physics*, vol. 75, p. 949, 2003.
- [99] Z. Parlak, R. Hadizadeh, M. Balantekin, and F. Levent Degertekin, "Controlling tip-sample interaction forces during a single tap for improved topography and mechanical property imaging of soft materials by AFM," *Ultramicroscopy*, vol. 109, pp. 1121-1125, 2009.
- [100] J. Brandrup and E. H. Immergut, *Polymer Handbook*: John Wiley & Sons, 1989.
- [101] V. V. Tsukruk, Z. Huang, S. A. Chizhik, and V. V. Gorbunov, "Probing of Micromechanical Properties of Compliant Polymeric Materials," *Journal of Materials Science*, vol. 33, pp. 4905-4909, 1998.
- [102] E. Kester, U. Rabe, L. Presmanes, P. Tailhades, and W. Arnold, "Measurement of mechanical properties of nanoscaled ferrites using atomic force microscopy at ultrasonic frequencies," *Nanostruct. Mater.*, vol. 12, p. 779, 1999.
- [103] H. U. Krottil, T. Stifter, and O. Marti, "Concurrent measurement of adhesive and elastic surface properties with a new modulation technique for scanning force microscopy," *Review of Scientific Instruments*, vol. 71, pp. 2765-2771, 2000.
- [104] Z. Parlak and F. L. Degertekin, "Combined quantitative ultrasonic and time-resolved interaction force AFM imaging " *Rev. Sci. Instrum.*, vol. 81, 2010.
- [105] W. D. J. Mehner, B. Schauwecker, and D. Ostergaard, "Reduced order modeling of fluid structural interactions in MEMS based on model projection techniques," in *Transducers*, 2003, pp. 18840-1843.
- [106] N. A. Hall, M. Okandan, R. Littrell, B. Bicen, and F. L. Degertekin, "Simulation of Thin-Film Damping and Thermal Mechanical Noise Spectra for Advanced Micromachined Microphone Structures," *Microelectromechanical Systems, Journal of*, vol. 17, pp. 688-697, 2008.